Title
Synthesis and Characterization of Simultaneous Electronic and Ionic Conducting Block Copolymers for Lithium Battery Electrodes

Author
Patel, Shrayesh

Publication Date
2013

Peer reviewed|Thesis/dissertation

Synthesis and Characterization of Simultaneous Electronic and Ionic Conducting Block Copolymers for Lithium Battery Electrodes

By

Shrayesh Naran Patel

A dissertation submitted in partial satisfaction of the

requirement for the degree of

Doctor of Philosophy

in

Chemical Engineering

in the

Graduate Division

of the

University of California, Berkeley

Committee in Charge:

Professor Nitash P. Balsara, Chair
Professor Rachel A. Segalman
Professor Jeffrey R. Long

Spring 2013

Synthesis and Characterization of Simultaneous Electronic and Ionic Conducting Block Copolymers for Lithium Battery Electrodes

by Shrayesh Naran Patel

Abstract

Synthesis and Characterization of Simultaneous Electronic and Ionic Conducting Block Copolymers for Lithium Battery Electrodes

by

Shrayesh Naran Patel

Doctor of Philosophy in Chemical Engineering

University of California, Berkeley

Professor Nitash P. Balsara, Chair

Materials with nanostructured conducting domains are essential for a wide range of applications related to alternative energy. Active materials in battery and fuel cell electrodes such as LiFePO4, graphite, and platinum, are either electronic or ionic insulators. Nanoscale electron- and ion-conducting domains are necessary for enabling redox reactions in these materials. For example, a traditional porous lithium battery electrode consists of a redox-active material, carbon black for electronic conduction, and non-conductive binder that holds the particles in place. The pores are backfilled filled with organic electrolyte for ionic conduction. In some cases such as $LiFePO_4$, electronic and ionic conductivities are so low that the active materials must be in nanoparticle form, and addressing such particles requires the transport of both kinds of charges to occur on nanometer length scales. Materials such as block copolymers can self-assemble and form co-continuous nanoscale domains. In this study, poly(3-alkylthiophene)-*block*-poly(ethylene oxide) (P3AT-PEO) copolymers are used to conducts both electronic and ionic charges. P3AT-PEO block copolymer molecules self-assemble on the nanometer length scale to yield P3AT-domains that conduct electronic charges and PEO-domains that conduct ionic charges. We propose to create a unique battery electrode where the $LiFePO_4$ active material is dispersed in a nanostructured P3AT-PEO block copolymer, which functions simultaneously as the conductor of lithium ions and electronic charge, as well as the binder material in the electrode.

The first phase of this dissertation work involved the synthesis of P3AT-PEO block copolymers. Regioregular P3ATs were synthesized using the Grignard metathesis (GRIM) polymerization method where in-situ end-group functionalization was employed to obtain ethynyl-functionalized P3ATs. Azide-functionalized PEOs were obtained through end-group modification of PEO monomethyl ether. Ethynyl-functionalized P3ATs and azide-functionalized P3AT-PEO were coupled using 1,3-dipolar cycloaddition “click” reaction to obtain P3AT-PEO block copolymer. In particular, poly(3-hexylthiophene)-*block*-poly(ethylene oxide) (P3HT-*b*-PEO) copolymers and a poly(3-ethylhexylthiophene)-*block*-poly(ethylene oxide) (P3EHT-*b*-PEO) copolymer were synthesized in this study.

Next, the morphology of the P3AT-*b*-PEO copolymer was characterized using small angle X-ray scattering (SAXS). The morphologies of P3HT-b-PEO copolymers, where the

P3HT block is the major component, are dominated by nanofibrils due to the crystallization of P3HT. In contrast, the nearly symmetric P3HT-*b*-PEO copolymers self-assemble into a lamellar phase. In addition, we show that P3EHT-*b*-PEO chains self-assemble to produce traditional nanoscale morphologies such as lamellae and gyroid in the melt-state. The segregation strength between the two blocks is controlled through the addition of lithium bis(trifluromethanesulfonyl) imide (LiTFSI). Our approach enables estimation of the "effective" Flory-Huggins interaction parameter, χ_{eff}, using the random phase approximation (RPA). The χ_{eff} trends with salt concentration suggest that the TFSI anion preferentially segregates into the P3EHT phase while Li^+ remains in the PEO phase. For the salt-free sample, the gyroid morphology, obtained in the melt-state, is transformed into lamellae when the P3EHT block is crystallized. This is due to the "breaking out" of the crystalline phase. At high salt concentrations, P3EHT-*b*-PEO has a lamellar morphology in both melt and crystalline states (confined crystallization).

We present the first reported study on the relationship between morphology and electronic/ionic charge transport of P3HT-*b*-PEO/LiTFSI mixtures. Using ac impedance spectroscopy, we show that P3HT-*b*-PEO/LiTFSI mixtures can conduct electronic and ionic charges simultaneously. At 90 °C, the electronic conductivity of P3HT-*b*-PEO/LiTFSI mixtures ranged from 10^{-8} to 10^{-5} S/cm depending on the volume fraction of P3HT. The decoupled ionic conductivity is around $\sim 10^{-4}$ S/cm. It was shown that LiTFSI partitions between P3HT and PEO microphases. In particular, LiTFSI only partitions between the microphases when the PEO block molecular weight is 2 kg/mol while we observe no partitioning when the PEO block molecular weight of 4.2 kg/mol. It thus appears that the chemical potential of LiTFSI in PEO is a function of the PEO block molecular weight. We propose that the higher chemical potential of LiTFSI for P3HT-*b*-PEO copolymers with PEO molecular weight of 2 kg/mol drives the LiTFSI into the P3HT rich microphase.

The electronic conductivity can be further increased by electrochemically chemically doping the P3HT chains with LiTFSI. Therefore, we quantified the electronic conductivity P3HT-*b*-PEO copolymers electrochemically oxidized with LiTFSI. We use a novel solid-state three-terminal electrochemical cell that enables simultaneous conductivity measurements and control over electrochemical doping of P3HT. At low oxidation levels, the electronic conductivity increases from 10^{-8} S/cm to 10^{-4} S/cm. At high oxidation levels, the electronic conductivity approaches 10^{-2} S/cm. These values match or exceed the ionic conductivity, which is important for enabling redox reactions in a battery as they involve equal moles of lithium ions and electronic charges.

A lithium metal battery was assembled where the positive electrode consisted of P3HT-*b*-PEO conductive binder and $LiFePO_4$ active material. We were able to cycle batteries and obtain capacities approaching the theoretical limit of $LiFePO_4$. Importantly, P3HT is electroactive within the voltage window of a charge/discharge cycle. The electronic conductivity of the P3HT-*b*-PEO copolymer binder is in the 10^{-4} to 10^{-2} S/cm range over most of the potential window of the charge/discharge cycle. This allows for efficient electronic conduction needed for the successful cycling of the batteries. However, at the end of the discharge cycle, the electronic conductivity decreases sharply to 10^{-7} S/cm, which means the "conductive" binder is now electronically insulating. The ability of our conductive binder to switch between electronically conducting and insulating states in the positive electrode provides an unprecedented route for automatic overdischarge protection in batteries.

Table of Contents

List of Figures

List of Tables

Acknowledgements

I first must thank my mom, dad, brother, and sister. Their love and support has been very important as I pursued my Ph.D. degree. My parents have worked hard and have sacrificed a lot to make sure their children have the best opportunities in America. This dissertation is dedicated to them. Without my family, none of this would have been possible.

I must thank my advisor, Prof. Nitash Balsara, whose guidance, patience, support, and enthusiasm was instrumental in obtaining my Ph.D. degree. Nitash had complete confidence in me even though I was struggling mightily with my project in the early years. He recognized my hard work during that time and would remind me that my work ethic would pay off in the end. He was completely right. I will be forever grateful for that.

The next person I must thank is Dr. Anna Javier who is a postdoctoral fellow in the lab. The best thing that Nitash did for me was to hire Anna. The arrival of Anna to the lab was a huge turning point for my project. In a few months, she successfully completed the synthetic goals that I was struggling with. Chapter 2 deals with the synthetic part of my project. Anna should get full credit for establishing that in our lab. She also did some amazing work in fabricating batteries, which is discussed briefly in Chapter 5. It was amazing what she did in a span of one year.

Next, I would like to thank the more "senior" graduate students in lab when I joined in 2007. I would like to thank Nisita Wanakule, Alisyn Nedoma, and Justin Virgili. I bugged them frequently with stupid questions as I tried to learn as much as I could about polymer physics. Nisita was particularly helpful in teaching me PEO synthesis, answering all my questions, and helping me get ready for my qualifying exam. Plus she kept my morale up in lab. I am very thankful for her assistance and friendship. I thank Scott Mullin for answering my all electrochemistry related question. I was amazed how much he knew about batteries in general. He was a great resource. Plus, he was a pretty funny guy to be around as he would just say what is on his mind. Greg Stone was also very helpful. I would just randomly start talking to him about something about my project. We would just talk to through it until it made sense.

I would like to thank David Wong and Keith Beers who both joined the lab with me in 2007. All three of us struggled with our projects, but made it through just fine. I have known David the longest dating back to our days at Georgia Tech. We happen to be in the same research lab at Georgia Tech as well. So, it only made sense that we joined the same research lab at Berkeley. David and I shared the same love (and frustration) for Atlanta-based sports. We had many conversations about his during our time in lab. He was a good friend outside of lab as well. Keith Beers was a good person to talk in lab when I wanted to complain about something. Plus, he knew a lot of stuff in general about polymer physics. The inspiration for parts of Chapter 3 was developed after having a conversation with Keith one evening in lab. He made one simple comment which helped me understand all my scattering data (which turned into a Nano Letters paper). He also got some sweet TEM images for me as shown in Chapter 3.

Next, I must thank Nick Young who had the unfortunate honor of sitting next to me for the past five years. He was great to talk to about all random things related to sports and our love for similar television shows. Considering we are both left-handed, it was no surprise that we got along so well. He also rocked a sweet manly beard (I was quite jealous). Plus, he was an amazing manager for the Isothermal PBRs. He led our team to back-to-back College of Chemistry softball championships. I will be in attendance when Nick goes into the College of Chemistry Softball Hall of Fame. Oh yes, he also is doing some cool work with "with them neutrons." I also thank Alex Teran. I was very impressed with how efficiently he works. Sometimes I wish I was as efficient as he was. The amount of quality work he has done during his time in the lab is amazing. I am certain he will be very successful in his future endeavors. Plus, the man knows how to rock the ear rings and how to gel his hair.

I also had the pleasure of working with Jacob Thelen. I am impressed with how he critically thinks through problems. I am certain he will do some great work as he continues his Ph.D. research. Plus, he is a pro with the yo-yo. I also had the pleasure of working with Kevin Wujcik. I think he has done some amazing work using x-ray spectroscopy. In my mind, Kevin is an amazing bell player. Both Jacob and Kevin have been fun guys to be around. I also thank Katherine Harry. She is a very enthusiastic and confident person. I was completely blown away with how much she accomplished in her first year of research. Plus, she is really eager to learn and ready to tackle any challenging problem. I also had the pleasure of working with Adriana Rojas. It was my job to train her before I left. I hope I did a good job and didn't annoy her too much with my goofy humor. I am very confident that she will do some amazing work as she begins her Ph.D. research. I wish Chae-Young Shin, Mahati Chintapalli, Alex Wang, and Doug Greer good luck as they continue their Ph.D. journey. I had the pleasure working with Victor Ho in the Segalman lab. I bugged him a lot when I wanted to talk about things related to polythiophenes. I thank Naveen Venkatensan who was my undergad researcher this past year. He did a really good job and has a future in research. I had the pleasure of knowing Rodger Yuan who has done some amazing research as an undergad. Rodger has a bright future and I look forward to see what he comes up with next.

I must also thank several postdoctoral fellow researchers. First, I would like to thank Xin Wang who showed me how to make polystyrene usinh anionic polymerization. That was the first polymer I synthesized. I also thank Moon Park who taught me sulfonation during my first year. I was really impressed with her quality of work. She set the bar high for our lab. I thank Ashoutosh Panday who was important during the early days for setting up the electrochemistry lab. I also thank Liang Chen. He was the first "chemist" to join the lab during my time. He was one of the most helpful people in lab. He was particularly helpful with synthesis when I was struggling during my early years. I was amazed with his knowledge of polymer chemistry. Next, I thank Dan Hallinan. He was a pleasure to work with and was very helpful. I had many scientific conversations with him that helped me understand my project better. He was a very enthusiastic researcher. It was clear that he loved his work. I am confident he will be a successful professor at Florida State. I also had the pleasure of knowing Evren Ozcam. He was very generous person offering to give me car rides whenever I needed it. I also thank Sebnem Incengolu. She was really fun to be around in lab. She was one of the nicer people in lab and I will miss her a lot. Plus, she has been

very productive scientifically. I am amazed how productive she has been working on so many different projects. I had the pleasure of knowing Guillaume Sudre who did his best to tolerate our stupid American humor. I also thank Inna Gurevich, who has done some great with block copolymer nanocomposites. I had the pleasure of knowing Chelsea Chen who has a good work ethic and a true enthusiasm for electron microscopy. I also thank Nikos Petzetakis who, as Nitash puts it, is a "maestro" of anionic polymerization. For the brief time they have been in lab, I had the pleasure of knowing Pepa Cotanda, Irune Villaluenga, and Didier Devaux. I wish them good luck as they begin their postdoctoral fellowship.

Lastly, I thank Prof. Rachel Segalman who has been very helpful and supportive during my Ph.D. research. I also thank Prof. Malika Jeffries-EL (and her graduate student, Robyn Laskowski) for allowing me to work in her lab at Iowa State University so I can learn P3HT synthesis. I thank Dr. Venkat Srinivasan for helpful discussions related to the electrochemistry of my project.

Chapter 1 - Introduction

1.1 Electronically Conducting Polymers

Electronically conducting polymers (Figure 1.1) are conjugated materials where the π-bonding characteristic in the polymer backbone leads to electron delocalization; thus allowing for pathways for charge transport. Conjugated polymers are considered to be insulators or semiconductors in their pristine where electronic conductivities are typically less than 10^{-8} S/cm. The game changing moment for electronically conducting polymers occurred when Chiang at el. showed that exposing polyacetylene (PA) to a halogen vapor, I_2, increased the electronic conductivity to over 100 S/cm.[1] Iodine "dopes" PA through oxidization where electrons are removed from the p_z orbitals of the polymer backbone (p-doping). The electrons in the partially empty conjugated p-orbitals are highly mobile; thus increasing the conductivity. Alternatively, PA can be doped through reduction where electrons are added to the p_z orbital (n-doping). In general, most conjugated polymers are stable p-type conductors and poor n-type conductors.[2]

The discovery of electronically conducting polymers opened up a new field of research. One can now have a material that has the electrical and optical properties of semiconductors or metals, while taking advantage of the processability of polymers. The applications of electronically conducting polymers have included transistors, photovoltaics, smart windows, chemical sensors, batteries, supercapacitors, etc...[3-10] The impact of electronically conducting polymers was recognized in 2000 when Heeger, MacDiarmid, and Shirakawa were awarded the Nobel Prize in Chemistry for the discovery of conductive polymers.[11-13]

This dissertation focuses on polythiophenes-based polymers, which is described in more detail in the next section.

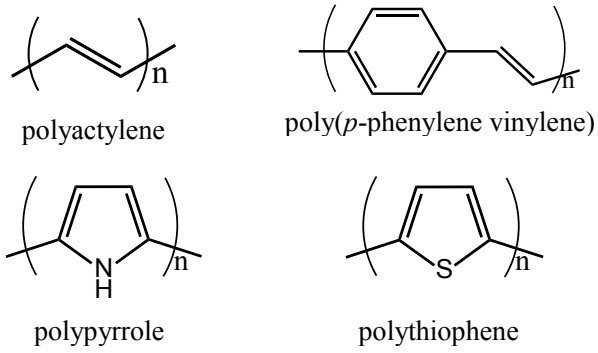

Figure 1.1. Few examples of electronically conducting polymers

1.2 Structural and Charge Transport Properties of Poly(3-alkylthiophene)s

Unsubstituted polythiophenes have high electronic conductivity in addition to the added benefits of better thermal and environmental stability relative to traditional conjugated polymers like polyacetylene.[14, 15] However, unsubstituted polythiophenes are highly insoluble and have poor processability.[14, 15] To address this issue, alkyl side chains are added to the polymer backbone, which increases the solubility of the polymer in organic solvents.[16] In particular, substituted polythiophenes have alkyl side chains (butyl, hexyl, octyl, etc ...) on the 3 position of the thiophene monomer [poly(3-alkylthiophene)s, P3ATs)].[14, 17] As a result, P3ATs have improved solution and melt processability.

Due to the asymmetrical nature of the 3-alkylthiophene monomer, it is important to consider the regiochemistry during the synthesis of P3ATs.[17] The 3-alkylthiophene monomer can be coupled between the 2 and 5 positions resulting in three distinct couplings: head-to-head (HH), tail-to-tail (TT), and head-to-tail (HT). During further polymerization, these regiochemical couplings lead to four distinct triad regioisomers: HH-HH, TT-HH, HT-HH, and TT-HT (Figure 1.2), where the HT-HT coupling is the regioregular isomer. Regioirregular structures have twists in the polymer backbone due to steric hindrance of the alkyl side chains, which results in the reduction of the conjugation length and poor π-π stacking of the polymer backbone. This leads to increase in the bandgap and, as a consequence, a lower conductivity. For example, Mao et al. showed that the electronic conductivity of P3HT doped with nitrosonium tetrafluroborate ($NOBF_4$) increases from 9 x 10^{-3} S/cm to 6 S/cm when the regioregularity goes from 52% to 80%.[18] On the other hand, P3ATs with a highly regioregular structure (>90%) have limited twists in the its backbone which allows for a planar conformation. This leads to an increase in conjugation length and better π-π stacking, thus higher electronic conductivity. Doped P3HTs with high regioregularity (~98%) have been reported to have electronic conductivity greater than 100 S/cm.[17, 19]

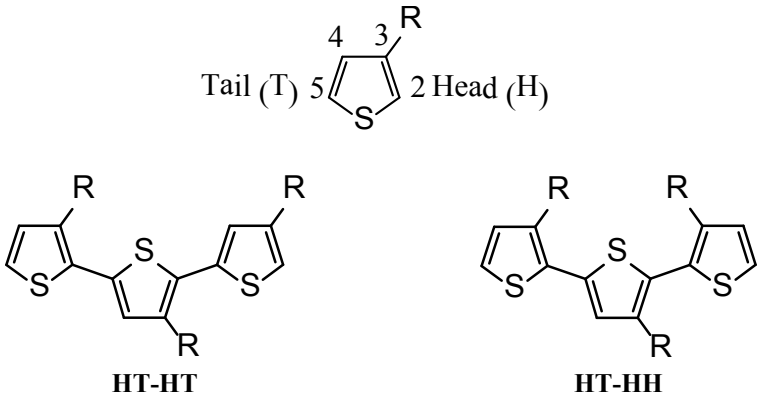

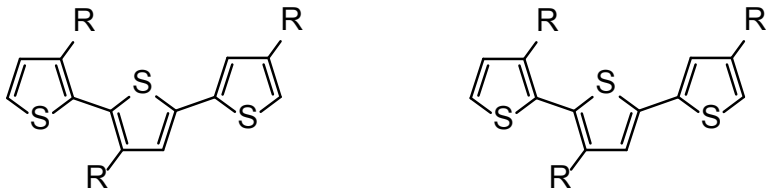

HH-TT **TT-HT**

Figure 1.2. Regioisomers found in poly(3-alkylthiophene)s (P3ATs).

The methods used to synthesize P3ATs dictate the extent of regioregularity. Original synthetic routes for P3AT synthesis resulted in regioirregular structures.[20, 21] However, new methods of P3AT synthesis was introduced by both McCullough[22] and Rieke[23] in the early 1990s. The McCullough method uses selectively brominated 3-alkylthiophene followed by lithiation and transmetalation at -40 °C. The intermediate is polymerized via Kumada cross-coupling using Ni(dppp)Cl_2 catalyst. The resulting P3ATs have a regioregularity greater than 98%. The Rieke method uses a highly reactive "Rieke zinc" (Zn*) with a 2,5-dibromo-3-alkylthiophene monomer to form two intermediate isomers. In particular, the formation of the 2-(bromozincio)-3-alkyl-5-bromothiophene isomer at -78 °C results in a higher regioregular polymer. Also important is the type of catalyst used for polymerization where the addition Ni(dppe)Cl_2 results in a regioregular polymer while the addition of Pd(PPh_3)$_4$ leads to a regiorandom polymer. Even though above two methods results in regioregular P3ATs, the downside is that reaction steps involve low temperatures (an issue for large scale production). However, in the late 1990s, the McCullough group developed a room temperature synthetic route for regioregular P3ATs synthesis called the Grignard Metathesis (GRIM) method.[24] Using 2,5-dibromo-3-alkythiophene monomer with a Grignard reagent and Ni(dppp)Cl_2 catalyst, P3ATs are synthesized at room temperature with regioregularity greater than 95%. In addition, the GRIM method generates a "living" polymer thus allowing for *in-situ* end-group functionalization through termination with a desired Grignard reagent (*e.g.* vinylmagnesium bromide, allylmagnesium bromide, etc...).[25] This reduces or eliminates the need for post-polymerization functionalization reactions in order to synthesize P3AT-containing block copolymers. It is important to note that the proposed mechanism of the GRIM method begins with formation of HH (head-to-head) dimer and after which further polymerization follows the HT (head-to-tail) coupling route.[26] Therefore, every P3AT chain will contain at least one HH dimer.

The planarity of the polymer backbone is enabled by head-to-tail coupling of the 3-alkylthiophene monomer and promotes interchain π-π interactions. As a result, the P3AT chains self-assemble to form a polycrystalline structure referred to as the nanofibrillar morphology.[27-29] This has been seen in both electron microscopy and atomic force microscopy, is believed to be a signature of these interactions.[28, 29] A representative AFM image of regioregular P3HT with the nanofibrillar morphology is shown in Figure 1.3. The dimensions of the P3HT microstructure were determined using grazing incidence wide-angle X-ray scattering (GIWAXS) experiments. The distance between hexyl side chains is 1.6 nm while the π-π stacking distance is 0.38 nm between to polymer chains. The width of a nanofibril is a function of molecular weight where the width can range from 20-50 nm. Surrounding the nanofibrils are amorphous P3HT chains. It is important to note that the

processing steps used to create the samples affect the observed morphology. Solution cast samples made under rapid evaporation conditions results in highly disordered structure, while those made under slow evaporation conditions display the nanofibrillar morphology with higher percent crystallinity.[30]

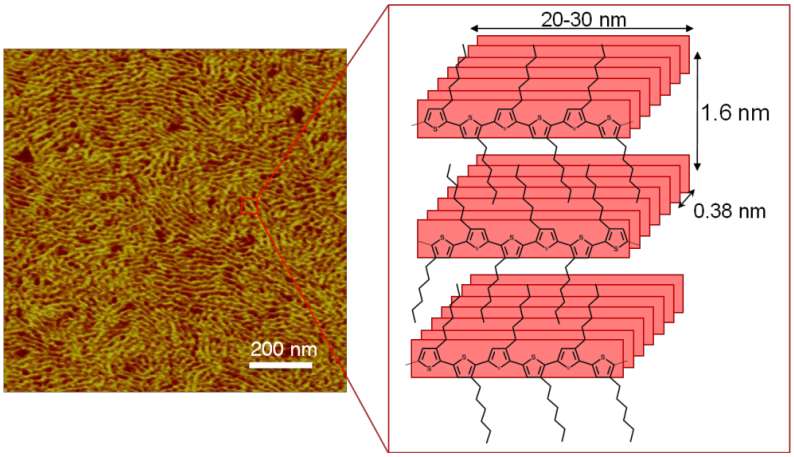

Figure 1.3. Atomic Force Microscopy (AFM) image showing the nanofibrillar morphology of P3HT. The brighter wire-like structures are the nanofibrils. A schematic of the P3HT crystal structure are shown in the red box.

The charge transport properties of P3ATs are typically characterized in terms of conductivity or mobility, which are related to each other by the following equation:

$$\sigma_e = ne\mu, \tag{1.1}$$

where σ_e corresponds to electronic conductivity, n is the charge carrier density, e is the elementary charge, and μ is the mobility. It is clear electronic conductivity is affected by both charge carrier density and mobility. Meaning, one may either increase charge carrier density or mobility to enhance conductivity. Mobility is a measurement of how fast charge carriers move in the presence of an electrical field. P3ATs are stable hole conductors so charge transport is discussed in the context of hole mobility.

Pristine P3ATs have intrinsically a very low charge carrier density, which results in a very low electronic conductivity. The presence of impurities in "pristine" P3ATs can affect the electronic conductivity. Reported conductivity values of undoped regioregular P3HT range from 10^{-5} to 10^{-8} S/cm.[31-36] In addition to impurities, the configuration of the conductivity measurement can affect the electronic conductivity. Lui *et al.* found that in-plane conductivity of regioregular P3HT was 10^{-5} S/cm while that in the through-plane geometry was 10^{-8} S/cm.[34] Furthermore, differences in sample preparation must also be accounted for when comparisons between reported literature values are made. For instance, the extent of crystallinity in the P3AT conductivity sample can affect the conductivity value. Therefore, care must be taken that all samples have a high level of purity and are processed in a consistent manner.

As mentioned earlier, conjugated polymers need to doped to increase conductivity. The term "doping" was taken from the field of solid-state physics where inorganic semiconductors (silicon) are doped to increase conductivity. The doping mechanism for inorganic semiconductors involves the substitution of atoms. The concentration of the

dopant is typically in the ppm level.[37] On the other hand, "doping" conjugated polymers has a completely different meaning. The dopant molecule undergoes a redox reaction with the polymer to generate charge carriers.[11] In addition, the optimal dopant concentration is significantly higher in conjugated polymers (20-30 mole percent).

P3ATs can be doped chemically or electrochemically. In the case of chemical doping, introduction of an oxidizing agent such I_2 or F_4TCNQ results in a spontaneous oxidation of the conjugated polymer.[18, 38-40] In the case of electrochemical doping, an applied potential drives the electrochemical oxidation of the conjugated polymer.[41-43] The dopant counterion diffuses in from the electrolyte to stabilize the oxidized polymer. With both methods, one can precisely control the doping level and conductivity. Furthermore, doping alters the electronic structure of P3ATs.[44, 45] The p_z orbitals overlap to form the valence and conduction bands where the difference between these bands is the band gap (E_g). For regioregular P3HT, E_g is around 1.7 eV, which small enough to classify P3ATs as semiconducting polymers. During the oxidation of P3AT, an electron is removed from the valence band. This results in the formation of a polaron (hole/radical pair) where two electronic states are formed between the valence and conduction bands. Additional removal of electrons, results in the formation of a bipolaron (hole/hole pair). At high oxidation levels, the electronic states combine to form bipolaron bands in between the valence and conduction bands. These changes in the band structure can be observed with UV-VIS and near-IR measurements. The optimal separation between a bipolaron is dictated by two competing forces. Coulombic repulsion between the bipolaron increases the distance between the two holes. However, this increases the quinoid structure of the polymer backbone, which is a high energy state. As a result, these two competing forces are balanced where the bipolaron is stabilized over six thiophene units.

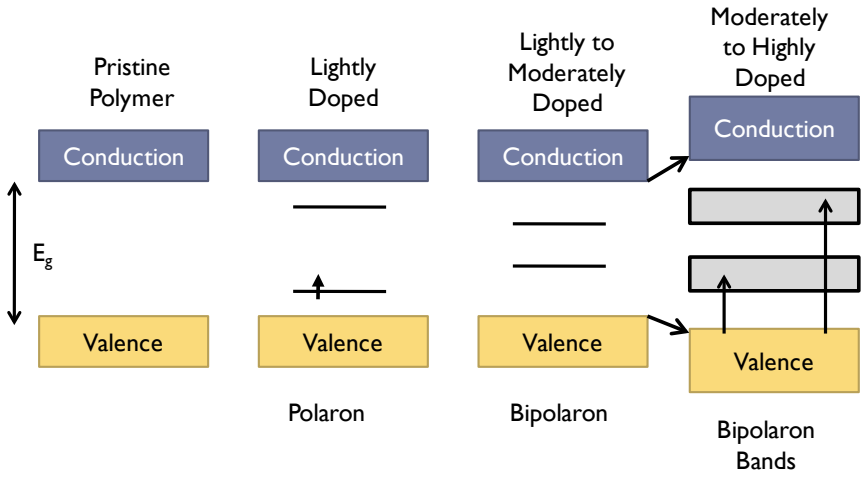

Figure 1.4. Evolution of band structure upon doping. At low doping levels results in the formation of a polaron. Further doping results in a bipolaron, which eventually turn into bipolaron bands at high oxidation levels (>30%).[44]

Since the introduction of organic transistors, mobility has been the preferred term to characterize the charge transport properties of semiconducting polymers like P3ATs. Most reported mobility values for P3ATs are from organic thin-film transistors (TFTs), where charge carriers are generated through a field-effect mechanism. Meaning, it does not

undergo chemical doping to generate charge carriers and no counterions are present in the semiconducting polymer during the transistor operations. As a result, TFTs do not suffer from Coulomb traps as seen with doping, which mean the measured mobility does not change much with charge carrier density. It is important to note that charge transport in TFTs occur within a few nanometer region at the semiconducting polymer and dielectric interface.[46] As a result, the measured mobility using TFTs are typically higher by orders of magnitude relative other techniques.[47] This is in part due to the morphology of the semiconducting polymer at the polymer/dielectric interface. For example, the polymer backbone of P3ATs is perpendicular to the dielectric interface.[48] This is the ideal configuration because the charge transport between the source and drain occur parallel to the interface. If the polymer backbone aligns parallel to the dielectric interface, the measured hole mobility of polymer would be several orders magnitude lower.[48] In addition, the processing conditions used to fabricate a TFT (i.e. solution casting method, substrate modification, type of dielectric, etc...) can affect the measured mobility.[49, 50] Even though TFTs only provide the charge carrier mobility within a few region of the polymer, alternative methods such as time-of-flight (TOF) measurements can provide bulk values of mobility.[51] Therefore, it is important to remember that there is not one universal mobility value for a particular type of semiconducting polymer.

1.3 Ion Conducting Polymers - Polymer Electrolytes

A traditional electrolyte consist of ionizable species such as KOH and $LiPF_6$, dissolved in a high dielectric medium such as water or organic solvents (e.g. ethylene carbonate). Fenton et al. discovered in 1973 that alkali metals could be dissolved in poly(ethylene oxide) (PEO) (Figure 1.5).[52] This was a game changing moment as it open up the field of dry polymer electrolytes. Polymer electrolytes like PEO are an important class of electrolytes because they are intrinsically safer than the traditional volatile electrolytes (e.g. $LiPF_6$ in ethylene carbonate). In addition, lithium metal batteries are desirable because they have significantly higher energy density than traditional lithium-ion battery batteries. Organic liquid electrolytes cannot be used in lithium metal batteries due to irreversible side reactions between the electrolyte and lithium metal and the formation of lithium dendrites. The ionic conductivity of salt-containing PEO electrolytes is in the 10^{-3} S/cm range, which is lower than traditional electrolytes.[53-55] Nevertheless, this does not preclude one from using polymer electrolytes for various applications; especially for low current applications.

PEO is a polyether where the electronegative oxygen atoms can readily coordinate with various lithium ions. Typically, six ether oxygen atoms surround a lithium ion, which is the lowest free-energy configuration of lithium ions in a PEO matrix.[56, 57] It is important to note that PEO is a semicrystalline polymer where the crystalline domains impede lithium ion transport. As a consequence, PEO is heated above its melting point (60 °C) for optimal ionic conductivity. Segmental motion of the PEO chains results in the diffusion of the lithium ion to another low free-energy coordination site (the interaction between the ion and polymer is affected by the glass transition temperature, T_g). Another route of ion motion occurs through diffusion of the entire polymer chain coordinated with the lithium ions. However, as the molecular weight of PEO increases (above 2 kg/mol) the chains become more entangled thus inhibiting the diffusion of polymer chains.[58] As a result, the segmental motion of PEO is the mode of lithium ion charge transport. When the PEO molecular increases from 200 g/mol to

2,000 g/mol, the ionic conductivity of PEO with LiTFSI [lithium bis-(trifluoromethanesulfonyl) imide] decreases by a factor of 4.5 (4.5 x 10^{-3} S/cm to about 1 x 10^{-3} S/cm).[55] The ionic conductivity remains around 1 x 10^{-3} S/cm very higher molecular weight PEO (1x10^{6} g/mol). The $TFSI^-$ anion is a popular counterion because it can easily dissociate from the lithium ion due the resonance stabilization of the negative charge. Plus, it can suppress the crystallinity of PEO. It is important to note that that ionic conductivity measured in PEO/LiTFSI mixture is the ionic conduction of both the lithium ion and TFSI anion where the anion contributes to 80% of the conductivity.[58]

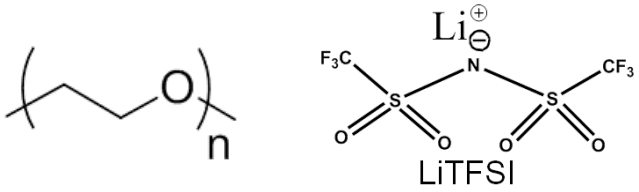

Figure 1.5. State of the art polymer electrolyte - poly(ethylene oxide) with LiTFSI.

1.4 Block Copolymer Self-Assembly

Block copolymers consists of two or more homopolymers that are linked through covalent bonds. For example, as used in this dissertation study, one can synthesize a diblock copolymer where one block conducts electronic charge while the other block conduct ionic charges (P3AT-*block*-PEO). Block copolymer chains can self-assemble on the nanometer length scale (microphase separation) to form periodic structures such as lamellae, hexagonally packed cylinders, and gyroid.[59, 60] Block copolymer self-assembly is dictated by balancing the enthalpic forces favoring the polymer chains to phase separate and the entropic forces favoring mixing between the polymer chains. The enthalpic forces between the chains are quantified through the Flory-Huggins interaction parameter, χ, which is inversely proportional to temperature, T. In addition to χ, the phase behavior of block copolymers is dictated by the degree of polymerization (N) and volume fraction of one of the blocks (ϕ).[61] A classical universal block copolymer phase diagram is shown in Figure 1.6. The ordinate of the phase diagram is the product, χN, which is related to the enthalpic and entropic contributions of the block copolymer chains. At ϕ = 0.5, the block copolymer will microphase separate (ordered) at $\chi N > 10.5$ and the block copolymer chains will mix (disordered) at $\chi N < 10.5$. With a block copolymer system with a particular value of χ, one may obtain various morphologies by varying N,ϕ, and T. It is important to note the phase diagram shown in Figure 1.6, is specifically for a system where the blocks have equal persistence lengths and low polydispersity.[62, 63] In addition, the critical χ value of 10.5 increases when compositional fluctuations are included in the thermodynamics of the block copolymer self-assembly.[64] This is particularly important when N is small.

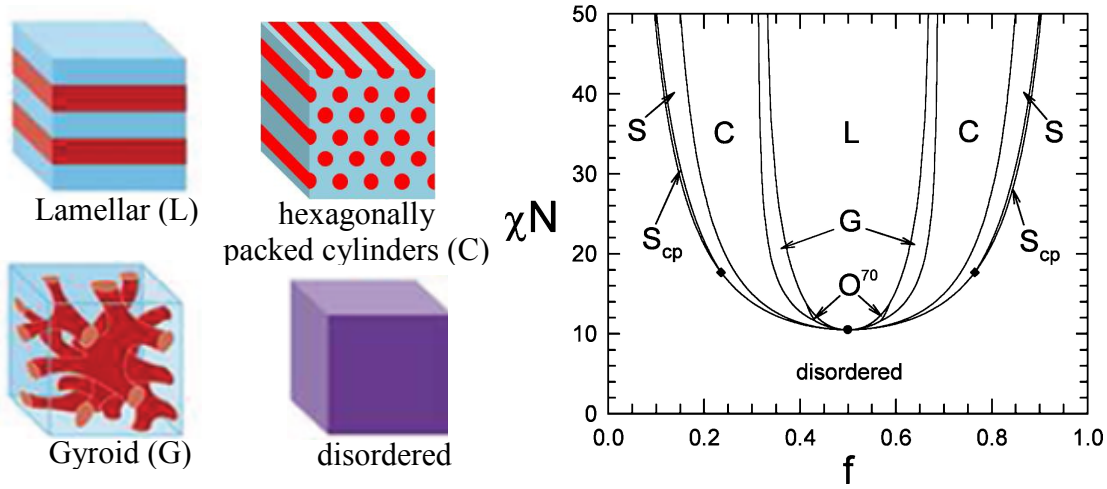

Figure 1.6. **(a)** Schematic of different diblock copolymer morphologies. (b) Theoretical diblock copolymer phase diagram taken from ref. 60. S_{cp} is closed-packed spheres, S is bcc spheres, C is hexagonally packed cyclinders, G is gyroid, O^{70} is *Fddd*, L is lamellar.

The above phase diagram is explicitly derived for coil-coil (flexible-flexible) block copolymers. It is well known that conjugated polymers have a more rigid backbone (i.e. rod-like), thus behaving less like a coil-like polymer. As a result, the liquid crystalline interactions between the conjugated (rod) block (Maier-Saupé parameter, μ) and the block length ratio (ν) need to be considered to fully describe the phase behavior.[65-69] The interplay between the liquid crystalline interactions and the interactions dictating microphase separation results in various morphologies, such as zig-zag and arrowhead, not observed in the traditional block copolymers.[67] However, these unique morphologies are kinetically trapped structures. As a result, Olsen et al. studied a weakly segregated (low χN) rod-coil block copolymer system (DEH-PPV-*b*-PEO) that formed thermodynamically stable morphologies.[70] In Figure 1.7, a universal phase diagram for a weakly segregated rod-coil block copolymer system in terms of χN and μN, which is related to liquid crystalline interactions contribution to phase behavior.[70] Lamellar, nematic, and isotropic phases are observed in rod-coil system.

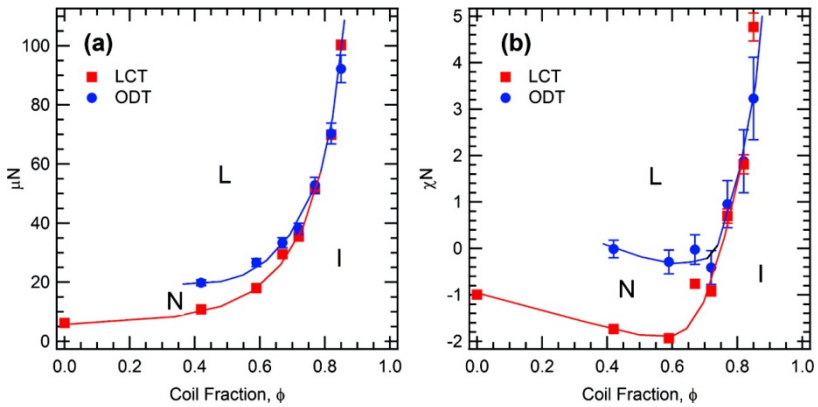

Figure 1.7. Experimental universal phase diagram for a weakly segregated rod-coil block copolymer taken from ref. 70. L is lamellar, N is nematic, and I is isotropic.

Persistence length measurements indicate that P3ATs are, in fact, semiflexible polymers.[71] Therefore, it is more appropriate to consider the phase behavior of semiflexible-flexible block copolymers (assuming the second block is a coil-like polymer such as PEO). The phase behavior of a semiflexible-flexible block copolymer is governed by χ, μ, N, and ϕ.[68] In Figure 1.8, a theoretically predicted phase diagram is shown for a semiflexible-flexible block copolymer with μ/χ of 3.2 and 11.4.[68] It is clear the extent of liquid crystalline interactions affect the phase behavior. Higher ratio of μ/χ results in a large window for the nematic phase (S = smectic, or, in other words, lamellar phase and I = isotropic which refers to a disordered phase). In addition, at higher μ/χ, the critical χN is lower than the coil-coil value of 10.5 at $\phi = 0.5$.

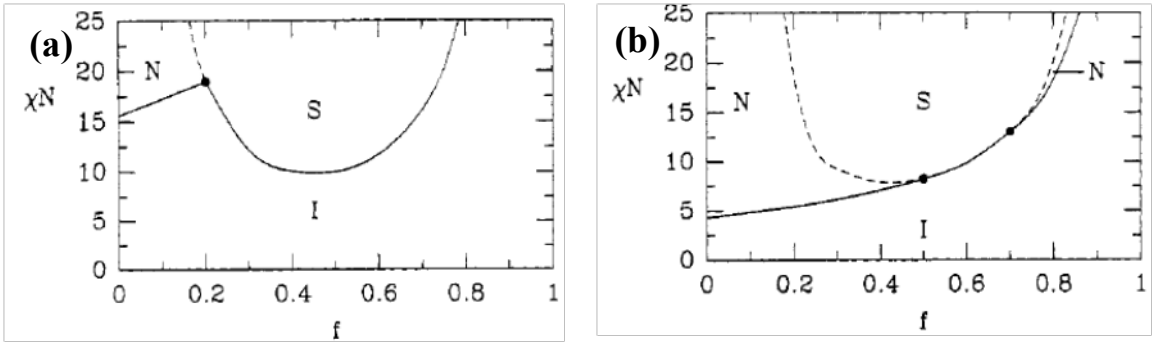

Figure 1.8. Theoretical phase diagram for a semiflexible-flexible block copolymer for **(a)** $\mu/\chi = 3.2$ and **(b)** (b) $\mu/\chi = 11.4$ were taken from ref.68. S is smectic (lamellar), N is nematic, and I is isotropic (disordered).

The above phase diagrams in Figures 1.6-1.8 are specifically for polymers in the melt-state. Block copolymer self-assembly can be affected if one of the blocks is crystallizable (as is the case with both P3ATs and PEO). The morphology of a semicrystalline block copolymer in the solid-state is dictated by the chemical incompatibility of the two blocks (χ, the Flory-Huggins interaction parameter) and whether the non-crystallizing block is either glassy or non-glassy.[72-80] When the non-crystallizing block is glassy, the morphology of the melt-state is retained and the crystallization occurs within the nanoscale domains (confined crystallization). When the non-crystallizing block is non-glassy, the segregation strength of the block copolymer is a major factor on the morphology in the solid-state. For weakly segregated systems (low χN), the melt-state morphology is destroyed upon crystallization (breakout crystallization). When the segregation strength is sufficiently high (large values of χN), the melt-state morphology is retained.

1.5 Lithium Battery Design

A lithium-ion battery consists of a negative electrode, a positive electrode, and an electrolyte. In a traditional lithium-ion battery, the electrolyte is a lithium salt in organic solvent, the negative electrode is graphite, and the positive electrode consists of a redox-active intercalation material ($LiCoO_2$ or $LiFePO_4$). In addition, the positive electrode contains carbon black for electronic conduction and non-conductive binder that holds the particles in place (Figure 1.9). The pores are backfilled filled with organic electrolyte for ionic conduction. Separating the two electrodes is a porous membrane separator filled with electrolyte, which serves to transport lithium ions between the electrodes. A schematic of a a traditional lithium-ion battery is shown in Figure 1.9. When discharging a battery, the positive electrode is the cathode while the negative electrode is the anode. On the other hand, when charging a battery, the positive electrode is the anode and the negative electrode is the cathode. Recently, the battery community has accepted the convention of always referring to the positive electrode as the cathode and the negative electrode as the anode. To avoid confusion in this dissertation, we will refer to the electrodes as being either a positive or negative electrode.

Positive Electrode

$$LiFePO_4 \underset{\text{discharge}}{\overset{\text{charge}}{\rightleftharpoons}} FePO_4 + e^- + Li^+$$

Negative Electrode

$$Li^+ + e^- \underset{\text{discharge}}{\overset{\text{charge}}{\rightleftharpoons}} Li$$

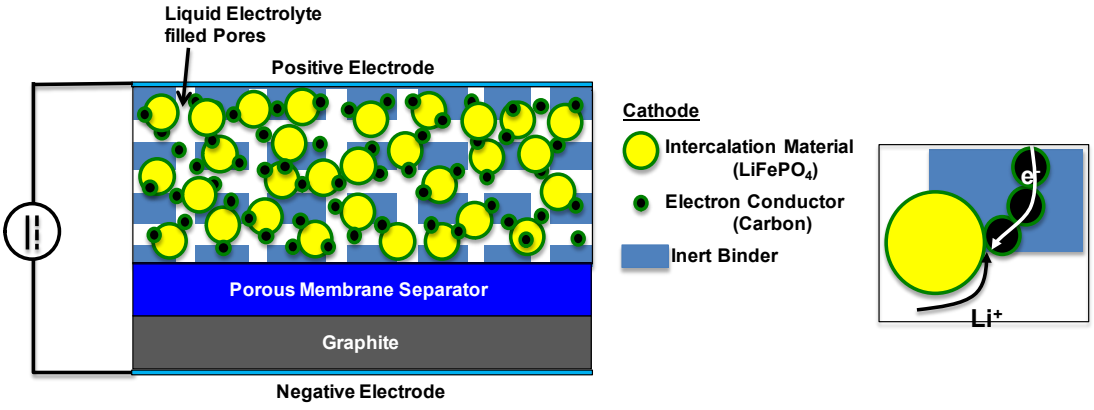

Figure 1.9. Traditional Lithium-ion Battery Design. The positive electrode consists of a redox-active intercalation material ($LiFePO_4$), inert binder, and liquid electrolyte. The negative electrode is a graphite electrode. Separating the two electrodes is a porous membrane separator filled with electrolyte, which serves to transport lithium ions between the electrodes.

For active materials like $LiFePO_4$, the electronic and ionic conductivities are so low that the active materials must be in nanoparticle form, and addressing such particles requires the transport of both kinds of charges to occur on the nanometer length scales.[81-84] As discussed in section 1.4, block copolymers can self-assemble and form co-continuous nanoscale domains. In this study, P3HT-PEO block copolymers are used to conducts both electronic and ionic charges. P3HT-PEO block copolymer molecules self-assemble on the nanometer length scale to yield P3HT-domains that conduct electronic charges and PEO-domains that conduct ionic charges. In our system, the $LiFePO_4$ active material is dispersed in a nanostructured P3HT-PEO block copolymer that functions simultaneously as the conductor of lithium ions and electronic charge, as well as the binder material in the electrode. The fact that we are using a polymeric material in the battery allows us to use lithium metal as the negative electrode ($Li \leftrightarrow Li^+ + e^-$). This is advantageous as lithium metal has a higher specific capacity relative to the graphite electrode (3860 mAh/g versus 350 mAh/g). In particular, we use a nanostructured block copolymer electrolyte, polystyrene-*block*-poly(ethylene oxide) (PS-PEO), with an ion-conducting block (PEO) and ion-insulating block (PS) for mechanical integrity. This allows for a route to suppress dendrite growth seen in lithium metal batteries, which is a critical issue for practical applications. However, the motivation behind lithium dendrite growth is beyond the scope of this dissertation. The use of PS-PEO block copolymers to address the issue of lithium dendrite growth is reported in literature.[58, 85-88] A schematic of our proposed lithium battery using the P3HT-PEO block copolymer conductive binder is shown in Figure 1.10.

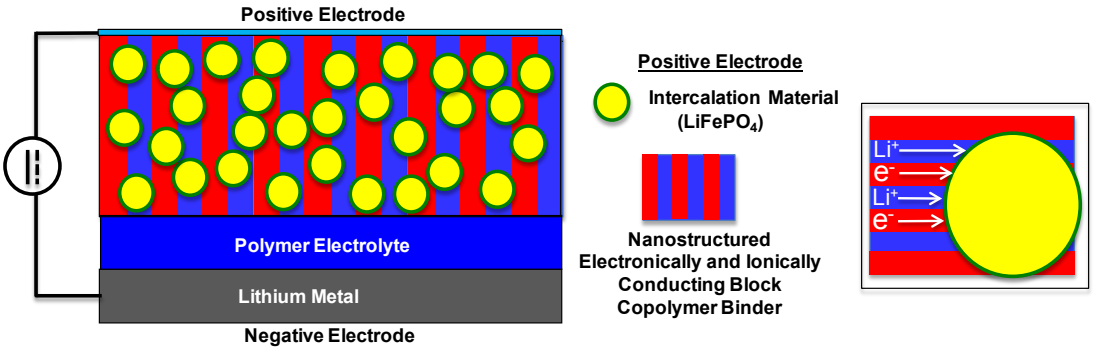

Figure 1.10. Proposed new solid-state lithium battery design. The positive electrode consists of a redox-active intercalation material ($LiFePO_4$) and a P3HT-PEO block copolymer conductive binder. The negative electrode is lithium metal. Separating the two electrodes is a polymer electrolyte, which serves to transport lithium ions between the electrodes.

1.6 Outline of Dissertation

In Chapter 2, we describe the synthesis of 3-alklythiophene monomer, P3AT homopolymer, and P3AT-*b*-PEO copolymers. A description of polymer characterization techniques is presented with a summary of characteristics for the polymers studied in this dissertation. In Chapter 3, the morphology for P3HT-*b*-PEO and P3EHT-*b*-PEO copolymers is characterized using small angle X-ray scattering (SAXS) and transmission electron microscopy (TEM). In addition, we analyze the SAXS data for P3EHT-*b*-PEO salt-containing samples using the random phase approximation to determine effective Flory-Huggins interaction parameter (χ_{eff}). In Chapter 4, we report on the relationship between morphology and simultaneous electronic and ionic charge transport in mixtures of P3HT-*b*-PEO copolymers and LiTFSI. In Chapter 5, we report on the electronic charge transport properties of P3HT-*b*-PEO copolymers electrochemically doped with LiTFSI using a novel three-terminal cell that enables simultaneous conductivity measurements and control over electrochemical doping. In addition, battery cycling data is presented for a lithium metal battery containing a P3HT-*b*-PEO copolymer and $LiFePO_4$ positive electrode (Figure 1.10). The results of our experiments in Chapter 5 provide further insight on the charge transport properties of P3HT-*b*-PEO copolymers when used to conduct electronic and ionic charges in a lithium battery electrode. Lastly, Chapter 6 provides a summary of the dissertation.

Chapter 2 –Poly(3-alkylthiophene-*block*-ethylene oxide) Synthesis and Characterization

ABSTRACT

Regioregular P3ATs were synthesized using the GRIM polymerization method. In-situ end-group functionalization was employed to obtain ethynyl-terminated P3ATs. Azide-terminated PEOs were obtained through end-group modification of commercially purchased PEO methy ether. P3AT-PEO block copolymers were synthesized using a 1,3-dipolar cycloaddition "click" reaction. The synthesized polymers were characterized through gel permeation chromatography, ^{1}H-NMR, MALDI-TOF MS, DSC, and UV-VIS spectroscopy.

2.1 Materials

All chemical reagents were purchased from commercial sources and used without purification unless otherwise noted. All anhydrous solvents were dispensed from an MBraun solvent purification system.

2.2 Monomer Synthesis

2.2.1 3-hexylthiophene

Table 2.1. Reagents for 3-hexylthiophene synthesis

Compound	Mol. Weight (g/mol)	Mass/Vol.	Moles	Equivalents
3-bromothiophene	163.04	30 g	0.184	---
hexylmagnesium bromide, 2.0M in diethyl ether	---	96.6 mL	0.193	1.05 eq.
Catalyst: Ni(dppp)Cl_2	542.04	300 mg	5.5×10^{-4}	---
Solvent: diethyl ether	---	300 mL	---	---
Product: 3-hexylthiophene	168.3	30.97 g	0.184	---

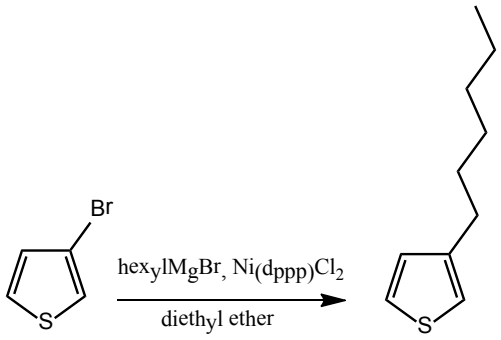

Figure 2.1. 3-hexylthiophene monomer synthesis scheme.

Synthesis

All required glassware are dried overnight in an oven set to >100 °C prior to use and then removed from the oven to be cooled to room temperature. 3-bromothiophene is added directly into a three-neck flask, which is then secured in the fume hood with a clamp. A condenser is attached to the middle neck of the flask and secured with a Keck clip. An additional funnel is then attached to one of the other necks, and also secured with a Keck clip. The gas inlet is added to the condenser and connected to the inert gas source from the Schlenk line. The remaining neck on the flask may be capped with a septum or a glass stopper. Argon gas is then flushed through the system. Anhydrous diethyl ether is added via syringe, and the flask is the lowered. The catalyst, $Ni(dppp)Cl_2$, is then added into the reactor through the 3rd neck, and Ar is flushed for an additional 15 min. The Grignard reagent is then transferred into the addition funnel using a cannula. Grignard reagents are pyrophoric, so care must be taken when transferring. The Grignard reagent is then slowly added into the reaction flask dropwise. This will take some time (>1 h). **Warning:** This is an exothermic reaction, and as such must be performed slowly and carefully. Salts may occasionally precipitate at the tip of the addition funnel preventing solution flow. If this happens, the addition funnel valve may be opened more to make sure the solution continuously drops into the flask. The reaction solution should begin to turn into a brown color as it reacts. When all the Grignard has been added, replace the ice bath with an oil bath, making sure to dry the flask before lowering into oil. Heat the oil bath to ~ 35°C, and leave to reflux gently overnight.

The following day, turn off the heat and remove the reaction flask from the oil bath. Let it cool to room temperature (about 15-20 min). Using a heavy-walled, 2-L beaker, prepare an ice-acid mixture (use 5-10 mL of concentrated hydrochloric acid in 100 mL of ice). Concentrated HCl is highly corrosive and has a strong odor. It must not be used outside a fume hood. Pour the flask contents into the beaker slowly. This is a highly exothermic reaction. Even with the ice, this may heat up quickly if the reaction mixture is added too fast, which may cause the solvent to bubble over. Occasionally mix the ice/acid/solution with a large spatula. The aqueous layer will initially look milky because of the white magnesium salts, while the organic layer has a dark brown color. Let it sit until all of the ice has melted. Add 100 mL of ethyl acetate to the contents of the beaker. Pour the mixture into 1000 mL separatory funnel. Carefully swirl the contents of the sep. funnel inside the fume hood.

Release the pressure by venting. Glassware may pressurize, so frequent venting is necessary. Make sure you secure the cap of the funnel so that it does not pop open. Vent inside the fume hood and make sure the tip is not pointing at anyone. Separate the two layers. Wash the aqueous layer three times with ethyl acetate, or until the organic extract is almost colorless. Use a minimum of ethyl acetate during each extraction. Combine all organic layers and dry using anhydrous magnesium sulfate. Let this stir for at least an hour. Dispose of the aqueous waste in the appropriate waste container. Afterwards, filter off the magnesium sulfate and collect the organic extract into a round bottom flask. Concentrate this using a rotary evaporator.

Purification

Pour previously concentrated solution into a small round bottom flask. Make sure the flask is less than halfway full. Attach a short pathway distillation head, with the necessary attachments (water hose, thermometer). Begin distillation by slowly pulling vacuum without heat. When all residual solvent has been removed, lower the flask into the oil bath and apply heat slowly. The distilled, purified product should be clear and very pale yellow, almost colorless.

2.2.2 2,5-dibromo-3-hexylthiophene

Table 2.2. Reagents for 2,5-dibromo-3-hexylthiophene synthesis

Compound	Mol. Weight (g/mol)	Mass/Vol.	Moles	Equivalents
3-hexylththiophene	168.04	24.80 g	0.1474	---
NBS	177.985	53.77 g	0.3021	2.05 eq.
Solvent: THF	---	250-300 mL		---
Product: 2,5-dibromo-3-hexylthiophene	326.089	48.05 g	0.1474	---

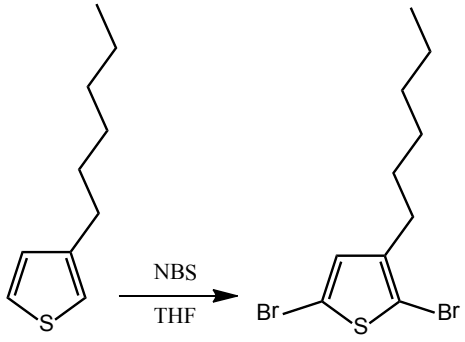

Figure 2.2. 2,5-dibromo-3-hexylthiophene monomer synthesis scheme.

Synthesis

Dissolve the 3-hexylthiophene in about 300 mL of anhydrous THF. Immerse the flask in an ice bath. Measure out 53.77 g of NBS in a weighing dish. Add the NBS (via funnel) portion-wise while stirring (5-6 portions). **Warning:** This is an exothermic reaction which may release some irritant fumes. Do not add all the NBS in one shot. Make sure you are not working too close to the flask. The mixture turns into a light yellow color, with some solid remaining undissolved in the bottom of the flask. Leave the mixture to stir at room temperature overnight (cap the flask with a septum).

Purification

Evaporate most of the solvent using the rotovap. Prepare a silica gel column. **Warning:** Silica adversely affects the lungs! Only transfer/use in a fume hood and consider using a dust mask. Mix some silica gel in hexane to make a slurry. Pour the silica gel into the column (leave about an inch above the silica gel for solvent) Pour some hexane into the column to keep the solvent level above the silica gel. Slowly pour in the product mixture into the column. You should see brown-orange rings form around the top layers of the silica gel. The residue solid from the product mixture should just collect on top of the silica gel. Wash the original flask with some hexane and add it to the column. Run the hexane through the column multiple times by refilling the columns, making sure to not let the column dry which affects the separation. Collect the product and rotovap the mixture to remove most of the solvent. The concentrated product should be a turbid yellow color. Transfer the monomer into a 14/20 round bottom flask for distillation. A vacuum distillation setup is assembled, similar to the previous step. After distillation, the purified monomer should be clear, with a pale yellow color.

2.2.3 *2,5,-dibromo-3-ethylhexylthiophene*

3-ethylhexylthiophene was first synthesized from 3-bromothiophene following the same procedure as outlined in section 2.3.1 for 3-hexylthiophene. The difference being ethylhexylmagnesium bromide was used as the Grignard reagent. 3-ethylhexylthiophene was then brominated following the same procedure in section 2.3.2 to yield 2,5-dibromo-3-ethylhexylthiophene.

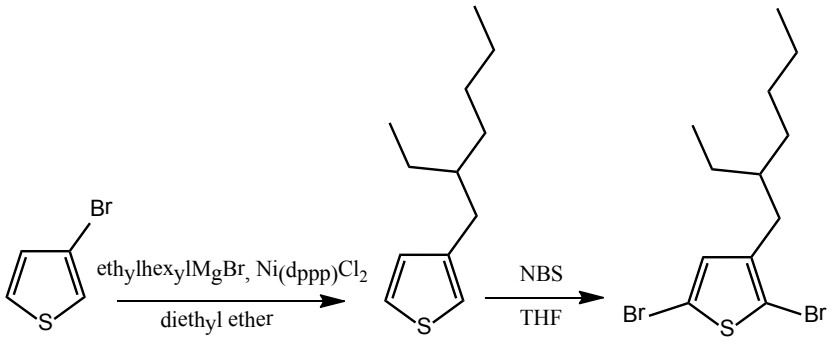

Figure 2.3. 2,5-dibromo-3-ethylhexylthiophene monomer synthesis scheme.

2.3 Polymer Synthesis

2.3.1 *Ethynyl-terminated poly*(*3-hexylthiophene*)

Compound	Mol. Weight (g/mol)	Mass/Vol.	Moles	Equivalents*
2,5-dibromo-3-hexylthiophene	324	6.48 g	0.02	---
***tert*-butylmagnesium chloride (2.0 M in diethyl ether)**	---	10 mL	0.02	1
ethynylmagensium bromide (2.0M in diethyl ether)	---	1 mL	0.002	---
Catalyst: $Ni(dppp)Cl_2$	542	0.100 g	1.85×10^{-5}	---
Solvent: THF	---	200 mL	---	---
Product: Ethynyl Terminated Poly(3-hexylthiophene)	---	~ 2 g	---	---

*relative to 2,5-dibromo-3-hexylthiophene

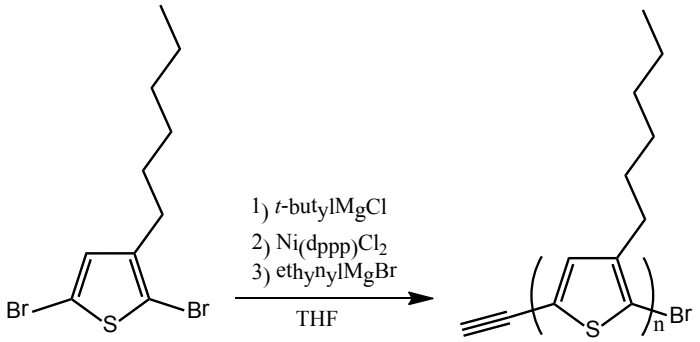

Figure 2.4. Ethynyl-terminated P3HT synthesis scheme following GRIM polymerization with in-situ end-group functionalization.

The GRIM polymerization method was used to synthesize regioregular P3HT.[89] 2,5-dibromo-3-hexylthiophene (6.52 g, 20 mmol) was added to a dry 500 mL, 3-neck round bottom flask that was purged with argon gas. Dried THF (20 mL) was added and stirred for another 15 minutes. Afterwards, 2M solution of t-butyl magnesium chloride in diethyl ether (10 mL, 20 mmol) was added and allowed to react for 2 hours in room temperature. The solution was further diluted with 180 mL of dried THF, then Ni(dppp)Cl_2 (0.175g, 0.323 mmol) was added to the reaction mixture. Ethynyl magnesium bromide was then added after 10 minutes and the reaction was quenched in methanol after an additional 3 minutes. The polymer was purified by sequential Soxhlet extractions with methanol, hexanes, and chloroform. The product was isolated from the chloroform solution to yield ca. 2 grams of ethynyl-terminated P3HT (63% yield). ^{1}H NMR ($CDCl_3$) 7.02 (s, 31H), 6.98 (s, 1 H), 3.57 (s, 1 H), 2.85 (t, 63 H), 2.61 (m, 4H), 1.73 (m, 64H), 1.39 (m, 59H), 1.30 (m, 132H), 0.97 (t, 100H).

2.3.2 *Allyl-terminated poly*(*3-hexylthiophene*) (Al-P3HT)

The same procedure outlined in 2.2.1 was used expect that allyl magnesium chloride was added 10 minutes after the addition of Ni(dppp)Cl_2.

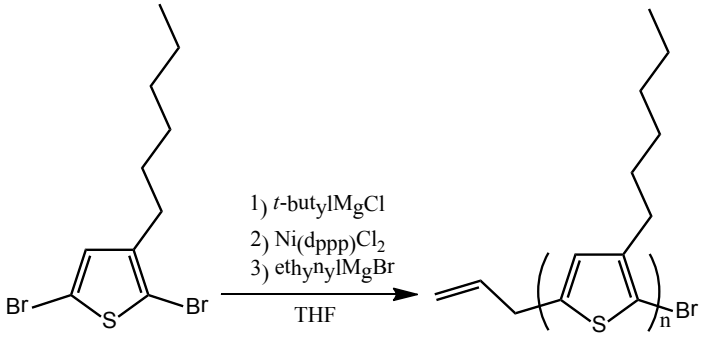

Figure 2.5. Allyl-terminated P3HT synthesis scheme following GRIM polymerization with in-situ end-group functionalization.

2.3.3 *Ethynyl-terminated poly(3-(2'-ethylhexyl)thiophene)* (Et-P3HT)

The GRIM polymerization method was used to synthesize regioregular P3EHT. 2,5-dibromo-3-ethylhexylthiophene (6.52g, 20 mmol) was then added to a dry 500 mL, 3-neck round bottom flask that was purged with argon gas. Dried THF (20 mL) was added and stirred for another 15 minutes. Afterwards, 2M solution of t-butyl magnesium chloride in diethyl ether (10 mL, 20 mmol) was added and allowed to react for 2 hours in room temperature. The solution was further diluted with 180 mL of dried THF, then Ni(dppp)Cl_2

(0.175 g, 0.323 mmol) was added to the reaction mixture. Ethynyl magnesium bromide in THF (6mL, 3mmol) was then added after 10 minutes and the reaction was quenched in methanol after an additional 3 minutes. The polymer was purified by sequential Soxhlet extractions with methanol, hexanes, and chloroform. The product was isolated from the chloroform solution.

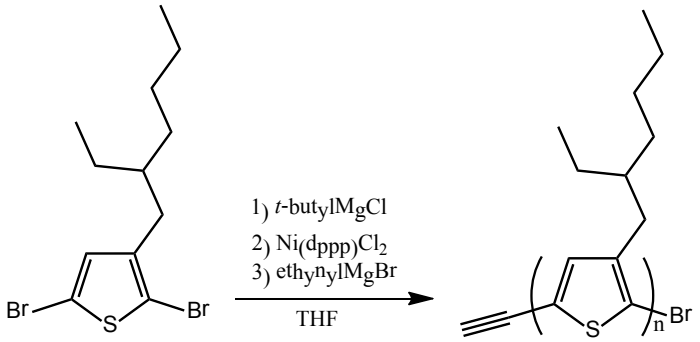

Figure 2.6. Ethynyl-terminated P3EHT synthesis scheme.

2.3.4 *Azide-functionalized poly(ethylene oxide)* (Az-PEO)

Table 2.3. Reagents for azide-functionalized PEO synthesis[90]

Compound	Mol. Weight (g/mol)	Mass/Vol.	Moles	Equivalents
Poly(ethylene oxide) methyl ether ($PEO\text{-}OCH_3$)	4200	5 g	1.20×10^{-3}	1
Triethylamine	101.19	~0.2 mL	---	1.1
Mesyl chloride	114.56	~0.1 mL	---	1.2
Solvent: THF	---	50 mL	---	---
Sodium Azide	65 g/mol	0.10 g	1.56×10^{-3}	1.3
95% Ethanol		50 mL		

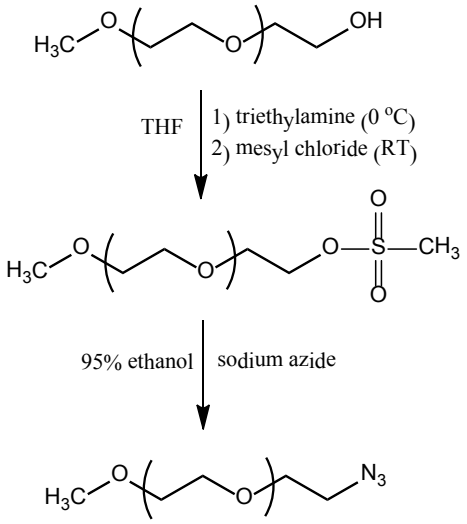

Figure 2.7. Azide-functionalized PEO synthesis scheme.

All required glassware are dried overnight in an oven set to >100°C prior to use. These are then removed from the oven and allowed to cool to room temperature. PEO-OCH_3 (mono methoxy PEO purchased from Polymer Source) is placed in a 100 mL 3-neck round bottom flask to dry under vacuum overnight. The system is then backfilled with Ar and THF solvent is added via syringe. A slight amount of heat may be applied just to dissolve the polymer, and then the reaction is allowed to cool to 0°C. Triethylamine is added *dropwise*. If the polymer reprecipitates, the temperature may be allowed to rise to RT to redissolve it, then brought down to 0°C again. Mesyl chloride is added *dropwise* and then allowed to react overnight at room temperature. **Warning: This is an exothermic step. Mesyl chloride should only be added slowly!** Solvent is then removed by rotary evaporation, and the solids are redissolved in 95% ethanol. Sodium azide is added to the solution, and the flask is outfitted with a condenser and placed under argon. The mixture is then allowed to reflux overnight. Sample aliquots may be taken to monitor the reaction by ^{1}H-NMR. When the reaction has finished, the solvent can then be removed by rotary evaporation, and the polymer is purified by redissolving in THF and washing with saturated NaCl aqueous solution. The polymer is then precipitated in hexane and rinsed with cold methanol. It is then dried under vacuum.

2.3.5 *Poly(3-hexylthiophene-block-ethylene oxide)* (P3HT-*b*-PEO)

Table 2.4. Reagents for P3HT-*b*-PEO synthesis

Compound	Mol. Weight (g/mol)	Mass/Vol.	Moles	Equivalents
Et-P3HT	6000	1.5 g	2.5×10^{-4}	1
Az-P3HT	2000	0.75 g	3.75×10^{-4}	1.5

CuI	190.5	0.003 g	1.6×10^{-5}	---
DIPEA	129.3	0.03 mL	1.7×10^{-5}	---
Solvent: THF	---	150 mL	---	---

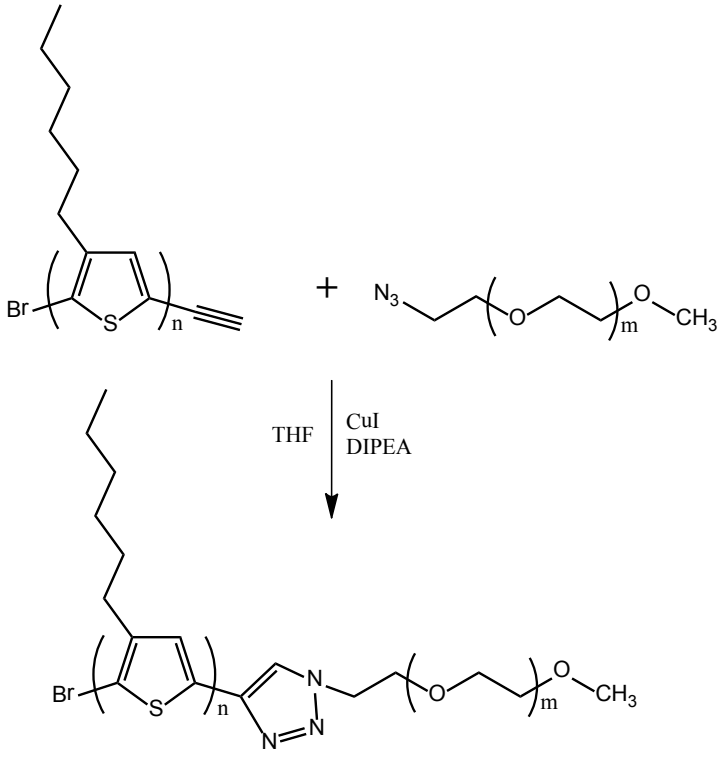

Figure 2.8. P3HT-*b*-PEO synthesis scheme using a 1,3-dipolar cycloaddition "click" reaction.

P3HT-*b*-PEO was synthesized using a 1,3-dipolar cycloaddition "click" reaction. Az-PEO (0.75 g, 0.375 mmol, Polymer Source) and Et-P3HT (1.5 g, 0.25 mmol) were placed in a dry 250-mL 3-neck round bottom flask and put under vacuum overnight. After refilling with Ar, 150 mL of dry THF was added to the reaction flask. The mixture was heated to ~40^{O}C and stirred for 15 minutes, or until the polymers were completely dissolved. Ar pressure inside the flask was increased, and CuI (0.003g, 0.016 mmol) was added quickly. DIPEA was added afterwards using a syringe (0.03mL, 0.017 mmol). The reaction was allowed to proceed at least 48 hours and then quenched in methanol. The polymer was filtered and purified by washing with copious amounts of methanol. The final product was then recovered from the chloroform solution to yield P3HT-PEO. ^{1}H NMR ($CDCl_3$) 7.86 (s, 1H),) 7.02 (s, 18H), 6.94 (s, 0.7H), 4.65 (t, 3H), 3.97 (t, 2H), 3.86 (t, 2H), 3.68 (m, 65H), 3.60 (m, 2H), 3.51 (t, 1H), 3.42 (s, 2 H), 2.85 (t, 37 H), 2.61 (m, 2H), 1.73 (m, 36H), 1.39 (m, 34H), 1.30 (m, 74H), 0.97 (t, 57H).

2.3.6 *Poly(3-(2'-ethylhexyl)thiophene-block-ethylene oxide)* (P3EHT-*b*-PEO)

Table 2.5. Reagents for P3EHT-*b*-PEO synthesis

Compound	Mol. Weight (g/mol)	Mass/Vol.	Moles	Equivalents
Et-P3EHT	5200	1.13 g	2.16×10^{-4}	1
Az-P3HT	2000	0.65 g	3.24×10^{-4}	1.5
CuI	190.5	0.003 g	1.6×10^{-5}	---
DIPEA	129.3	0.03 mL	1.7×10^{-5}	---
Solvent: THF	---	150 mL	---	---

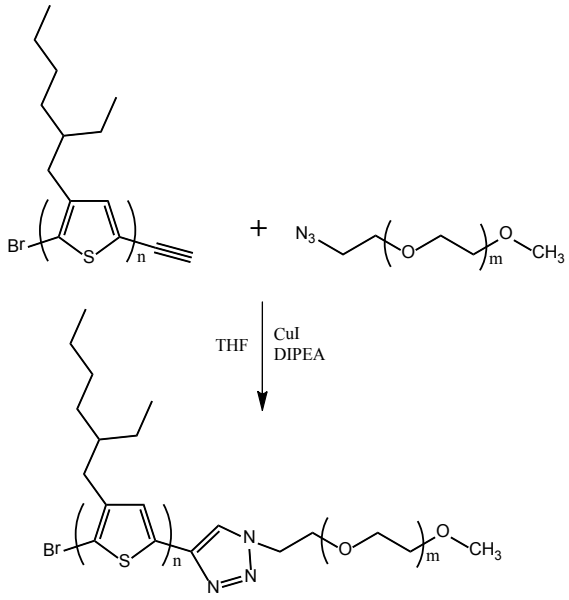

Figure 2.9. P3EHT-*b*-PEO synthesis scheme using a 1,3-dipolar cycloaddition "click" reaction.

P3EHT-*b*-PEO was synthesized using a 1,3-dipolar cycloaddition "click" reaction. Az-PEO (0.65 g, 0.324 mmol, Polymer Source) and Et-P3EHT(1.13 g, 0.216 mmol) were placed in a dry 250-mL 3-neck round bottom flask and put under vacuum overnight. After refilling with Ar, 150 mL of dry THF was added to the reaction flask. The mixture was heated to ~40°C and stirred for 15 minutes, or until the polymers were completely dissolved. Ar pressure inside the flask was increased, and CuI (0.003g, 0.016 mmol) was added quickly. DIPEA was added afterwards using a syringe (0.03mL, 0.17 mmol). The reaction was allowed to proceed at least 48 hours and then quenched in methanol. The polymer was filtered and purified by washing with copious amounts of methanol, washed with petroleum ether to remove any residual P3EHT homopolymer, and extracted with chloroform.

2.4 Polymer Characterization

2.4.1 *Characterization of Polymer using GPC*

The polymerization reactions were monitored using the GPC. In addition, the polydispersity index (PDI) of the homopolymers and block copolymers were measured using the GPC. Samples were run on a Viscotek Autosampler and TDA 302 GPC system, which included refractive index (RI), viscometer, light scattering, and UV detectors. GPC contained a set of three Styrogel HR columns (two HR3 and one HR4 columns) with tetrahydrofuran (THF) as eluent (flow rate of 1 mL/min, 35 °C). The GPC was calibrated with polystyrene (PS) standards. This provided PS equivalent PDI values of the polymers. We do not use the PS equivalent molecular weights in this study. Absolute molecular weight and PDI can be determined by using both RI and light scattering detectors. None of the polymers synthesized for this report used absolute molecular weight measurements. For reference, a more detailed explanation of absolute molecular weight measurements is given in Chapter 8.2. Representative GPC chromatographs are given below for P3HT-*b*-PEO and P3EHT-*b*-PEO and their precursors.

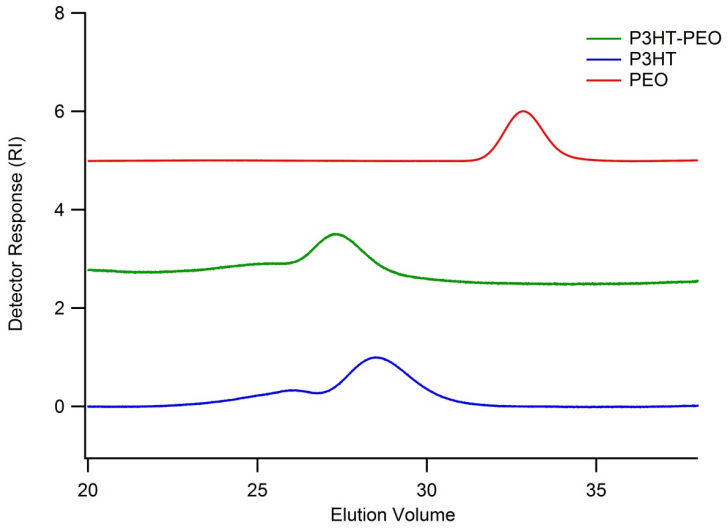

Figure 2.10. Representative GPC traces for P3HT and PEO homopolymer and the resulting P3HT-PEO block copolymer obtain via click reaction.

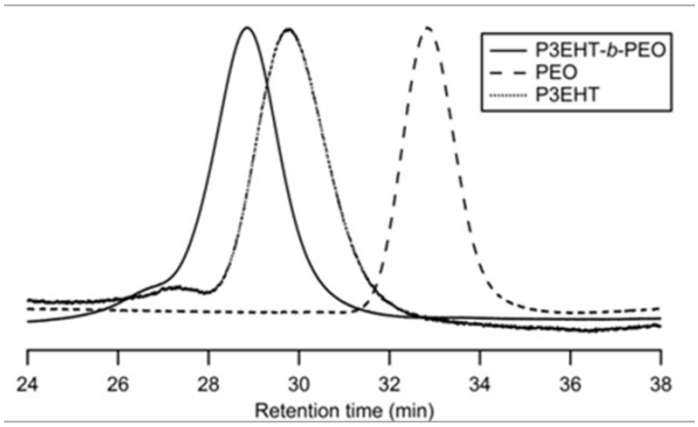

Figure 2.11. Representative GPC traces for P3EHT and PEO homopolymer and the resulting P3HT-PEO block copolymer obtained via click reaction.

2.4.2 *Characterization of Polymer using ^{1}H-NMR*

^{1}H NMR spectra were obtained on a Bruker AVG-400 or AVB-400 spectrometer using deuterated chloroform solutions to characterize synthesized monomers and polymers. Concentration of the solutions ranged from 10 to 15 mg/mL. In particular, ^{1}H NMR spectra were used to determine end-group functionalization, the number average molecular weight (M_n), and regioregularity of poly(3-hexylthiophene) homopolymers.

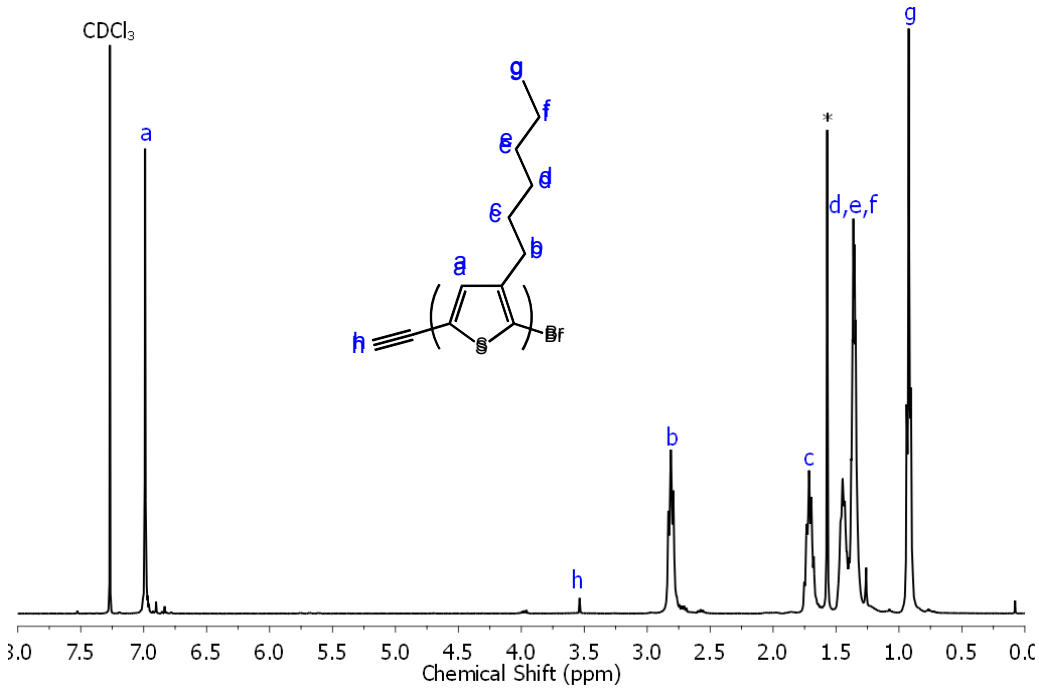

Figure 2.12. Representative ^{1}H-NMR spectrum of ethynyl-terminated P3HT (400 Mhz, $CDCl_3$). The * peak corresponds to water.

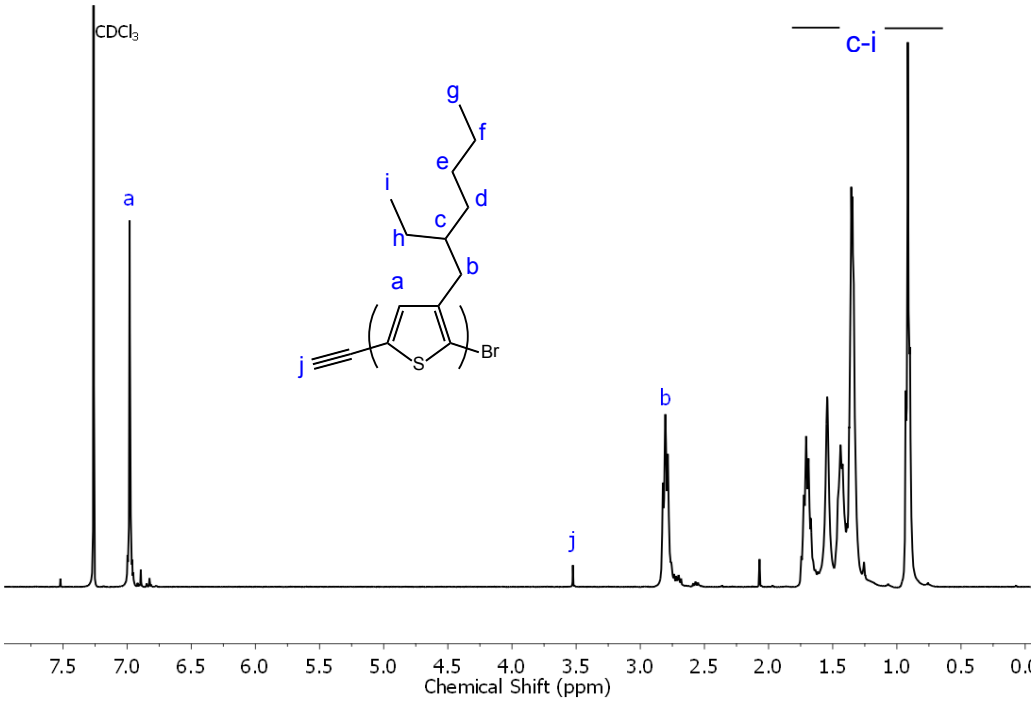

Figure 2.13. Representative ^{1}H-NMR spectrum of ethynyl-terminated P3EHT (400 Mhz, $CDCl_3$). The * peak corresponds to water.

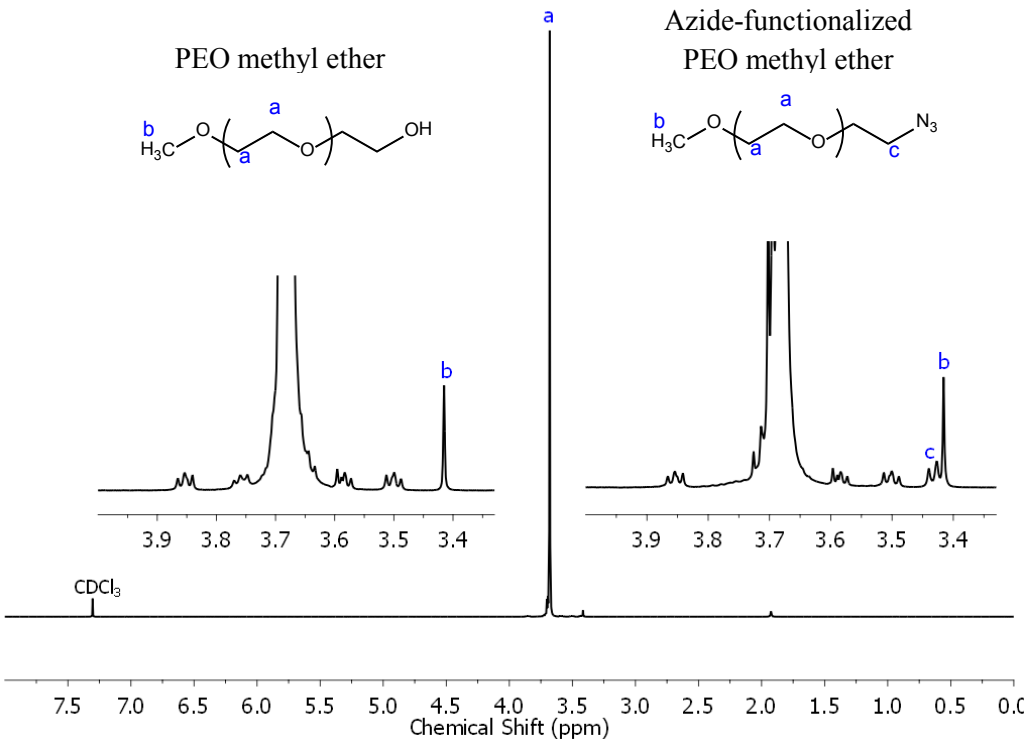

Figure 2.14. Representative ^{1}H-NMR spectrum of PEO methyl ether and azide-functionalized PEO methyl ether (400 Mhz, $CDCl_3$). After functionalization with an azide group, peaks appear near 3.44 ppm (labeled 'c' in the right inset). The peak at 3.4 ppm corresponds to the methyl end-group.

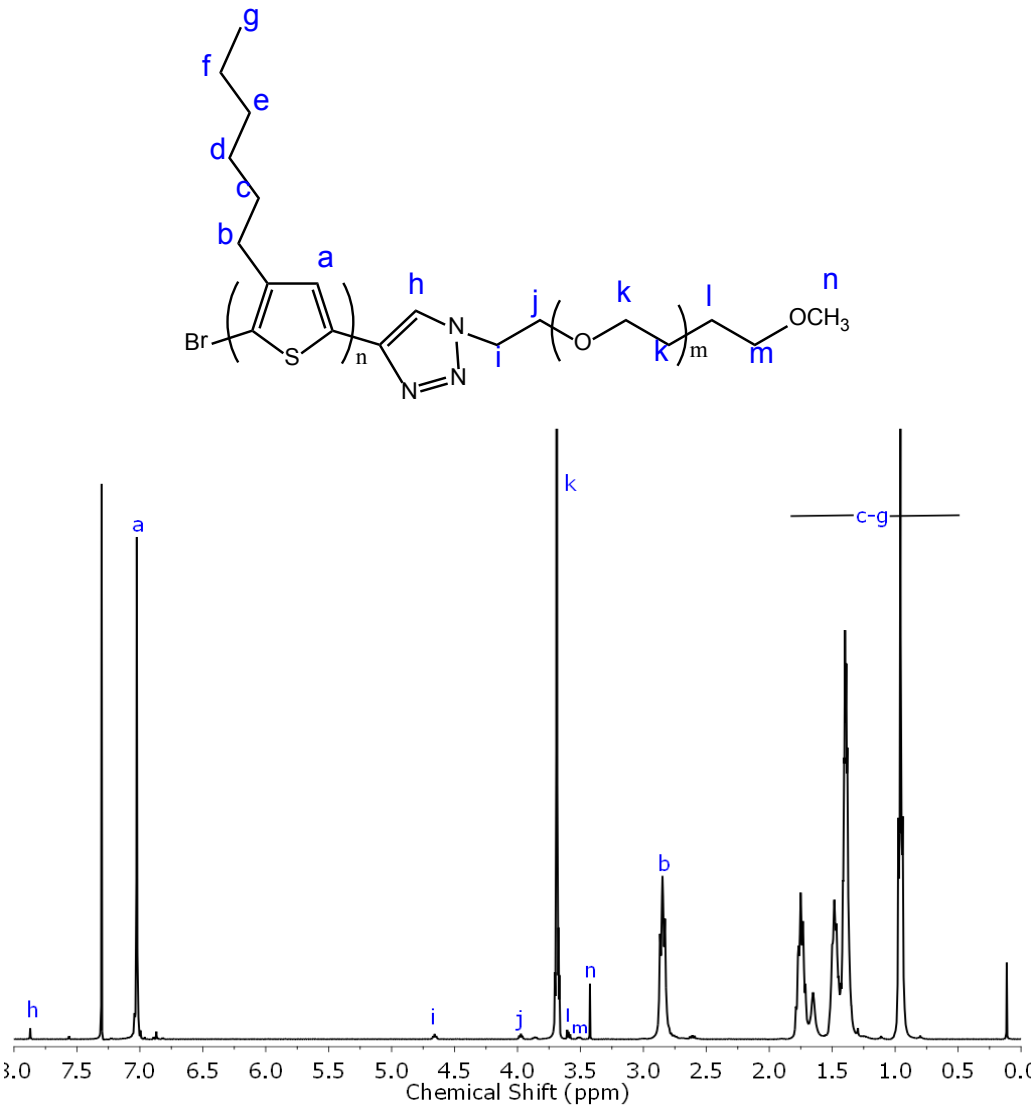

Figure 2.15. Representative ^{1}H-NMR spectrum of ethynyl-terminated P3HT-*b*-PEO (400 Mhz, $CDCl_3$).

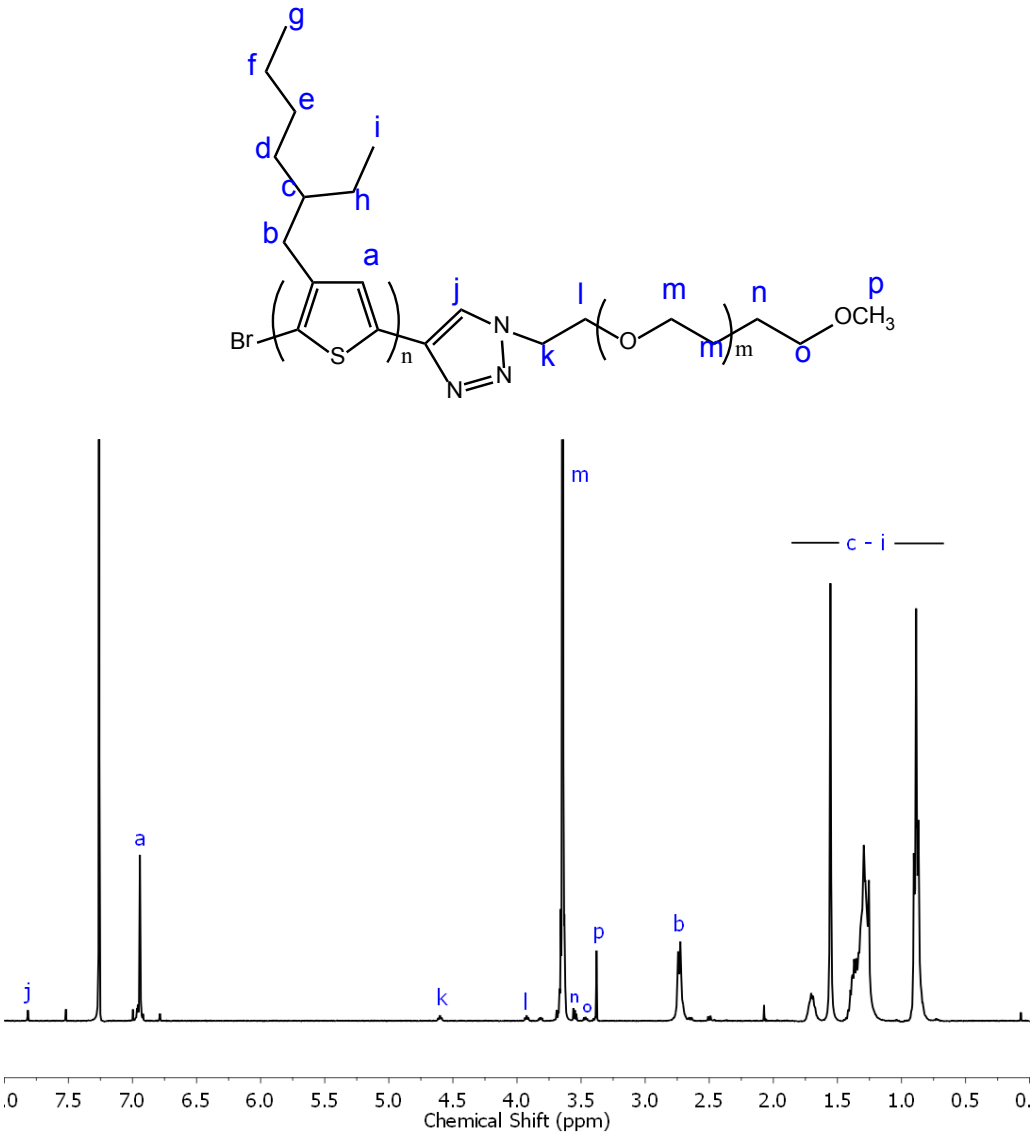

Figure 2.16. Representative ^{1}H-NMR spectrum of ethynyl-terminated P3EHT-*b*-PEO (400 Mhz, $CDCl_3$).

2.4.3 *Determination of Regioregularity using ^{1}H-NMR*

The regioregularity of P3HT can be determined using ^{1}H-NMR. In particular, the proton on the 4-position of the aromatic thiophene ring can be used to determine the regioregularity. The HT-HT triad sequence has a chemical shift, δ, of 6.98 ppm. A large signal at this chemical shift is highly indicative of a nearly perfect regioregular P3HT. Other triad sequences can be seen as well where TT-HT is at δ = 7.00 ppm, HH-HT is at δ = 7.03 ppm, and TT-HH is at δ = 7.05 ppm.[17, 18, 32] The integration of the HT-HT triad peak relative to the other triad peaks can give the percentage of HT-HT coupling (percent regioregularity). A representative ^{1}H-NMR spectrum is shown below indicating a highly regioregular P3HT.

For P3EHT, HT-HT is at at δ = 6.94 ppm, TT-HT is at δ = 6.96 ppm, HH-HT is at δ = 6.99 ppm, and TT-HH is at δ = 7.01 ppm. Alternatively, one can use the protons on the α-carbon of the 3-subsistuent to determine the regioregularity. The HT coupling is observed at δ = 2.80 ppm while HH coupling is observed at δ = 2.58 ppm.

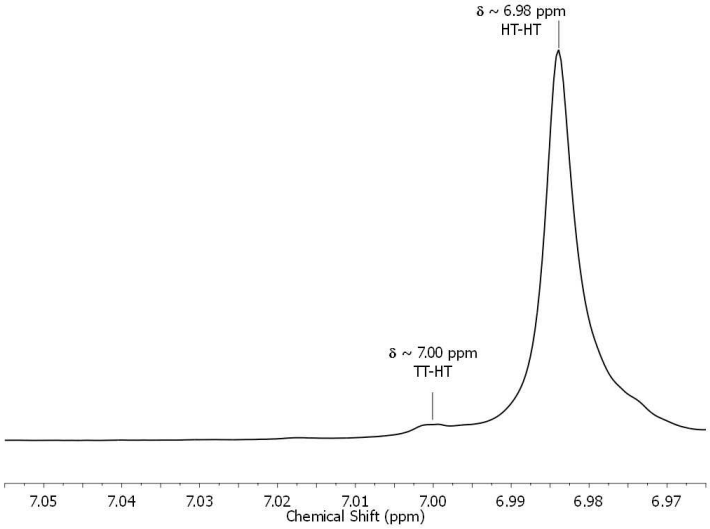

Figure 2.17. Representative expanded ^{1}H-NMR spectrum of a synthesized ethynyl-terminated P3HT homopolymer indicating high regioregularity. The integration of HT-HT peak is 49 while the integration of TT-HT is 2, which translates into a regioregularity of 96%. The TT-HT coupling always occurs because one TT dimer forms during the initial step of the GRIM polymerization. The HT-HH (δ = 7.02) and TT-HH (δ = 7.05) is not observed in the spectrum. Alternatively, one can use the protons on the α-carbon of the 3-subsistuent to determine the regioregularity. The HT coupling is observed at δ = 2.80 ppm while HH coupling is observed at δ = 2.58 ppm.

2.4.4 *Determination of Molecular Weight via ^{1}H-NMR*

The number average molecular weight (M_n) of P3AT can be determined through ^{1}H-NMR by using the relative integration of the protons associated with the α-carbon of the 3-subsistuent. It is important to note that α-carbon of the 3-subsistuent at the chain ends are in a different chemical environment than those of the other repeat units along the chains. As a result, the peak that corresponds to the protons associated with the α-carbon at the chain ends are at a lower chemical shift (δ ~ 2.60 ppm) relative to the protons of the α-carbon along the chain (δ ~ 2.80 ppm).[91] This observation allows for the determination of the molecular weight of the polymer via conventional end-group analysis. The degree of polymerization can be determined by simply dividing the peak integration at 2.80 ppm by the peak integration at 2.60 ppm. Then, multiplying by the repeat unit molecular weight will give M_n. It is important to remember to normalize the peak integration by the correct number of protons. Each α-carbon has two protons. The protons on the α-carbon at both chain ends are a total of four. A representative ^{1}H-NMR spectrum is shown below. This method provides a route to obtain an absolute molecular weight of P3HT.

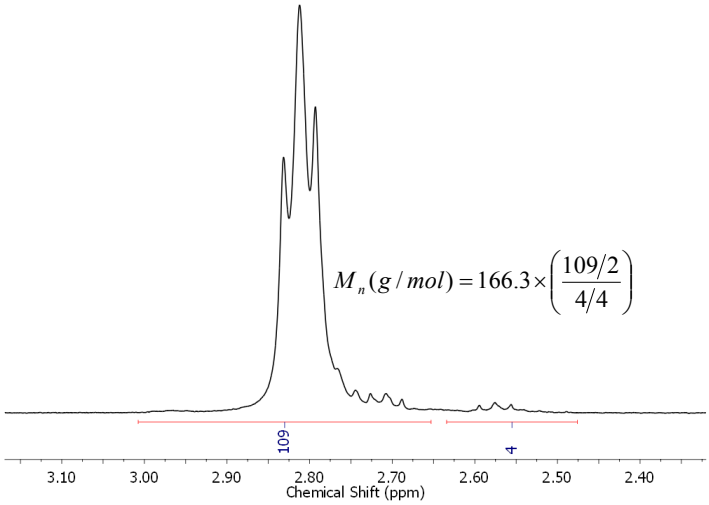

Figure 2.18. Representative expanded ^{1}H-NMR spectrum of a synthesized ethynyl-terminated P3HT homopolymer. These peaks correspond to the α-carbon of the 3-subsistuent. The multiplet that corresponds to the protons associated with the α-carbon at the chain ends are at δ ~ 2.60 ppm while the protons of the α-carbon of the other repeat units along the chains are at δ ~ 2.80 ppm. The end-group analysis yields a M_n of 9.0 kg/mol.

2.4.5 *Characterization of Polymer using Matrix-Assisted Laser Desorption Ionization - Time of Flight Mass Spectroscopy (MALDI-TOF MS)*

Matrix assisted laser desorption ionization – time of flight mass spectroscopy (MALD-TOF MS) is a versatile tool to characterize the mass for a variety of macromolecules such as proteins, peptides, polysaccharide, and, more recently, synthetic polymers. MALD-TOF is a soft ionization technique suitable for synthetic polymers (and other macromolecules) where fragmentation is an issue using conventional ionization techniques.[92-97] A MALDI-TOF MS sample consists of a dilute concentration of polymer embedded in a solid matrix, which is a crystalline molecule. The molar ratio of matrix to polymer is typically 500-1000. A UV laser beam (nitrogen, 337 nm) is shot at a polymer/matrix dried-droplet spot to promote desorption. The matrix absorbs the energy from the UV laser leading to vaporization of the top layer of the matrix. Next, the matrix ionizes the polymer chains. The charged polymer chains are accelerated by applying a high voltage to the sample plate and separated according to their mass-charge ratio (m/z) using a TOF mass analyzer. Most polymers are singly charged ions with a z of +1. To obtain good resolution MALDI spectra, the polymer should about molecular weight of 12 kg/mol or smaller. The sweet spot is 5 kg/mol (particularly for P3HT). Above 12 kg/mol value, polymer chains have a hard time "flying" as the mass is too large, which results in a spectra with poorly resolved peaks.

With MALDI-TOF MS, one can obtain the absolute molecular weight of a polymer. This is important because molecular weight of P3AT determined using a GPC is relative to a polystyrene calibration (when doing a conventional calibration).[92, 95] In addition to molecular weight, MALDI-TOF can be used to determine the end-group functionality of the polymer.

This is particularly useful when trying to confirm the extent of ethynyl end-group functionalization for P3AT. Ideally, with GRIM polymerization, one should obtain only Br/ethynyl end groups. However, other end groups such as H/ethynyl, ethynyl/ethynyl, Br/H, and H/H are possible. The end-group composition can be calculated knowing the repeat unit and end-group molar mass. For P3HT, peaks in a MALD-TOF spectrum correspond to 166.3*n* + EG1 + EG2, where n is the number of repeat units (g/mol), EG1 is the molar mass of one end-group, and EG2 is the molar mass the other end-group. The repeat unit molar mass for P3EHT is 194.3 g/mol. (Word of caution - I have noticed the ethynyl end-group can be easily cleaved during a MALDI experiment. Care needs to be taken when preparing the MALDI sample and use proper instruments settings to ensure no end-groups are cleaved. I believe using too much polymer in the in polymer/maxtrix was the main culprit of end-group cleavage).

One can take the intensity (absolute count) of each peak as the number of polymer chains (N) at a particular molecular weight (M_i). As a result, you can calculate absolute values for M_n, M_w, and PDI using the following basic equations.

$$M_n = \frac{\sum M_i N_i}{\sum N_i} \qquad M_w = \frac{\sum M_i^2 N_i}{\sum M_i N_i} \qquad PDI = \frac{M_w}{M_n} \tag{2.1}$$

MALDI-TOF spectra were obtained using Applied Biosystems Voyager-DE Pro instrument at the QB3/Chemistry Mass Spectrometry Facility. 1 mg of P3HT was dissolved in THF and 5 mg of 2,2':5',2"-tertthiophene matrix was dissolved in five drops of THF. One drop of the P3HT solution was mixed with two drops of tertthiophene solution. A drop of this mixture was placed on a MALDI plate to obtain an optimal homogenous solid mixture of the polymer and matrix. The spectra were obtained in linear TOF mode. Shown in Figure 2.19 and 2.20 are MALDI spectra corresponding to ethynyl-terminated P3HT and ethynyl-terminated P3EHT, respectively.

Table 2.6. Good starting point settings for MALDI-TOF MS instrument (linear mode)

Setting	Value
Mode of Operation	Linear
Extraction Mode	Delayed
Accelerating Voltage	20 kV
Grid Voltage	94%
Extraction delay time	500 nsec
Number of Laser Shots	200/spectrum

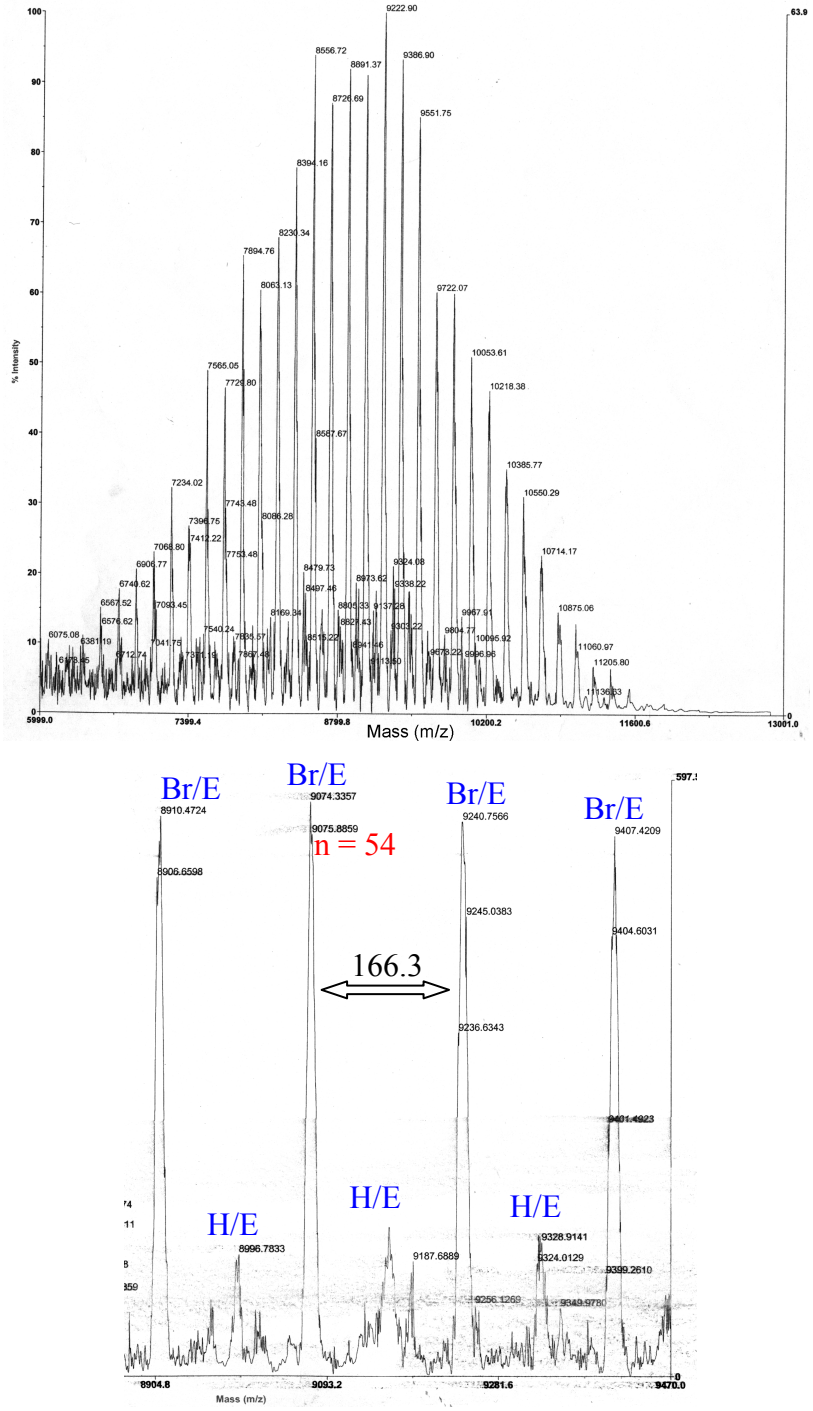

Figure 2.19. Representative MALDI-TOF spectra for ethynyl-terminated P3HT with labeled end-groups (where E=ethynyl group).

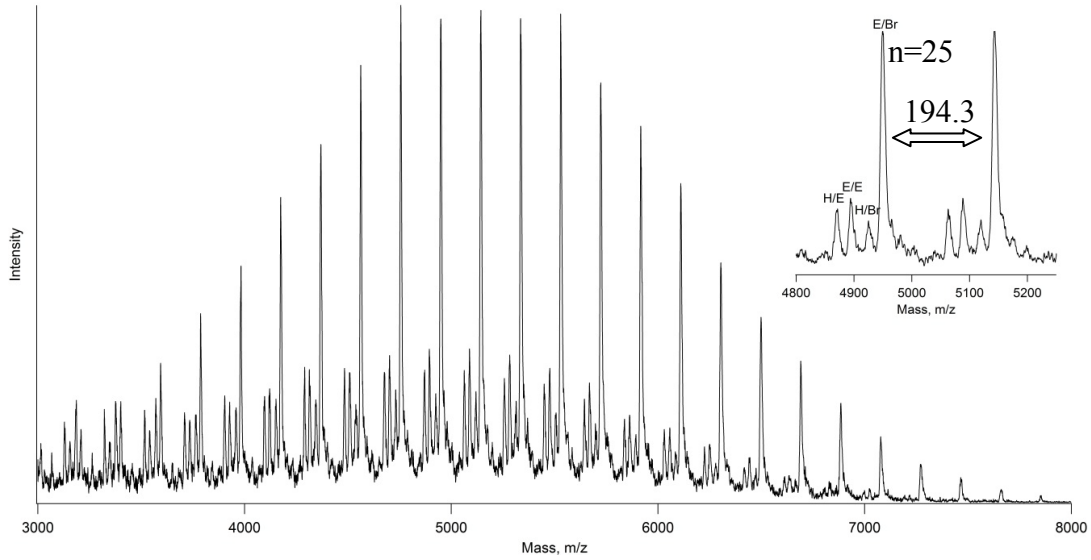

Figure 2.20. Representative MALDI-TOF spectra for ethynyl-terminated P3EHT with labeled end-groups (where E=ethynyl group).

2.4.6 *Differential Scanning Calorimetry (DSC)*

Melting points (T_m) and percent crystallinity of the polymers were determined using differential scanning calorimetry (DSC). DSC experiments were performed on a Thermal Advantage (TA) 2920 instrument. Samples were sealed in aluminum hermetic pans (salt-containing samples were prepared in an argon-filled glovebox). Heating/cooling runs were performed at 10 °C/min. Reported DSC data are from the third heating run unless stated otherwise. The ideal enthalpy of fusion for P3HT crystal is 99 J/g (used to calculate percent crystallinity).[98]

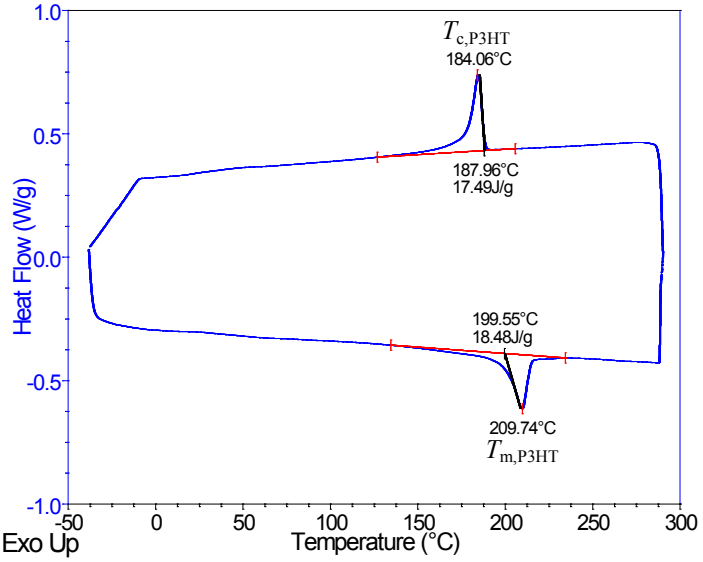

Figure 2.21. Representative DSC data for P3HT (5 kg/mol) (scan rate = 10 °C/min, 5.4 mg). T_m = melting temperature, T_c = crystallization temperature.

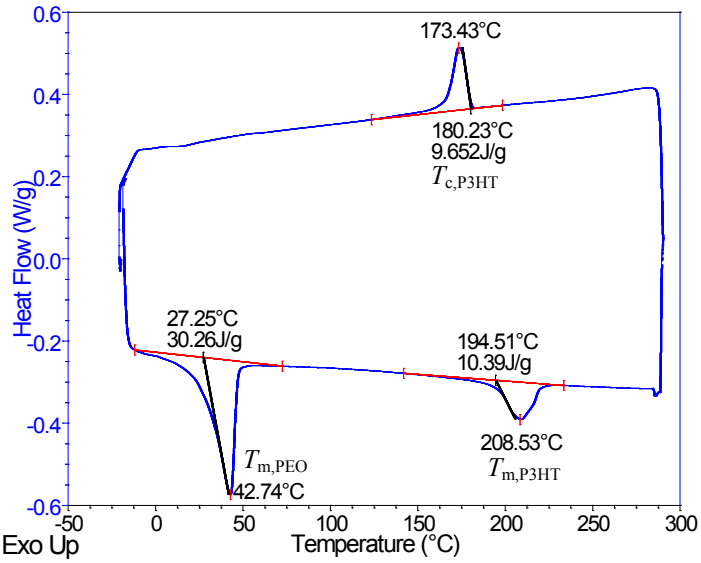

Figure 2.22. Representative DSC data for P3HT-*b*-PEO (scan rate = 10 °C/min, 4.7 mg). The P3HT M_n = 5 kg/mol and PEO M_n = 4.2 kg/mol. (T_m = melting temperature, T_c = crystallization temperature)

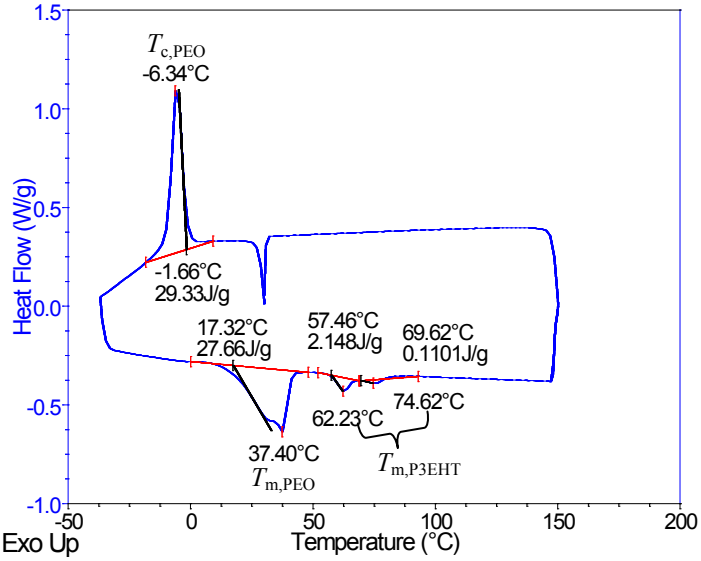

Figure 2.23. Representative DSC data for P3EHT-*b*-PEO (scan rate = 10 °C/min, 5.6 mg). The P3EHT M_n = 5 kg/mol and PEO M_n = 2 kg/mol. (T_m = melting temperature, T_c = crystallization temperature). P3EHT crystallization kinetics is much slower than P3HT. Therefore, an isothermal wait step of 90 minutes is needed at 30 °C to crystallize P3EHT.

2.4.7 *Ultraviolet-Visible (UV-VIS) Spectroscopy*

UV-VIS spectroscopy is powerful tool to characterize the π-orbital overlap of a conjugated polymer.[99] The absorption peaks is related to the $\pi-\pi^*$ transition, which tells the

extent of conjugation in the polymer. In solution, regioregular P3ATs have one absorption peak, but varies in wavelength depending on (λ) due to the solvatochromism of P3HT.[100] In THF, P3HT has absorption maximum at λ = 447 nm,[100] while P3EHT has absorption maximum at 437 nm. In the solid-state, P3ATs show three distinct shoulders/peaks corresponding to different conformational structures with different conjugation lengths (λ = 527 nm, 558 nm, 602 nm for P3HT[100] and λ = 496 nm, 537 nm, 572 nm for P3EHT[101]). Higher the value of λ means greater long-range order (higher degree of conjugation).

UV-Vis measurements were made with Varian Cary 50 instrument between 400 and 1000 nm. Solution-based UV-Vis data were obtained by using a 5 µg/mL polymer solution in THF. For salt-containing solutions, a custom built air-tight cuvette was used when obtaining the data. Solid-State UV-Vis data were obtained by drop casting 1 mg/mL polymer solution in THF onto a glass slide. For salt-containing samples, the glass slides were impulse sealed between two polypropylene sheets to ensure no exposure to water and air. The background was corrected for the glass slide and polypropylene sheets.

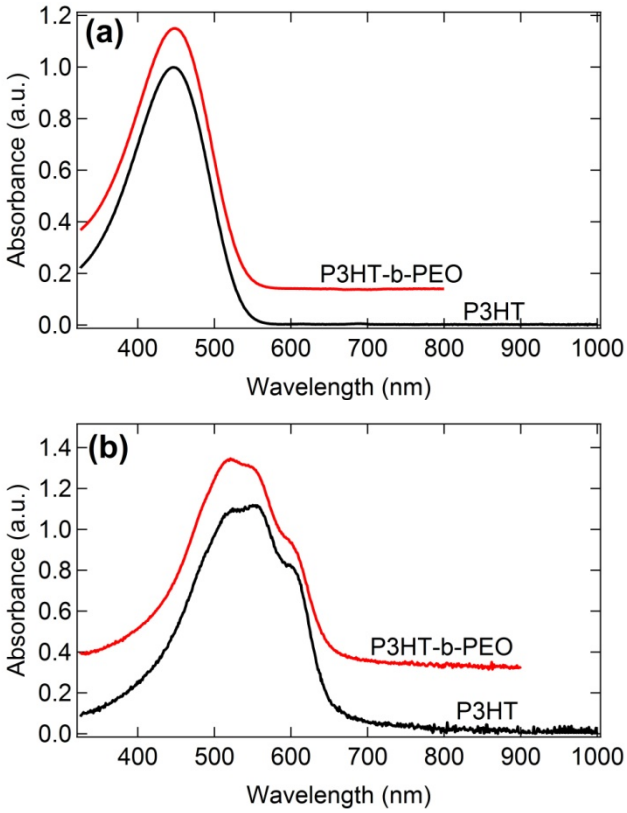

Figure 2.24.(a) Solution UV-VIS (THF) of P3HT (5 kg/mol) and P3HT-*b*-PEO (6k-2k). The maximum absorption is at λ = 447 nm for P3HT and λ = 449 for P3HT-*b*-PEO. (b) Solid-state UV-VIS (THF) of P3HT (5 kg/mol) and P3HT-*b*-PEO (5k-4.2k). The maximum absorption peaks/shoulders are at λ = 525, 558, 608 for P3HT and λ = 520, 554, 603 for P3HT-*b*-PEO (5k-4.2k).

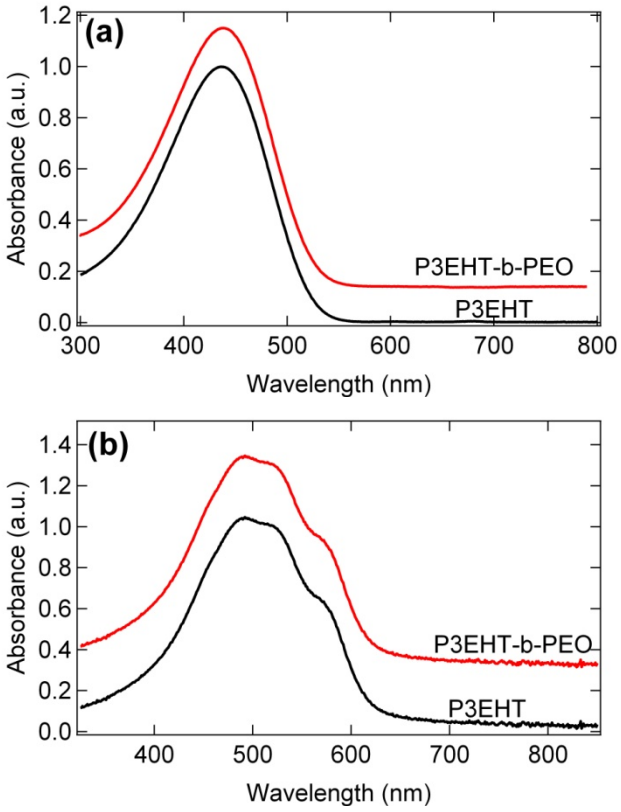

Figure 2.25.(a) Solution UV-VIS (THF) of P3EHT (5 kg/mol) and P3EHT-*b*-PEO (5k-2k). The maximum absorption is at λ = 437 nm for P3EHT and λ = 449 for P3EHT-*b*-PEO. (b) Solid-state UV-VIS (THF) of P3EHT (5 kg/mol) and P3EHT-*b*-PEO (5k-2k). The maximum absorption peaks/shoulders are at λ = 495, 528, 578 for P3EHT and λ = 495, 528, 578 for P3EHT-*b*-PEO (5k-2k).

2.5 Summary of Important Properties of Synthesized Polymers

Table 2.7. Characteristics of pertinent polymers used in this dissertation.

Polymer Name	$M_{n,P3HT}$[a] (kg/mol)	$M_{n,PEO}$[a] (kg/mol)	RR[b] (%)	ϕ_{P3AT}[c]	PDI[d]
P3HT(5)	5.0	---	>98	1	1.2
P3HT-PEO(9-2)	9.0	2.0	>98	0.81	1.27
P3HT-PEO(6-2)	6.0	2.0	>95	0.74	1.33
P3HT-PEO(5-4)	5.0	4.2	>95	0.53	1.30
P3EHT-PEO(5-2)	5.0	2.0	>95	0.72	1.06

[a]M_n = number-average molecular weight and [b]RR = regioregularity, which were determined using ^{1}H-NMR. [c]Calculated using density of 1.10 g/mL for P3HT and 1.07 for P3EHT and PEO density of 1.06 g/mL. [d]PDI = polydispersity index as determined through gel permeation chromatography with polystyrene standards

Table 2.8. Characteristics of pertinent polymers used in this dissertation continued.

Polymer Name	$T_{m,PEO}$ °C	$T_{m,P3HT}$ °C	% crystallinity of P3AT	Solution UV-VIS (THF) λ (nm)	Solid-State UV-VIS λ (nm)
P3HT(5)	---	215	23	447	525, 558, 608
P3HT-PEO(9-2)	not observed	218	23	450	528, 562, 611
P3HT-PEO(6-2)	not observed	210	22	449	523, 556, 605
P3HT-PEO(5-4)	58	209	20	440	520, 554, 603
P3EHT-PEO(5-2)	40*	64 , 77	---	410	495, 528, 578

*The crystallization temperature is at -6 °C.

Chapter 3 - Morphology and Thermodynamics of Poly(3-alkylthiophene-*block*-ethylene oxide)[†]

ABSTRACT

We report on the morphology and thermodynamics of P3AT-PEO block copolymers. The morphologies of asymmetric copolymers with P3HT as the major component are dominated by nanofibrils. In contrast, the nearly symmetric P3HT-PEO copolymer used in this study self-assembles into a lamellar phase. We show that in the melt state, the P3EHT-*b*-PEO chains self-assemble to produce traditional nanoscale morphologies such as lamellae and gyroid. This is in contrast to a majority of previous studies on copolymers with electronically conducting blocks wherein a nanofibrillar morphology is obtained. The segregation strength between the two blocks is controlled through the addition of lithium bis(trifluromethanesulfonyl) imide (LiTFSI). Our approach enables estimation of the "effective" Flory-Huggins interaction parameter, χ_{eff}, using the random phase approximation (RPA). The χ_{eff} trends with salt concentration suggest that the TFSI anion preferentially segregates into the P3EHT phase while Li^+ remains in the PEO phase. For the salt-free sample, the gyroid morphology, obtained in the melt-state, is transformed into lamellae below the melting temperature of the P3EHT block. This is due to the "breaking out" of the crystalline phase. For the salt-containing sample, P3EHT-*b*-PEO has a lamellar morphology in both melt and crystalline states (confined crystallization).

3.1 Introduction

Nanostructuring of electronically conducting domains is important for a wide range of applications related to clean energy. Organic solar cells require nanoscale electron- and hole-conducting domains to promote charge separation and extraction.[102] Battery and fuel cell electrodes based on active materials that are either electronic or ionic insulators (e.g. lithium iron phosphate or platinum) require nanoscale electron- and ion-conducting domains.[103, 104] Copolymers with electronically conducting block such as poly(3-alkylthiophenes) (P3AT) appear to be perfectly suited for such applications.[105] It is thus not surprising that many research groups have focused on the synthesis and characterization of block copolymers containing P3AT.[100, 106-108] The formation of nanoscale domains such as alternating lamellae and the cubic gyroid phase in block copolymers[59] is well established and such morphologies are ideally suited for the applications listed above. Unfortunately, the

[†] Parts of this chapter have been reported in *ACS Nano*. **2012**, *6* (2), 1589-1600 and *Nano Letters* **2012**, *12* (9), 4901-4906.

crystallization of most electronically conducting polymers disrupts these morphologies; a vast majority of publications on P3AT report the formation of crystalline nanofibrils with no evidence of conventional domain morphologies seen in block copolymers.[100, 106-108] Notable exceptions are the reports from Ho et al.[109] and Moon et al.[110], who report the formation of conventional morphologies in a P3AT-contiaining block copolymers that have reduced melting temperatures. The common feature in these studies is that the non-conducting blocks have a high glass transition temperature, and the inability of glassy polymers to conduct either electrons or ions is well established.

A framework has been established to predict the self-assembly of copolymers with one non-conducting crystallizable block and one amorphous block.[72-75, 77-80, 111, 112] The morphology obtained in these systems is dictated by the chemical incompatibility of the two blocks (χ, Flory-Huggins interaction parameter), the free energy of crystallization, and the glass transition temperature of the amorphous block.[72-75, 77-80, 111, 112] When the amorphous block is glassy, the morphology of the melt-state is retained and the crystallization of the second block is confined within the nanoscale domains.[74, 77, 78, 113] When the amorphous block is rubbery, the morphology in the crystalline-state depends on both segregation strength (χN, where N is the number of monomers per chain) between the blocks and the free energy of crystallization.[72, 74, 77, 79] The melt-state morphology is retained only in strongly segregated systems.[77, 79, 111] In weakly segregated systems, the crystalline phase "breaks out" of the confining block copolymer domain.[72-74, 79, 80, 112] The morphology of the crystalline phase is often lamellar as this geometry is commensurate with that of chain folded crystals.[72, 74, 112, 114, 115] This was first anticipated by theorists[114, 115] and subsequently observed experimentally.[72, 74, 112]

Poly(3-hexylthiophene) (P3HT) is a highly studied semicrystalline polymer system due to its high electronic charge carrier mobility.[116, 117] P3HT has a high melting temperature (<230 °C) and is dominated by crystallization through strong π-π interactions. As a result, the morphology of P3HT-containig block copolymers have nanofibrillar superstructure.[100, 106-108] Variations in the alkyl side chain of the thiophene block can have a large effect on the crystalline and liquid crystalline properties of poly(3-alkylthiophene)s (P3ATs). For example, poly(3-dodecylthiophene) (P3DDT) has a lower melting point (125 °C) and reduced rod-rod interactions relative to P3HT.[101] Moon et al. show that one can obtain traditional block copolymer morphologies with P3DDT-*b*-poly(methyl methacrylate) (P3DDT-*b*-PMMA) by varying the molecular weight of P3DDT and PMMA, thus controlling the segregation strength.[110] The nanofibril morphology is only obtained when the total molecular weight is reduced and P3DDT is the majority block. Importantly, the crystalline nature of P3DDT is retained in the nanoscale domains for the whole composition window.

In addition to P3HT and P3DDT, the introduction of a branched alkyl side chain, such as in poly(3-(2'-ethylhexyl)thiophene) (P3EHT), causes the polymer to have a lower melting temperature (60-80 °C) and reduced rod-rod interactions.[101] The P3EHT homopolymers and P3EHT-containing block copolymers[109] have been shown to crystallize similarly to P3HT by forming the π-π stacked polymer chains,[118] and also has comparable optical and charge transport properties to those of P3HT.[109, 118, 119] The use of a P3AT-derivative with a lowered crystallization temperature can affect the self-assembly of P3EHT rod–coil block copolymers. Ho et al. have observed traditional block copolymer morphologies with a P3EHT-*b*-polylactide (P3EHT-*b*-PLA) system.[109] This result is consistent with the framework described above; confined crystallization can be attributed to the low

crystallization temperature of P3EHT, the glassy nature of the non-crystalline block, and the strong segregation strength between the two blocks.

In this chapter, we first report on the morphology of P3HT-PEO block copolymers with and without the addition of the salt lithium bis(trifluromethanesulfonyl) imide (LiTFSI). We extend our morphology study to a P3EHT-PEO block copolymer. We show that P3EHT-*b*-PEO can self-assemble to form lamellar and gyroid morphologies. We also show that the morphology is affected by the addition of LiTFSI. Using absolute small-angle X-ray scattering data (SAXS), we estimate the "effective" Flory-Huggins interaction parameter, χ_{eff}, by applying the random phase approximation (RPA). This is the first report of the application of RPA for P3AT-containing block copolymers.

3.2 Experimental Methods

3.2.1 *Salt Sample Preparation*

All of the steps used to make the P3AT-*b*-PEO/LiTFSI mixture were conducted in argon-filled gloveboxes (MBraun and Vacuum Atmospheres). LiTFSI was purchased from Novolyte and dried under vacuum at 120 °C for 3 days to remove residual water. Neat P3EHT-*b*-PEO was dried at 50 °C under vacuum for 6 days before making salt samples. P3HT-*b*-PEO was dried at 90 °C dried under vacuum for 3 days before making salt samples. LiTFSI/anhydrous THF mixtures were prepared in a volumetric flask at a concentration of 0.75 g/mL. The P3AT-*b*-PEO samples were dissolved in anhydrous benzene at a concentration of 10 mg/mL in scintillation vials. Some heating is needed to dissolve P3HT-*b*-PEO while P3EHT-*b*-PEO should dissolve at room temperature. LiTFSI/anhydrous THF solution was added to the polymer solution to obtain the desired salt concentration. The P3AT-PEO salt solutions were stirred overnight to ensure good mixing and placed in an air-tight desiccator, which was transferred into a freeze drying unit. The process ensured no exposure to air and water.

3.2.2 *Small-Angle X-ray Scattering and Wide-Angle X-ray Scattering*

Small-angle X-ray scattering (SAXS) can be used to determine the morphology of block copolymers with a characteristic periodic length scale from 5 – 100 nm. With wide-angle X-ray scattering (WAXS), one can characterize the crystalline morphology of each polymer chain. WAXS is equivalent to commonly used X-ray powder diffraction. Both SAXS and WAXS experiments were performed under transmission mode. For both SAXS and WAXS data, the measured two-dimensional scattering data were averaged azimuthally to obtain intensity (I) *vs.* magnitude of the scattering wave vector $q=4\pi\sin(\theta/2)/\lambda$, where λ is the wavelength of the incident X-rays and θ as the scattering angle.

For scattering experiments, polymer samples were pressed into 125 μm thick Garolite spacer and placed in an airtight sample holder with Kapton windows. The samples were annealed overnight under vacuum at 130 °C. SAXS and WAXS measurements were taken at the Advanced Light Source (ALS) beamline 7.3.3 at Lawrence Berkeley National Lab. A

silver behenate sample was used as a standard for SAXS. The 2D scattering patterns were collected on a 1M Pilatus detector. The scattering patterns were reduced using the Nika macro for Igor Pro developed by Jan Ilavsky at Argonne National Laboratory. WAXS measurements were also taken at Stanford Synchrotron Radiation Lightsource (SSRL) beamline 1-4. A combination of silver behenate and silicon oxide was used as the calibrant. The SSRL WAXS scattering patterns were reduced using a program developed by John Pople (a staff scientist at SSRL).

3.2.3 *Transmission Electron Microscopy (TEM)*

TEM can be used to determine the morphology of a block copolymer. TEM samples were prepared in an argon-filled glovebox by dip coating a copper grid in polymer/THF solution (10 mg/mL) and dried under vacuum. TEM samples were transferred in an air-tight desiccator to the microscope to limit air/water exposure. Bright field TEM images were obtained using a Ziess LIBRA operating at 200 kV.

3.2.4 *Random Phase Approximation (RPA)*

The scattering wave vector, q, dependence of the scattering intensity (I) is from a disordered diblock copolymer melt as obtained by Leibler[61] (within the random phase approximate, RPA) is given by[120]

$$I(q)=\left(\frac{b_A}{v_A}-\frac{b_B}{v_B}\right)^2\left\{\frac{S^0_{AA}+S^0_{BB}+2S^0_{AB}}{S^0_{AA}S^0_{BB}-\left(S^0_{AB}\right)^2}-\frac{2\chi}{v}\right\}^{-1} \tag{3.1}$$

where A and B refer to the two blocks, b_i and v_i the scattering lengths and volumes, χ is the Flory-Huggins interactions parameter, and a reference volume of v = 1 nm^3, and S_{ij} are the ideal correlations between blocks A and B in the absence of interactions.

$$\boldsymbol{S^0_{ii}=\phi_i N_i v_i P_i(q)\ \ (i=A,B)} \tag{3.2a}$$

$$\boldsymbol{S^0_{AB}=\left(\phi_A N_A v_A \phi_B N_B v_B\right)^{1/2} F_A(q) F_B(q)} \tag{3.2b}$$

N_i is the number of monomers in block i, ϕ_i is the volume fraction of the block, and v_i is the monomer i volume. $P_i(q)$ and $F_i(q)$ are the intrablock and interblock correlations as described by Debye and Leibler, respectively:

$$\boldsymbol{P_i(q)=2\frac{\exp(-u_i)-1+u_i}{u_i^2}\ \ (i=A,B)} \tag{3.3a}$$

$$F_i(q) = \frac{1 - \exp(-u_i)}{u_i} \quad (i = A, B) \tag{3.3b}$$

where $u_i = q^2 N_i l_i^2/6$ and l_i is the statistical segment length of block *i*.

The SAXS disorder peak was fit to equation 3.1 by adjusting l_{EHT}, χ, and $(b_A/v_A - b_B/v_B)^2$. All other parameters are known and reported in literature.[121] The density of P3EHT used in this study is 1.07 g/cm^3 at 25 °C. The density at other temperatures were determined knowing that the volumetric thermal expansion coefficient $(d \ln V/dT)$ is approximately 4 x10^{-4} K^{-1} for most polymers.

3.3 Results and Discussion

3.3.1 *P3HT-b-PEO Morphology*

In Table 2.7, we list the characteristics and nomenclature of the P3HT-PEO block copolymers used in this portion of the Chapter 3. Figure 3.1a shows the small angle X-ray scattering (SAXS) intensity, *I*, *versus* magnitude of the scattering vector, *q*, of P3HT-PEO(9-2) at 90 °C in the absence and presence of salt at r_0 = 0.085, where r_0, the molar ratio of lithium ions to ethylene oxide moieties. The neat sample (r_0 = 0) produces a featureless scattering profile. However, with the addition of salt, the scattering profile shows a broad primary peak at $q = q^*$ = 0.29 nm^{-1} corresponding to a characteristic periodic length scale, *d* = 22 nm ($d=2\pi/q^*$) and another broad peak at q = 0.50 nm^{-1}. Similar data are obtained from P3HT-PEO(6-2) as shown in Figure 3.1b. The SAXS profile of neat P3HT-PEO(6-2) at 90 °C is featureless, but the addition of salt at r_0 = 0.085 results in broad peaks at q^* = 0.37 nm^{-1} and q = 0.74 nm^{-1}, corresponding to *d* = 17 nm. The broad peaks seen in Figure 3.1 are not characteristic of traditional block copolymer morphologies and are thus likely to be indications of the often-reported nanofibrillar morphology in P3HT-containing block copolymers.

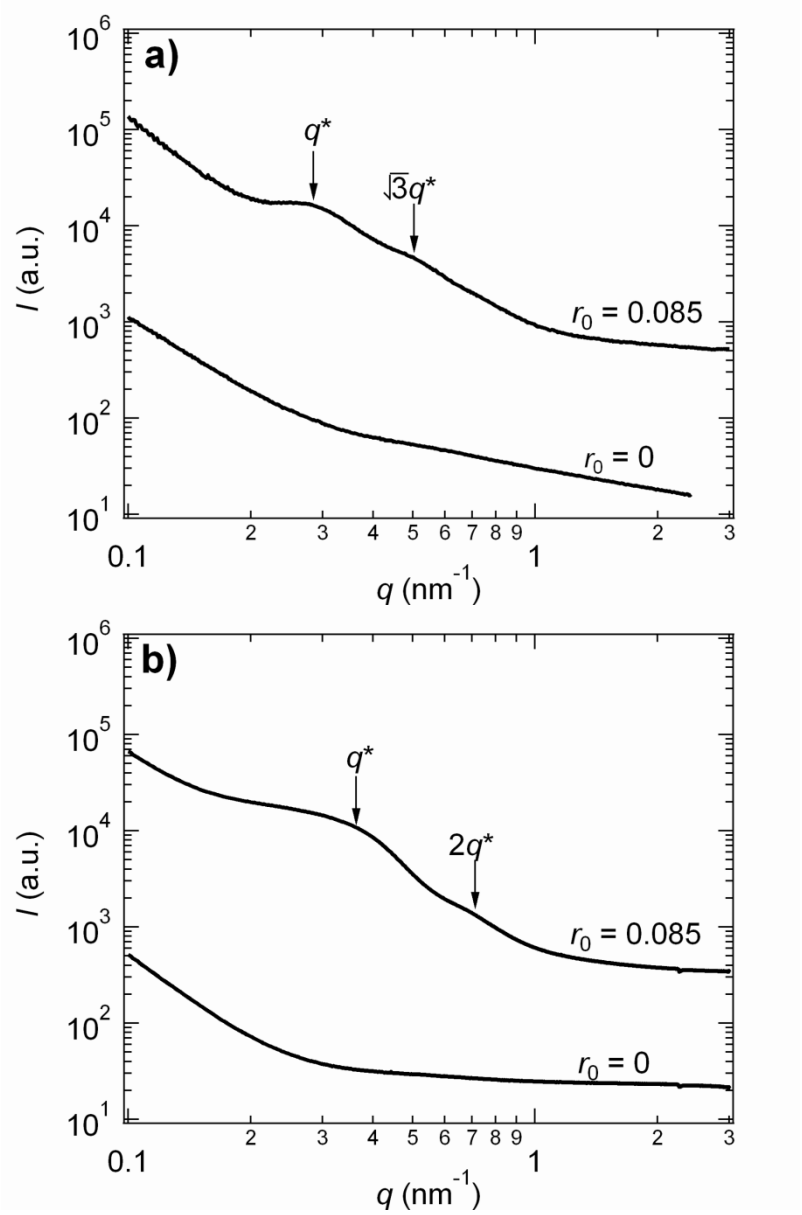

Figure 3.1. **(a)** SAXS of P3HT-PEO(9-2) and **(b)** P3HT-PEO(6-2) at 90 °C. The SAXS profile at $r_0 = 0$ is featureless while the addition of LiTFSI (r_0=0.085) indicates the presence of microphase separation. The features shown here are seen at all temperatures from 28 to 160 °C.

Dramatically different results are obtained from neat P3HT-PEO(5-4) as shown in Figure 3.2a. At room temperature, the SAXS profile contains a primary peak at $q^* = 0.28$ nm^{-1} and a higher order peak at $2q^*$ indicative of a lamellar phase corresponding to a domain spacing, d (the center-to-center distance between adjacent PEO lamellae), of 22.5 nm. A featureless SAXS profile is obtained when the sample temperature is increased to 60 °C, indicating the disappearance of the lamellar morphology. The lamellar peaks return when the sample is cooled to room temperature. It is not clear if the high temperature phase in P3HT-PEO(5-4) contains nanofibrils. In Figure 3.2b, we show the SAXS profile of P3HT-PEO(5-4) at $r_0 = 0.085$ at room temperature and 90 °C. At both temperatures we observe peaks at q^*

= 0.31 nm^{-1} and $2q^*$ indicating the presence of a lamellar structure with d = 20.3 nm. The lamellar structure of P3HT-PEO(5-4) at r_0 = 0.085 was confirmed by TEM as shown in the inset of Figure 3.2b. There is good agreement between the length scale of the periodic structure determined by SAXS and TEM (about 20 nm). It should be noted that the TEM sample was not stained, *i.e.* the natural electron density contrast between P3HT and PEO in the presence of LiTFSI is responsible for the image. The TEM image contained isolated dark features as shown in Figure 3.2b. This may be due to residual homopolymers or some other contaminant in our samples. TEM images of P3HT-PEO(6-2) and P3HT-PEO(9-2) did not contain any discernible features. The SAXS results for all P3HT-PEO block copolymers indicate that the addition of LiTFSI enhances the microphase separation (Figures 3.1-2). This is also true in polystyrene-*b*-poly(ethylene oxide) (PS-PEO) block copolymers.[85, 122]

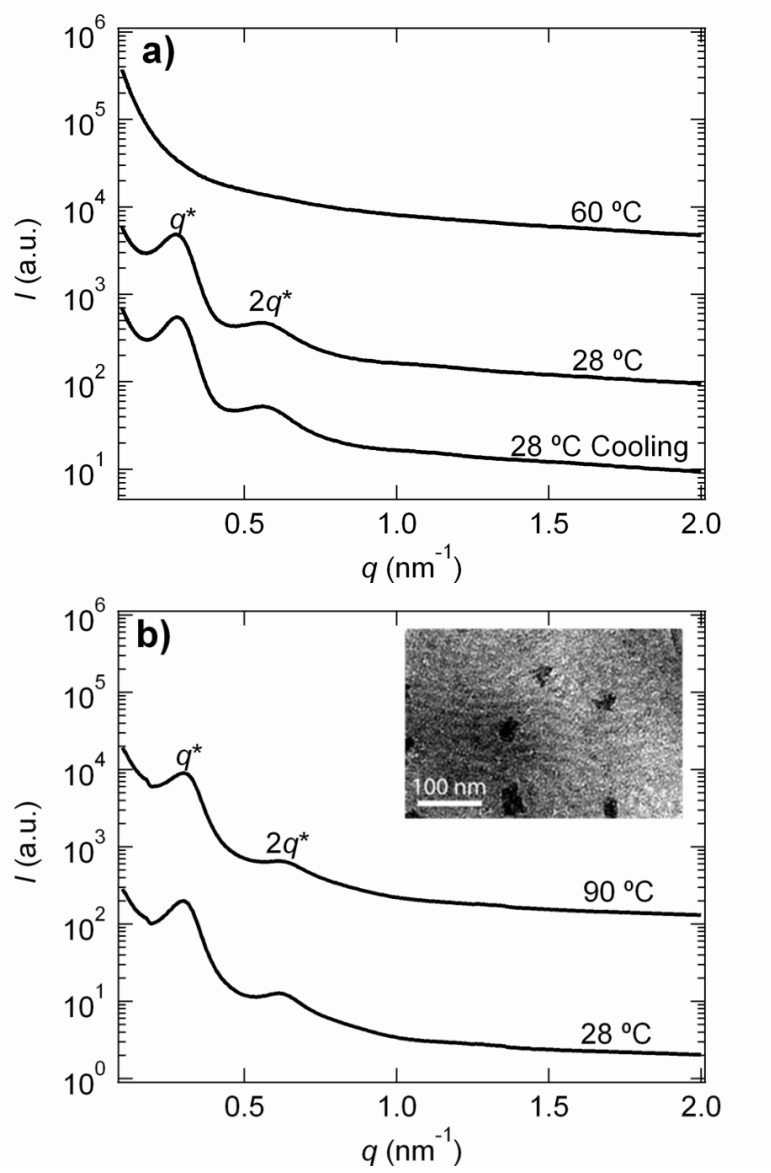

Figure 3.2. **(a)** SAXS of P3HT-PEO(5-4) at r_0 = 0. A lamellar microstructure is seen at 28 °C while the featureless profile is obtained at 60 °C. The lamellar microstructure returns after cooling to 28 °C. **(b)** SAXS of P3HT-PEO(5-4) at r_0 = 0.085 indicating a lamellar microstructure. The inset shows the bright field transmission

electron microscopy (TEM) image of a P3HT-PEO(5-4) r_0 = 0.085. Contrast in the image arises from density differences between the P3HT-rich (dark) and PEO-rich (light) microphases.

Figure 3.3 compares the wide angle X-ray scattering (WAXS) profiles of the P3HT-PEO copolymers with those of a P3HT homopolymer at 90 °C which is above the melting temperature of PEO. The WAXS profiles thus reflect the local structure of the P3HT crystals. All of the profiles are dominated by the (100) and (010) reflections of the P3HT chains that are due to the side-chain spacing and π-π stacking, respectively. Weaker peaks and shoulders corresponding to the (200) and (300) reflection are also seen in all of the samples. Qualitatively similar behavior is seen when salt is added to the P3HT-PEO block copolymers. The WAXS data suggest that the introduction of the PEO block and the addition of LiTFSI salt do not have a significant effect on the local arrangement of the P3HT segments. Interestingly there is no difference in the WAXS data from samples that contained nanofibrils [*e.g.* P3HT-PEO(6-2)] and those that did not [P3HT-PEO(5-4)].

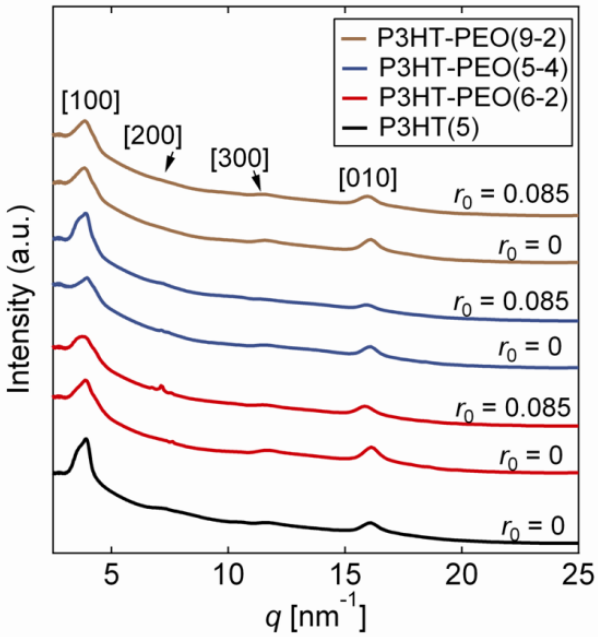

Figure 3.3. WAXS at 90 °C for P3HT(5) at r_0 = 0 (no LiTFSI) and P3HT-PEO at r_0 = 0 and r_0 = 0.085. The (100), (200), and (300) peaks corresponds to the side-chain packing while the (010) peak corresponds to the π-π stacking. No diffraction peak is seen for PEO as the samples are above the PEO melting point.

In summary, SAXS experiments, used to determine morphology, indicate the presence of a lamellar phase in neat P3HT-PEO(5-4) at room temperature and a disordered phase at temperatures above 60 °C. In contrast, SAXS profiles of that neat P3HT-PEO(6-2) and P3HT-PEO(9-2) are featureless indicating that the morphology is dominated by P3HT nanofibrils. After the addition of LiTFSI at r_0 = 0.085, the SAXS profiles from all three samples contain signatures of microphase separation. At this concentration, SAXS profiles from P3HT-PEO(5-4)/LiTFSI mixtures contain clear signatures of a lamellar morphology at temperatures up to 90 °C, while SAXS profiles from P3HT-PEO(6-2)/LiTFSI and P3HT-

PEO(9-2)/LiTFSI mixtures contain broad shoulders that cannot be interpreted in terms of specific morphologies.

3.3.2 *P3EHT-b-PEO Morphology - Breakout and Confined Crystallization*

P3EHT-*b*-PEO was synthesized following the procedure in Chapter 2. One P3EHT-*b*-PEO copolymer was characterized in this section. The P3EHT block has a molecular weight of 5 kg/mol and the PEO block has a molecular weight of 2 kg/mol. In Figure 3.4, we show two DSC scans cooled to -40 °C and 25 °C to observe the temperatures limits for PEO crystallization in the P3EHT-*b*-PEO copolymer. When cooling the DSC sample to -40 °C, we observe an exothermic peak at -6 °C corresponding to the crystallization peak for PEO. During the heating scan, we observe a melting peak at 38 °C corresponding to PEO and melting peaks at 64 °C and 77 °C corresponding to P3EHT. However, when only cooling to 25 °C (near the lowest temperature limit of our x-ray scattering and TEM experiments), we do not observe a crystallization peak for PEO and we do not observe a PEO melting peak at 38 °C during the heating scan. We note the drop in heat flow at 30 °C corresponds to the isothermal wait step of 1.5 hours needed for P3EHT crystallization. Results of both DSC runs show that P3EHT-*b*-PEO needs to be cooled to temperatures well below 25 °C to crystallize PEO. Figure 3.4c shows the wide angle x-ray scattering (WAXS) for neat P3EHT-*b*-PEO, which was held at 28 °C for 90 minutes. The resulting scattering peaks are consistent with previously published WAXS data on P3EHT, where the sharp peak at 0.44 nm^{-1} corresponds to the (100) plane (side-chain packing). The scattering peaks for crystalline PEO are not observed, confirming that the P3EHT block is the only crystallized component.

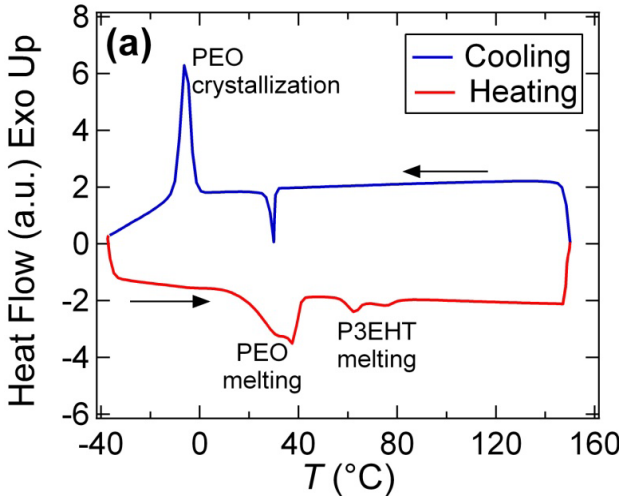

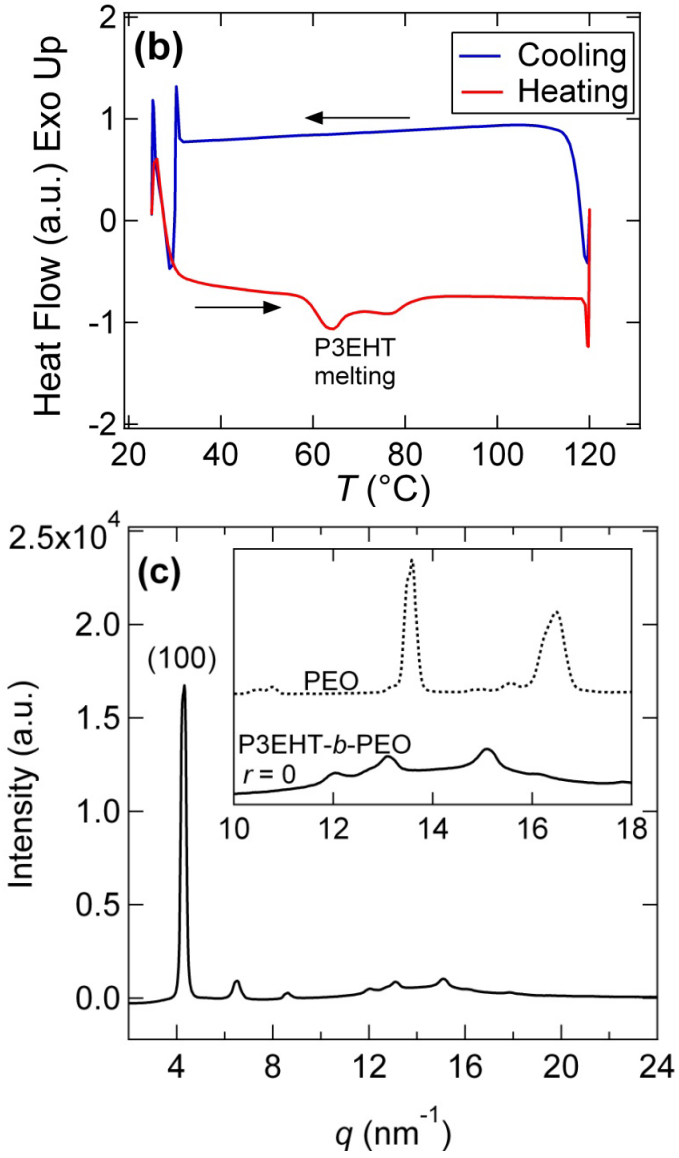

Figure 3.4. DSC cooling/heating scans of P3EHT-*b*-PEO (r =0) at 10 °C/min between **(a)** -40 °C and 150 °C and **(b)** 25 °C and 120 °C. The heating scan is the red curve and cooling scan is the blue curve. Crystallization and melting peak for PEO is observed when cooling to –40 °C, while no such peaks are observed when cooling to 25 °C. Melting peaks at 64 °C and 77 °C corresponding to P3EHT is observed in both cases. The drop in heat flow at 30 °C corresponds to an isothermal wait step. **(c)** WAXS curve of P3EHT-*b*-PEO (r =0) where the inset compares WAXS curves of PEO homopolymer (dotted curve) and P3EHT-*b*-PEO (r = 0) (solid curve).

The introduction of the LiTFSI salt at a concentration of r = 0.125 leads to much weaker melting peaks in the DSC data (Figure 3.5a) at 65 °C and 81 °C. Increasing the isothermal crystallization time from 3 to 8 hours results in an increase in intensity of the melting peaks and a small decrease in the melting temperatures to 62 °C and 76 °C. The longer crystallization time required for the salt-containing sample was further confirmed through WAXS, where the scattering peaks could only be seen after annealing at 28 °C for 12 hours (Figure 3.5b). Both the DSC and WAXS data suggest that the crystallization

kinetics of the P3EHT block is affected by the addition of salt. Previous studies on P3HT containing block copolymers indicate some LiTFSI partitions into the P3HT domain.[123] Therefore, it is possible some LiTFSI is partitioning into the P3EHT domain for the $r = 0.125$ sample, which could explain different crystallization properties, particularly the slightly lower melting temperature.

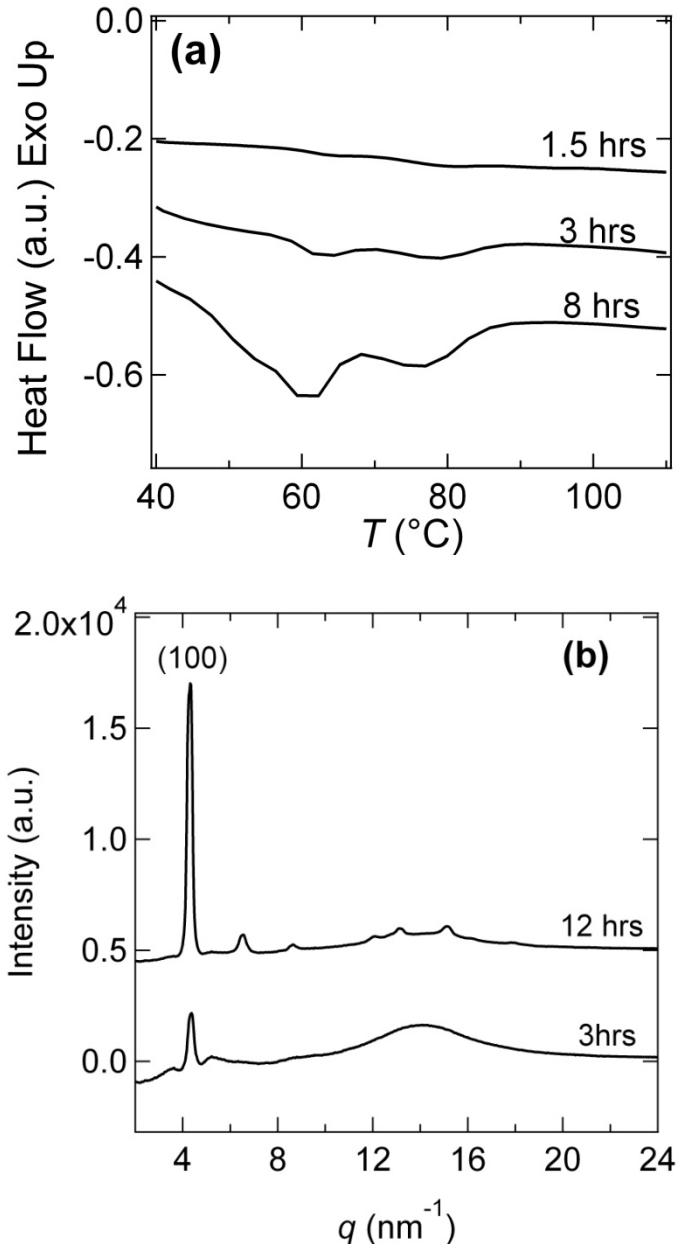

Figure 3.5. **(a)** DSC heating scans of P3EHT-*b*-PEO ($r = 0.125$) at 10 °C/min after an isothermal wait step of 1.5, 3, and 8 hours at 30 °C; **(b)** WAXS curves of P3EHT-*b*-PEO ($r = 0.125$) after going above the melting temperature, cooling to 30 °C and waiting for 3 and 12 hours. The P3EHT block for both $r = 0$ and and $r = 0.125$ remain semicrystalline as indicated by the melting peaks in the DSC scans and the (100) reflection in the WAXS profiles. The P3EHT block for the $r = 0$ sample crystallized in 1.5 hours, while the $r = 0.125$ showed a

very weak melting peak in 1.5 hours. However, a more pronounced P3EHT melting peak was observed after 8 hours.

Figure 3.6a shows the small angle X-ray scattering (SAXS) intensity, I, vs. the magnitude of the scattering vector, q, of P3EHT-*b*-PEO for $r = 0$. At 28 °C and 50 °C, the scattering profiles indicate two broad shoulders that index to q^* and $2q^*$, where q^* is the magnitude of the scattering vector associated with (100) family of reflection planes of a given morphology. The characteristic domain spacing, $d = 2\pi/q_{max}$, is 15.9 nm, where q_{max} is the magnitude of q at the most intense peak (or the peak that occurs at the lowest value of q). The TEM image (Figure 3.6c) of the neat sample indicates a lamellar morphology with a domain spacing of 15.5 nm. Surprisingly, well-defined lamellae are observed in the TEM image, which is in contrast with the broad peaks seen in the SAXS data. At temperatures above the melting point of P3EHT (90 °C and 120 °C), the SAXS scattering profiles show two distinct Bragg peaks at $\sqrt{6}q^*$ and $\sqrt{8}q^*$, consistent with the gyroid morphology. The characteristic domain spacing, d, is 12.3 nm. Further increase of the temperature to 125 °C leads to a disordered structure at a q_{max} of 0.51 nm^{-1}. In the inset of Figure 3.6a, a plot of the full width at half max of q_{max} (FWHM) vs. temperature shows a clear jump in FWHW, which is typical for an order-to-disorder phase transition (ODT). The ODT is reversible, as evidenced by the return of the gyroid morphology after the sample was cooled back down to 90 °C (Figure 3.6b). This is the first evidence of the existence of an ODT for a P3EHT-containing block copolymer.

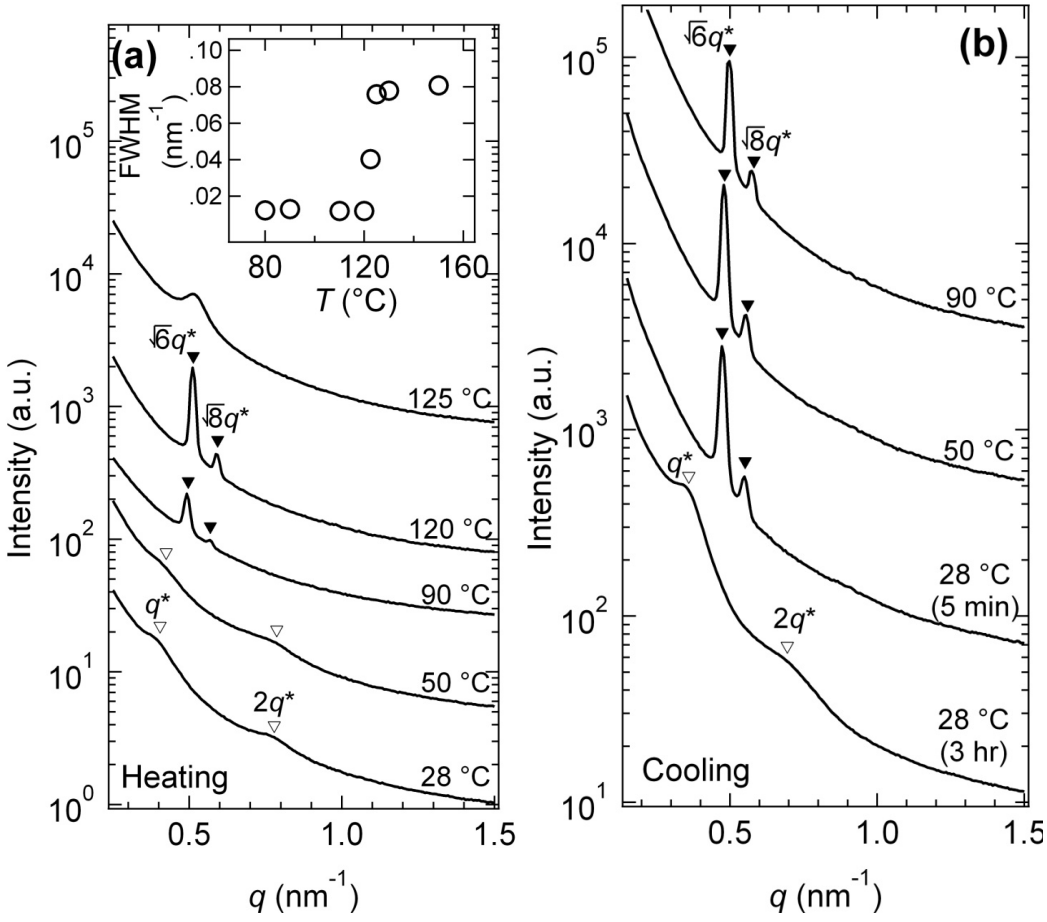

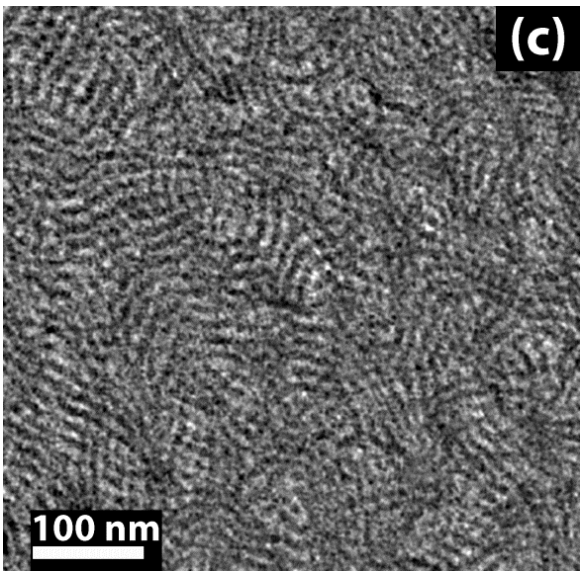

Figure 3.6. **(a)** The heating scan and **(b)** cooling scan SAXS curves of P3EHT-*b*-PEO ($r = 0$). The inset in **(a)** is the full width half max (FWHM) of the primary scattering peak vs. T (temperature) curve indicating an order-to-disorder phase (ODT) transition. The melt-state gyroid morphology (90 °C) is destroyed ("breakout") upon crystallization of the P3EHT block at 28 °C. The filled triangles denote peaks corresponding to the gyroid morphology and the unfilled triangles denote peaks corresponding to the lamellar morphology. **(c)** Bright field transmission electron microscopy (TEM) image of P3EHT-*b*-PEO ($r = 0$) shows that the "breakout" morphology is lamellar at room temperature. Contrast arises from the higher electron density in the semicrystalline P3EHT (dark phase).

In Figure 3.6b, we show the SAXS data for $r = 0$ during the cooling run after heating the P3EHT-*b*-PEO to 150 °C. Unlike the heating step to 50 °C where lamellar morphology was observed (Figure 3.6a), the cooling step to 50 °C shows retention of the gyroid morphology (Figure 3.6b). DSC data and WAXS experiments during cooling runs indicate that P3EHT does not recrystallize at 50 °C (data not shown). It is not clear if this observed suppression of crystallization at 50 °C is due to kinetic factors. Further cooling to 28 °C shows the gyroid morphology at early times and a lamellar morphology at long times (Figure 3.6b). This observation indicates that the crystallization of P3EHT block destroys the melt-state morphology. In other words, the P3EHT crystals "breakout" of the confined domains dictated by thermodynamic segregation of the blocks (χN and ϕ_{EHT}). This is due to the non-glassy nature of the PEO block and the fact that χN is between 14 and 20, i.e., the system is weakly segregated. The fact that the breakout structure is lamellar is not completely unexpected as previous theories[114, 115] and experiments[72-74, 124] on weakly segregated semicrystalline block copolymers show the crystalline-state morphology is often lamellar regardless of the melt-state morphology.

Segregation between the blocks can be increased by the addition of LiTFSI salt to P3EHT-*b*-PEO. In Figure 3.7a, the SAXS profile of the P3EHT-*b*-PEO/LiTFSI mixture with $r = 0.125$ in the melt state (150 °C) shows the presence of the lamellar morphology indicated by the Bragg peaks at q^*, $2q^*$, $3q^*$, and $4q^*$ corresponding to a d of 15.4 nm. The sample

was quenched to 28 °C to allow for the crystallization of P3EHT block. We see that the lamellar morphology is retained even after 12 hours. However, the Bragg peaks broaden slightly and the lamellar spacing increases; *d* increases from 15.4 nm to 18.3 nm during the 12 hour annealing step. The DSC and WAXS data shown in Figure 3.5 indicate that the P3EHT block in the P3EHT-*b*-PEO/LiTFSI mixture with $r = 0.125$ crystallizes on this time scale. We thus attribute the broadening the Bragg peaks to P3EHT crystallization. A lamellar morphology is also observed in the TEM image of the P3EHT-*b*-PEO/LiTFSI mixture with $r = 0.125$ shown in Figure 3.7b, where the characteristic domain spacing is 17.5 nm. It is evident that the P3EHT-*b*-PEO/LiTFSI mixture with $r = 0.125$ exhibits confined crystallization at room temperature. This is attributed to an increase in segregation, χN, and the fact the melt-state morphology is lamellar. Extrapolation of the data for polystyrene-*b*-poly(ethylene oxide)(PS-*b*-PEO)/LiTFSI mixtures[125] shows that χ increases by a factor of about 7 when *r* is increased from 0 to 0.125. The DSC data in Figure 3.5 indicate that the P3EHT crystals melt in both $r = 0$ and $r = 0.125$ samples around 80 °C. In spite of this, the $r = 0$ sample crystallizes in 90 minutes while there is virtually no evidence of crystallization in the $r = 0.125$ sample after 90 minutes of annealing. The difference in crystallization kinetics can be attributed to confinement. The $r = 0$ sample exhibits breakout crystallization, while $r = 0.125$ sample exhibits confined crystallization. Previous studies on semicrystalline block copolymers have shown that breakout crystallization follows sigmoidal kinetics, while confined crystallization follows first-order kinetics.[77, 126, 127] In particular, the crystallization half-time is more highly dependent on crystallization temperature during confined crystallization. As a result, varying the temperature for isothermal crystallization of the $r = 0.125$ sample could greatly affect the time needed to fully crystallize the P3EHT block. The magnitude in time difference for crystallization (hours) between $r = 0$ and $r = 0.125$ is far greater than previously reported confined/breakout crystallization behavior in block copolymers. This could be attributed to the inherent slower crystallization kinetics of P3EHT. Further work is needed to fully understand the crystallization kinetics in P3EHT-*b*-PEO during confinement and breakout.

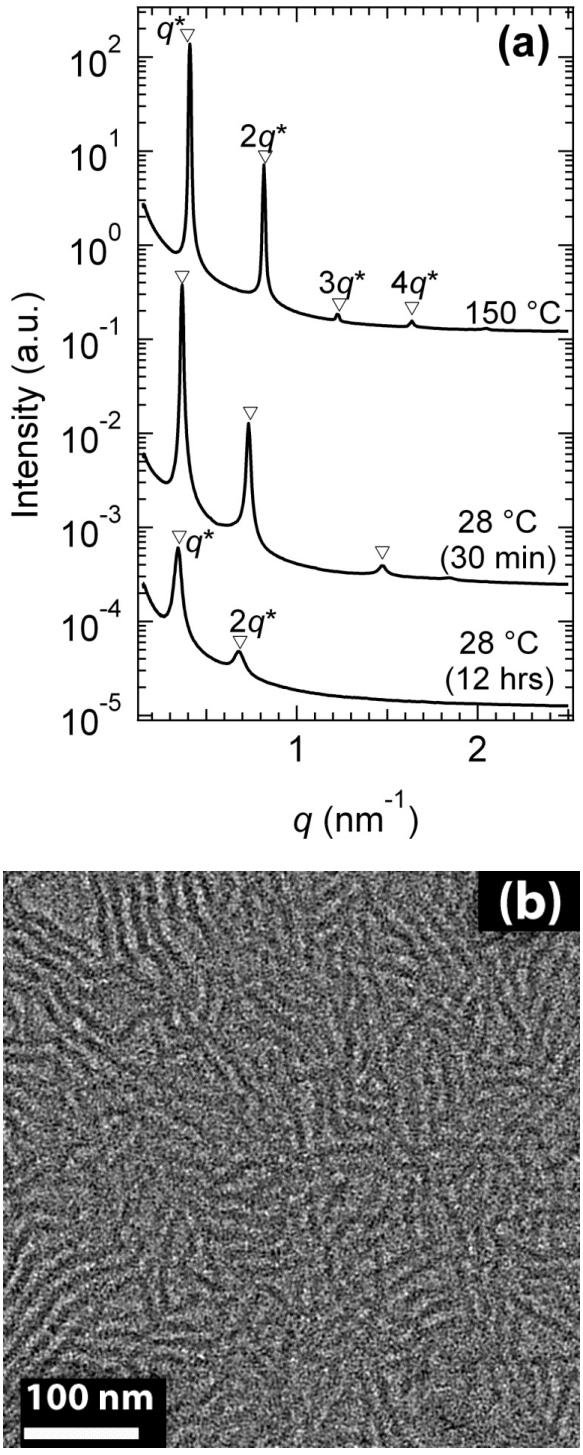

Figure 3.7. **(a)** The cooling run SAXS curves of P3EHT-*b*-PEO (r = 0.125). The lamellar morphology is retained after 12 hours at 28 °C where P3EHT block fully crystallizes (confined crystallization). (c) Bright field TEM image of P3EHT-*b*-PEO (r = 0.125) at room temperature indicating a lamellar morphology. Contrast arises from the higher electron density in the semicrystalline P3EHT (dark phase).

In summary, a P3EHT-*b*-PEO copolymer was synthesized by producing ethynyl-terminated P3EHT in one step using GRIM polymerization followed by coupling to an azide-terminated PEO block through click chemistry. This facile approach may be used for synthesizing a variety of poly(3-alkylthiophene)-containing block copolymers. We have demonstrated that the morphology of this copolymer can be controlled by thermodynamic parameters such as temperature and segregation strength (χN). The segregation strength was adjusted by the addition of LiTFSI salt. In the melt state, the salt-free sample (r =0) exhibits a gyroid morphology while the salt-containing sample (r = 0.125) exhibits a lamellar morphology. Quenching the salt-free sample to room temperature results in a lamellar morphology due to the breakout of the P3EHT crystals. In contrast, there is little change in the morphology of the salt-containing sample upon quenching to room temperature, *i.e.* we observed confined crystallization. This qualitative change is attributed to increase in χN from about 17 to 100. Finally, this work provides the first estimate for the value of χ between P3AT chains and conventional polymers such as PEO.

3.3.3 *Determination of χ_{eff} of P3EHT-b-PEO using the random phase approximation*

The ODT for P3EHT-*b*-PEO at r = 0 (Figure 3.6a) can be used to estimate the value of χ between P3EHT and PEO. There are currently no literature reports of statistical segment length of P3EHT chains in the melt state, l_{EHT}. We apply the random phase approximation to the SAXS data in the disordered state to obtain l_{EHT} as outlined by Lin et al.[120] In the mean field theory the value of q_{max} depends on statistical segment lengths only and not on χ. Thus, knowing the literature value for the statistical segment length of PEO chains, l_{EO}, 0.72 nm,[121] and the value of q_{max} in the disordered state, 0.51 nm^{-1}, we obtain l_{EHT} = 1.1 nm. The statistical segment lengths and χ parameters in this work are based on reference volume of 0.1 nm^3. Thus, the conformational asymmetry factor for our system is l_{EHT}/l_{EO} = 1.5. The mean-field phase diagram for block copolymer with l_{EHT}/l_{EO} = 1.5 and ϕ_{EHT} = 0.71 contains a transition from gyroid to cylinder at χN = 20, a transition to cylinders to spheres at χN = 14.5, and a transition from spheres to disordered at χN = 14.[62] However, only a gyroid to disorder transition was observed in our P3EHT-*b*-PEO (r = 0) at 125 °C. We thus conclude the value of χN for our system at 130 ± 5 °C is between 14 and 20. Since N = 108 we conclude that 0.13 < χ < 0.19 at 130 ± 5 °C. To our knowledge, this is the first quantitative measurement of χ between conventional polymers such as PEO and poly(3-alkylthiophene) chains. This is the first step toward prediction of the morphology of block copolymers containing poly(3-alkylthiophene) chains.

The above method for determining χ only applies to conventional block copolymers with Gaussian chains. P3EHT is, however, a semiflexible polymer.[109, 128] Theoretical work on the phase behavior of semiflexible block copolymers shows that the value of χN at the ODT for these systems depends on magnitude of the Maier-Saupé parameter, μ, relative to χ.[65, 66, 68, 69] The Maier-Saupé parameter quantifies interactions between rod-like molecules in the mean-field limit. The μ value for P3EHT is 0.01 at 130 ± 5 °C[128], thus μ/χ is estimated to be between 0.052 and 0.076 for our system. The predictions in ref. 68 indicate that such a small value of μ/χ has a negligible effect on the value of χN at the ODT. We note

in passing that our estimate is based entirely on the mean-field theory of block copolymers. *i.e.*, fluctuation corrections[64] are ignored.

Alternatively, with absolute SAXS scattering data, we can determine the value of χ through fitting the RPA equation (with both χ and l_{EHT} as adjustable parameters). The two-dimensional scattering patterns were azimuthally averaged and corrected for scattering from air and the kapton windows. Then, the scattering data were converted to absolute intensities (I_{abs}) using a glassy carbon standard obtained from Jan Ilavsky at Argonne National Laboratory. In Figure 3.8, we show the absolute SAXS profile of P3EHT-*b*-PEO at $r = 0$ at $T_{ODT} = 130 \pm 5$ °C. The solid red curve is the RAP fit (using equation 3.1) to the scattering profile. Following the procedure established by Leibler and Lin et al., the heights of the experimental and theoretical peaks were matched by adjusting χ while the location of the peak in q-space was obtained by adjusting the statistical segment length (i.e. radius gyration of the polymer). It is important to note we included an exponential term to help fit the scattering from the background. The χ value obtained from the RPA fit is 0.138 ($\chi N = 15.9$). This is very close to the lower limit of range of χ determined using the mean-field phase diagram. This is the first application of the random phase approximation to a poly(3-alkylthiophene)-containing block copolymer system.

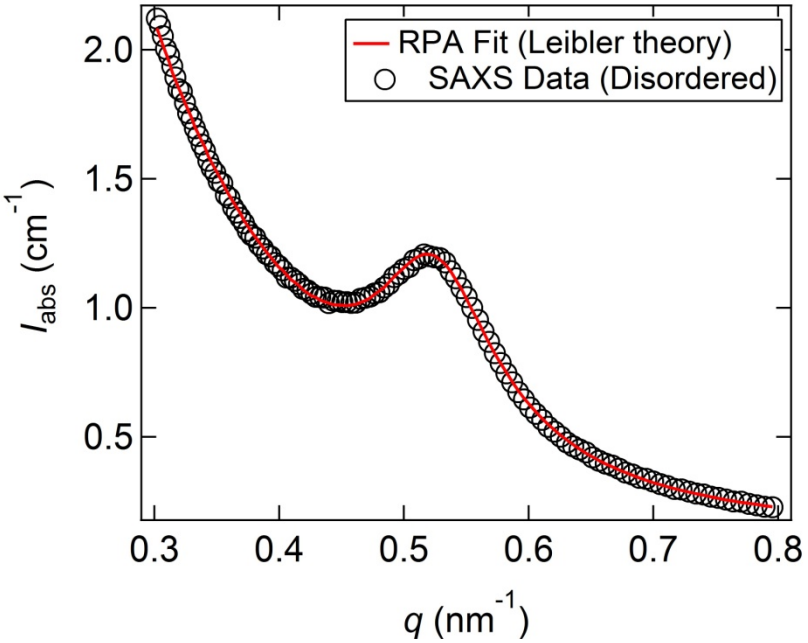

Figure 3.8 RPA fit of absolute SAXS data of P3HT-b-PEO at r = 0 taken at 130 ± 5 °C. The χ value obtained from the RPA fit is 0.138 (χN = 15.9). This is the first evidence of the application of the random phase approximation to a poly(3-alkylthiophene)-containing block copolymer system.

In Figure 3.9, we show the T_{ODT} values for P3EHT-*b*-PEO at $r = 0$, 0.0025, 0.005. 0.01, and 0.02. The T_{ODT} increases from 130 ± 5 °C at $r = 0$ to 170 °C at $r = 0.02$. Order to disorder transitions were not accessible for salt concentrations above 0.20 because the ODT is above the PEO degradation temperature.

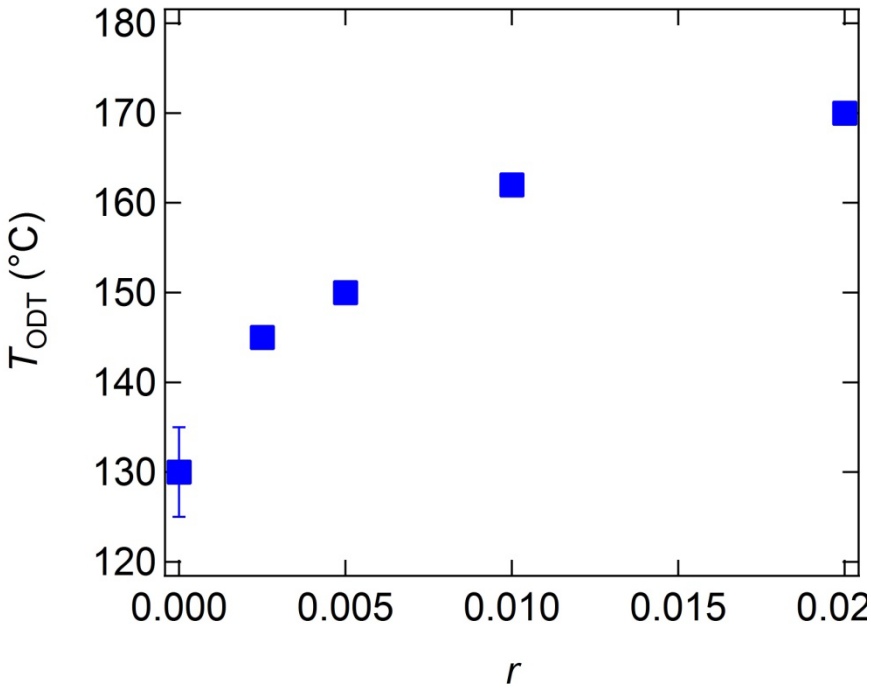

Figure 3.9 T_{ODT} for a P3EHT-b-PEO salt series determined from SAXS measurements.

Previous theoretical and experimental research has shown that the effect of added salt results in an increase of the "effective" Flory-Huggins interaction parameter, χ_{eff}.[122, 125, 129, 130] The assumption is that salt is located only in one of the phases. Therefore, concomitant changes in ϕ need to be taken into account. A linear relationship between χ_{eff} and r has been proposed:

$$\chi_{eff} = \chi_{r=0} + mr, \tag{3.4}$$

where $\chi_{r=0}$ is the neat Flory-Huggins interaction parameter, and m is a system-dependent constant related to the anion of the salt. The effect of salt addition on a block copolymer is quantified by the magnitude of m. For PS-*b*-PEO/LiTFSI mixtures, where the LiTFSI resides all in the PEO domain, an m value of 1.56[125] was experimentally determined by applying the Leibler's mean-field theory. It is clear the χ_{eff} increases as a function of salt concentrations.

To determine χ_{eff} for P3EHT-*b*-PEO/LiTFSI mixtures, we fit the RPA equation at the ODT for r = 0.0025, 0.005. 0.01, and 0.02. The calculations were done at 170 °C. We assume that LiTFSI preferentially resides in the PEO phase. The SAXS disorder peak was fit to equation 3.1 by adjusting l_{EHT}, χ, and scattering contrast, $\left(b_A/v_A - b_B/v_B\right)^2$. The scattering contrast is adjusted to take into account the challenge in accurately calculating the scattering length density after the addition of LiTFSI. In Figure 3.10, we show the χ_{eff} values as a function of r when we assume all the salt is in the PEO phase. Surprisingly, χ_{eff} decreases with r, which is in stark contrast with previously reported trends of χ_{eff} where it increases with r. In this situation, m is -0.31. It is important to note that the change in χ_{eff} is very small (χ_{eff} decreases from 0.133 at r = 0 to 0.127 at r = 0.02). On the other hand, we consider the case where we assume that all the LiTFSI resides in the P3EHT phase (taking

into account the change in ϕ_{EHT}). As shown in Figure 3.10, χ_{eff} increases with r, where m is 0.175 (χ_{eff} increases from 0.133 at r = 0 to 0.137 at r = 0.02). It is clear we are observing very small changes in χ_{eff}. The fact that χ_{eff} increases with r suggests LiTFSI might be partitioning into the P3EHT phase. Our previous study on P3HT containing block copolymers indicate some LiTFSI partitions into the P3HT domain (discussed in Chapter 4).[123] Moreover, we postulate that the TFSI anion, in fact, partitions into the P3EHT phase while Li^+ remains solvated in the PEO domain. This will follow trend in χ_{eff} where we assume all the salt goes into the P3EHT phase as most of the volume change occurs due to the large $TFSI^-$ anion.

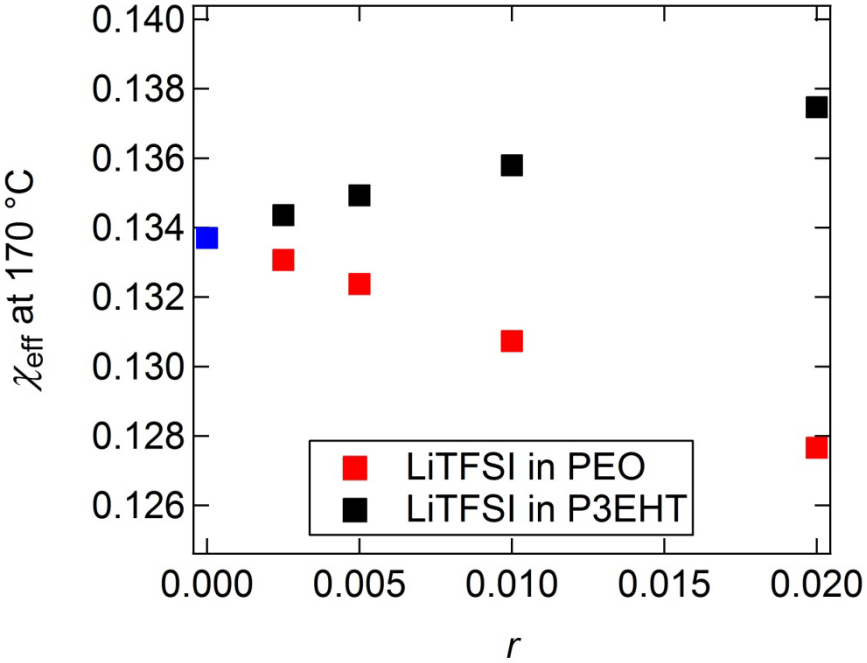

Figure 3.10 χ_{eff} for a P3EHT-b-PEO salt series determined from SAXS measurements assuming that the LiTFSI is all in PEO phase and assuming that the LiTFSI is all in the P3EHT phase.

In summary, we determine the χ parameter for a P3EHT-*b*-PEO copolymer by applying the random phase approximation to scattering data. This is the first attempt to apply RPA theory to a P3AT-containing block copolymer. First, we use a mean-field phase diagram to determine the χ parameter for a neat P3EHT-*b*-PEO sample, which we conclude is between 0.13 and 0.19 at 130 ± 5 °C. We extend our analysis using absolute SAXS data where we fit the RPA equation to determine χ. For neat P3EHT-b-PEO, we obtain a $\chi_{r=0}$ value of 0.138. The order to disorder transition temperature (T_{ODT}) increases with the addition of LiTFSI salt. The effective Flory-Huggins interaction parameter (χ_{eff}) was determined by fitting the RPA equation to the disorder scattering profile for each salt sample at 170 °C. When assuming the LiTFSI is all in the PEO phase, χ_{eff} decreases with salt concentration. This is in stark contrast in previously reported salt-containing block copolymers where χ_{eff} increases with salt concentration. However, when assuming all the salt is in the P3EHT phase, χ_{eff} increases with salt concentration. The trends in the χ_{eff} with r suggest that the $TFSI^-$ anion, in fact, partitions into the P3EHT phase while Li^+ remains solvated in the PEO domain.

Chapter 4 - Simultaneous Conduction of Electronic Charge and Lithium Ions in Block Copolymers[‡]

ABSTRACT

The main objective of this work is to study charge transport in mixtures of poly(3-hexylthiophene)-*b*-poly(ethylene oxide) (P3HT-PEO) block copolymers and lithium bis(trifluromethanesulfonyl) imide salt (LiTFSI). The P3HT-rich microphase conducts electronic charge while the PEO-rich microphase conducts ionic charge. A combination of ac and dc impedance measurements was used to determine the electronic and ionic conductivity of our samples. The ionic conductivities of P3HT-PEO/LiTFSI mixtures are lower than those of mixtures of PEO homopolymer and LiTFSI, in agreement with published data obtained from other block copolymer/salt mixtures. In contrast, the electronic conductivities of the asymmetric P3HT-PEO copolymers are significantly higher than those of the P3HT homopolymer. This is unexpected because of the presence of the non-electronically-conducting PEO microphase. This implies that the intrinsic electronic conductivity of P3HT the microphase in P3HT-PEO copolymers is significantly higher than that of P3HT homopolymer.

4.1 Introduction

Simultaneous electronic and ionic conduction has been studied extensively in various inorganic materials.[131-136] In particular, Reiss has outlined methods for measuring electronic and ionic conduction for inorganic mixed conductors.[135, 136] A method using ac impedance spectroscopy was developed to determine the presence of independent pathways for charge transport and resistance in an inorganic material between ion blocking electrodes.[137] In addition, some work has been done to model the impedance spectroscopy of mixed conductors, which included a term for accounting for imperfections in the electrodes.[138] There also have been a few reports of simultaneous electronic and ionic conduction in various polymeric systems.[139-144] In refs. 141 and 142, attempts were made to quantify the electronic and ionic conduction, but did not shed light on the relative rates when both ionic and electronic charge species are present. Ren et al. measured the electronic and ionic conductivity of poly(3-methylpyrrole-4-carboxylic acid) using dc and ac impedance measurements.[141] Plocharski studied the electronic and ionic conduction of doped poly(*p*-phenylene) homopolymer, but the source of ionic charges was not established.[143]

[‡] Parts of this chapter have been reported in *ACS Nano*. **2012**, *6* (2), 1589-1600

The purpose of this paper is to study the relationship between morphology and charge transport in mixtures of P3HT-PEO block copolymers and lithium bis(trifluromethanesulfonyl) imide (LiTFSI). The P3HT block enables electronic transport while the PEO block enables ion transport. Our results indicate that LiTFSI partitions into both P3HT and PEO microphases. The effect of this on charge transport is quantified. The morphology this system is described in the Chapter 3.

Our group has studied the relationship between charge transport and morphology in lamellar block copolymers with an ion-conducting block and an insulating block.[85, 86, 122, 145] These studies have shown that conductivity, σ, is proportional to the volume fraction of the conducting block, ϕ. We thus obtain:

$$\sigma = f\phi\sigma_0, \tag{4.1}$$

where σ_0 is the intrinsic conductivity of the conducting phase and f is a factor that accounts for the morphology (also called tortuosity factor in the literature, although this term is usually used in the context of a porous materials with ill-defined pores). For randomly oriented grains comprising alternating conducting and non-conducting lamellae, f = 2/3. The maximum value of f is obviously unity. This limit is appropriate when transport limitations at grain boundaries is not significant.[85] Equation 4.1 can readily be applied to systems wherein more than one kind of charge is transported. A major objective of the present study is to test the applicability of such a framework to P3HT-PEO/LiTFSI blends. To our knowledge, this is the first attempt to quantify the relationship between morphology and simultaneous transport of electronic and ionic charges.

4.2 Methods

4.2.1 *Conductivity Sample Preparation*

Samples for conductivity measurements were prepared by hot pressing freeze-dried samples into a 125 μm thick Garolite G-10 spacer with an inner-hole diameter of 3.88 mm. For thickness dependent measurements on the P3HT-PEO/LiTFSI mixture, we also used a 250 μm G-10 spacer and a 25 μm Kapton spacer. Nickel foil current collectors were pressed at 1000 psi on both sides of the spacer at 90 ^{o}C for 30 seconds using a Carver press (in a glove box). The Ni-polymer-Ni sandwich was allowed to anneal for an additional 30 minutes at 90 ^{o}C after the pressure was released. The actual thickness of the polymer in the spacer was measured after annealing. Due to overfilling the spacer hole, the actual thickness is slightly larger than the spacer thickness, but is not an issue for taking measurements as the polymer is a hard solid at 90 ^{o}C. The sandwich was sealed in aluminum laminated pouch material (Showa Denko) using a vacuum sealer (Packaging Aids Corp) with nickel tabs in an argon glovebox. Our approach ensures that the samples are air- and water-free.

4.2.2 *Conductivity Measurements*

Impedance spectroscopy measurements were made using either a Bio-Logics VMP3 or a Solartron 1260 instrument with applied ac voltages in the 10 mV-50 mV range, and frequencies ranging from 1MHz to 1 mHz. Resistances were calculated from the complex impedance data ($Z^* = Z' - iZ''$) where Z' and Z'' are the real and imaginary impedances, respectively, using Nyquist plots ($-Z''$ *vs.* Z'). The conductivity, σ, is given by

$$\sigma = \frac{L}{R}, \tag{4.2}$$

where L is the polymer thickness and R is the resistance ($\Omega \cdot cm^2$), obtained from intersections of the Nyquist plots on the Z' axis. Small dc potentials between -50mV to 50mV were imposed on the P3HT-containing samples and the steady-state current response was measured using the Biologic VMP3 instrument. All conductivity measurements were averaged over a minimum of three samples and all error bars were calculated from the standard deviation. Also, all reported conductivity values are from ac impedance measurements unless stated otherwise.

4.2.3 *Equivalent Circuit Curve Fitting*

Experimental ac impedance spectroscopy data were analyzed using equivalent circuits composed of constant phase elements (CPE) and resistors. The impedance of a CPE is given by:

$$Z_Q = \frac{1}{Q(i\omega)^a}, \tag{4.3}$$

where Q is the capacitance (constant phase element), ω is the angular frequency and a is a measure of non-ideality of the capacitor. The unit for Q is $F \cdot s^{a-1}$. Both Q and a are fitting parameters and $a = 1$ corresponds to the ideal capacitor. Physical arguments were used to arrive at a particular equivalent circuit and the Randomize + Simplex algorithm built into the EC-Lab software package was used to fit the impedance data. In all cases, we report the parsimonious result, *i.e.* the simplest equivalent circuit with the fewest elements that can describe the data.

4.3 Results and Discussion

The characteristics of the P3HT homopolymer and the P3HT-PEO block copolymers used in this chapter are summarized in Table 1.

Table 4.1. Characteristics of polymers used in chapter 4.

Polymer Name	$M_{n,P3HT}$[a] (kg/mol)	$M_{n,PEO}$[a] (kg/mol)	RR[b] (%)	ϕ_{HT}[c] (P3HT block)	PDI[d]	Morphology

P3HT(5)	5.0	---	>94	1	1.2	Nanofibrillar
P3HT-PEO(9-2)	9.0	2.0	>98	0.81	1.27	Nanofibrillar
P3HT-PEO(6-2)	6.0	2.0	>95	0.74	1.33	Nanofibrillar
P3HT-PEO(5-4)	5.0	4.2	>95	0.53	1.30	Lamellar

[a]M_n = number-average molecular weight and [b]*RR* = regioregularity, which were determined using ^{1}H-NMR. [c]Calculated using P3HT density[7] of 1.10 g/mL and PEO density[121] of 1.06 g/mL. [d]PDI = polydispersity index as determined through gel permeation chromatography with polystyrene standards.

In Figure 4.1a, we show the results of impedance spectroscopy experiments on P3HT(5) sandwiched between nickel electrodes at 90 ^oC. The impedance data shows one semicircle. The equivalent circuit used to analyze these data is a parallel combination of a resistor and CPE (constant phase element). Extrapolating the semicircle in Figure 4.1a to the real axis gives the electronic resistance of P3HT(5). It is reasonable to assume that the transport in this sample is dominated by electronic charge, and we thus obtain the electronic conductivity of P3HT(5), σ_{HT}, of (4.9±0.6) x 10^{-8} S/cm. This value is within the range of reported conductivity values of undoped regioregular P3HT (10^{-5} to 10^{-8} S/cm).[31-36] Our measured σ_{HT} is at the lower end of the range of the published data. Lui *et al.* found that in-plane conductivity of regioregular P3HT was 10^{-5} S/cm while that in the through-plane geometry was 10^{-8} S/cm.[34] Our measurements were performed using a through-plane geometry. Differences in sample preparation must also be accounted for when comparisons between reported literature values are made. All of our measurements were made on freeze-dried, bulk samples.

In Figure 4.1b we show the Nqyuist plot of PEO homopolymer (M_n = 2 kg/mol) with LiTFSI at r_0= 0.085. As is typically the case with ion-conducting polymers, we see a single semicircle at high frequencies and a capacitive tail at low frequencies. Standard analysis using the equivalent circuit shown in Figure 4.1b results in the conclusion that the ionic conductivity of PEO, σ_{EO}, at r_0 = 0.085 is 2.05 x 10^{-3} S/cm. It should be noted that the semicircle approaches the *Z*' axis at a frequency of about 1 kHz, which is significantly higher than the semicircle touchdown of P3HT(5) (Figure 4.1a) where it is in the mHz range. The capacitive tail appears in Figure 4.1b but not in Figure 4.1a because nickel is a blocking electrode for ions but not for electronic charges. The lack of a capacitive tail is a clear indication of the presence of pathways for the transport of electronic charge. The presence of one semicircle in both Figures 4.1a and 4.1b is a signature of the presence of a single dominant pathway for charge transport in both P3HT and PEO homopolymers.

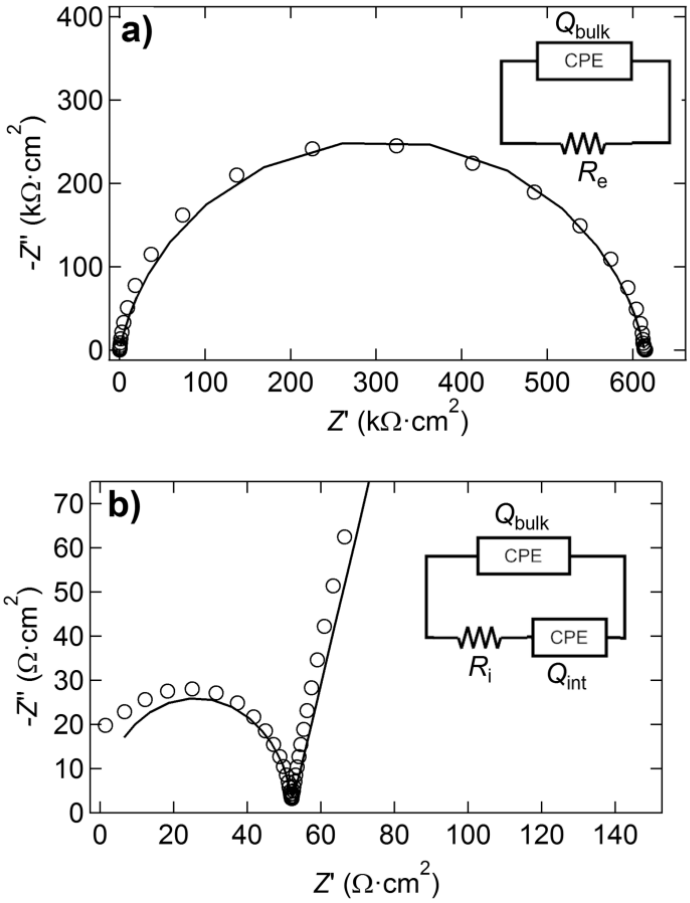

Figure 4.1. **(a)** Nyquist impedance plot (*-Z'' vs. Z'*) for P3HT(5) at 90 °C for frequency range of 1 MHz to 10 mHz. Fit parameters for P3HT(5) are Q_{bulk} = 7.33 x 10^{-11} F·s^{a-1}, a_{bulk} = 0.875, and $R_{e,fit}$ = 610 kΩ·cm^2. **(b)** Nyquist impedance plot (*-Z'' vs. Z'*) for PEO at r_0 = 0.085 at 90 °C for frequency range of 1 MHz to 100 mHz. Fit parameters for PEO are Q_{bulk} = 9.32 x 10^{-10} F·s^{a-1}, a_{bulk} = 1, Q_{int} = 3.14 x 10^{-6} F·s^{a-1}, a_{int} = 0.891, and $R_{i,fit}$ = 52.2 Ω·cm^2. The open circles correspond to the experimental data and the solid curves correspond to the fit using the equivalent circuit shown in the inset.

Figure 4.2a shows impedance spectroscopy data from the P3HT-PEO(6-2)/LiTFSI mixture at r_0 = 0.085 sandwiched between nickel electrodes at 90 °C. The presence of three semicircles in Figure 4.2a, and the absence of such features in Figures 4.1a and 4.1b, suggests the presence of multiple charge transport pathways in the P3HT-PEO(6-2)/LiTFSI mixture. Again, the lack of a capacitive tail indicates the presence of continuous pathways for the transport of electronic charge. The total electronic resistance of the sample was determined from dc polarization experiments. A small dc potential was applied until a steady-state current was observed as shown in Figure 4.2b. The corresponding resistance at steady-state is the total electronic resistance because the nickel electrode blocks ions. In Figure 4.2c, the dc potentials are plotted *versus* steady-state current. The data follows Ohm's law, and the total electronic resistance of the sample, R_{dc}, is 1.30 kΩ·cm^2. This value is very close to the sum of the three semicircles in Figure 4.2a labeled as R_3. Therefore, extrapolation of the low-frequency semicircle to the *Z'* axis gives the total electronic resistance of the P3HT-PEO(6-2)/LiTFSI mixture.

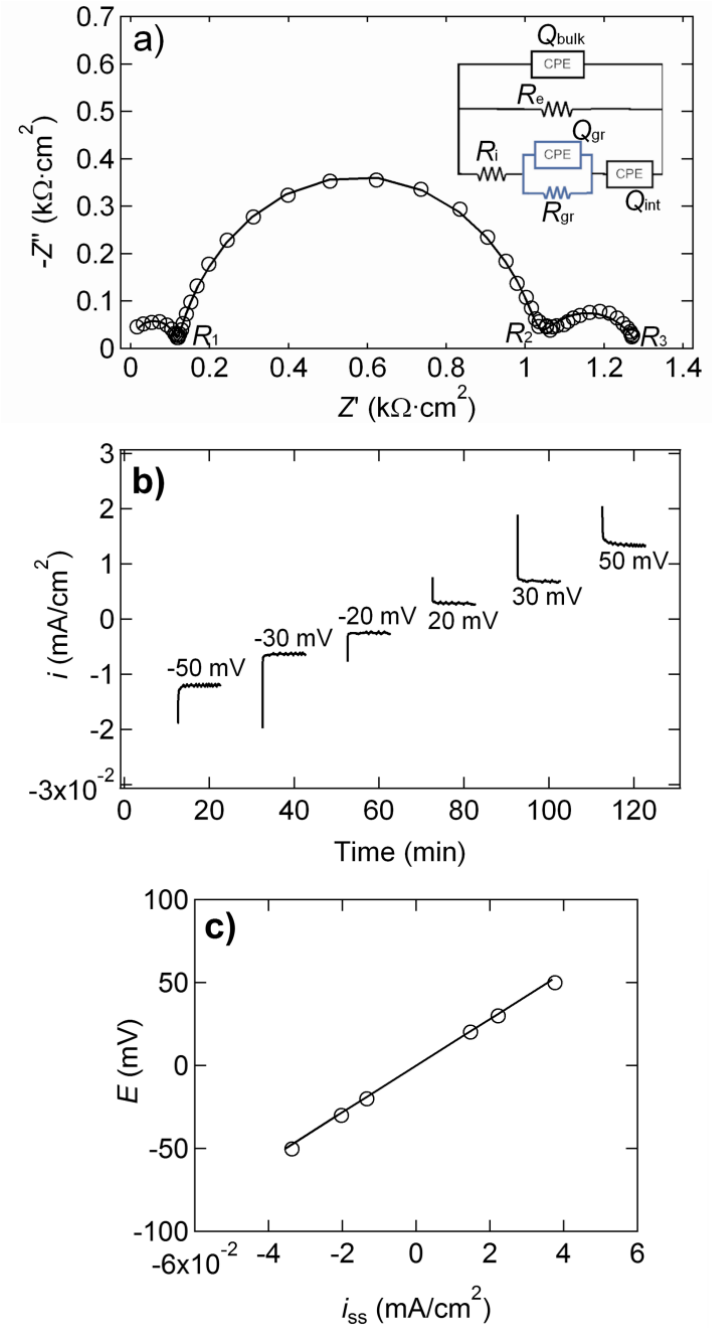

Figure 4.2. **(a)** Nyquist impedance plot (-*Z*'' *vs.* *Z*') for P3HT-PEO(6-2)/LiTFSI (open circles) and the corresponding fit (solid curve) using the proposed equivalent circuit shown in the inset. Fit parameters: Q_{bulk} = 3.79 x 10^{-10} F·s^{a-1}, a_{bulk} = 1, Q_{int} = 2.51 x 10^{-5} F·s^{a-1}, a_{int} = 0.658, Q_{gr} = 2.17 x 10^{-7} F·s^{a-1}, a_{gr} = 0.853, and $R_{i,fit}$ = 0.129 kΩ·cm^2, $R_{e,fit}$ = 1.29 kΩ·cm^2, $R_{gr,fit}$ = 4.90 kΩ·cm^2. **(b)** Current (*i*) *vs.* time curves at different applied dc potentials (*E*). **(c)** Corresponding Ohm's law plot using the measured steady-state current density (i_{ss}). Open circles are the experimental data and solid line is the Ohm's Law fit. The dc resistance, R_{dc}, from Ohm's Law fit is 1.30 kΩ·cm^2.

As a first approximation, one may model the data from salt-containing P3HT-PEO copolymers (*e.g.* Figure 4.2a) by proposing an equivalent circuit that is a linear combination of the equivalent circuits of the two constituent homopolymers. We expect the sample to contain bicontinuous ion- and electron-conducting channels and thus the parallel combination of the two circuits is appropriate. Unfortunately, the equivalent circuit for this combination gives two Nyquist semicircles which is inconsistent with the data in Figure 4.2a. The inset of Figure 4.2a shows the simplest equivalent circuit that is consistent with the data. The equivalent circuit comprises a parallel combination of an electronic and ionic conductor and an additional resistor/constant-phase-element circuit in series with the ionic conductor. This equivalent circuit gives three semicircles, consistent with the data in Figure 4.2a. Three semicircles have been reported before in inorganic mixed conductors, and in that case, the additional circuit has been attributed to the grain boundary resistance to either electronic or ionic transport.[137, 146] Jamnik and Maier proposed that the middle semicircle reflects the fact that the electrodes are not completely reversible to the transfer of electronic charges.[138] The physical underpinning of the added circuit (the circuit in blue in Figure 4.2a inset) is uncertain. We will show that this limitation does not impede our ability to determine the overall electronic and ionic conductivity in our samples. The resistance and capacitance of the blue portion of the equivalent circuit in Figure 4.2a inset are referred to as R_{gr} and Q_{gr}. The equivalent circuit in Figure 4.2a inset indicates that the high frequency semicircle diameter, R_1, is the parallel combination of the R_e and R_i.[137, 138]

$$\frac{1}{R_1} = \frac{1}{R_i} + \frac{1}{R_e}, \tag{4.4}$$

where R_e is the electronic resistance (also equal to R_3). This enables determination of R_i. The middle frequency range semicircle touchdown in Figure 4.2a can be used to calculate R_{gr} with the following equation[137]:

$$\frac{1}{R_2} = \frac{1}{R_i + R_{gr}} + \frac{1}{R_e}, \tag{4.5}$$

where R_2 is the Z' intercept of the second semicircle (not the radius of the semicircle). We do not use R_{gr} in the discussion below and only include this equation for completeness. The solid curve in Figure 4.2a is a fit of the data to the equivalent circuit in the Figure 4.2a inset. Not surprisingly, the two important parameters R_e and R_i obtained from the fit are consistent with those obtained by using equation (4.4).

The analysis described above was used on r_0 = 0.085 P3HT-PEO(6-2)/LiTFSI samples with different thicknesses. In Figure 4.3a and 4.3b we plot R_i and R_e thus obtained as a function of sample thickness, L. Both electronic and ionic resistance show approximately linear trends with thickness. In principle, the linear fits in Figure 4.3 should go through the origin. The y-intercept of the R_i *versus* L plot (-8 $\Omega \cdot cm^2$) is relatively small, while that of the R_e *versus* L plot (250 $\Omega \cdot cm^2$) is not. This may be due to errors intrinsic in extracting two independent resistances from the data, or the presence of a non-negligible interfacial resistance to the transport of electronic charge at the electrode-polymer interface.

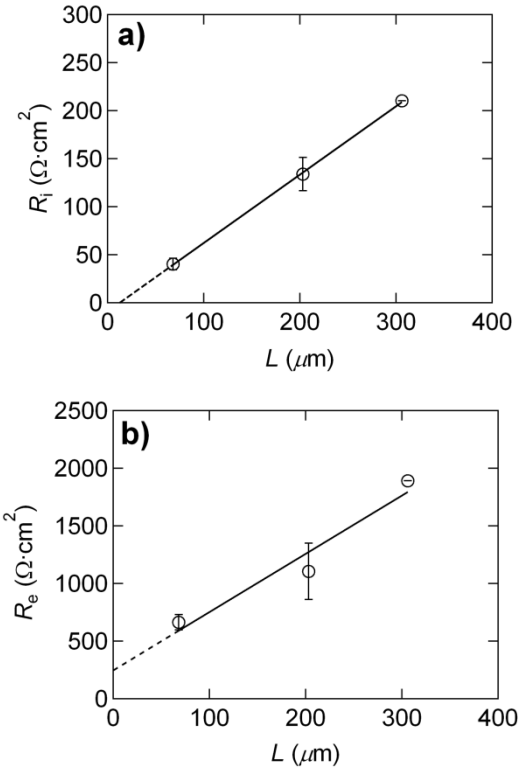

Figure 4.3. **(a)** Ionic resistance, R_i, and **(b)** electronic resistance, R_e, of P3HT-PEO(6-2) at r_0 = 0.085 at 90 ^oC as a function of sample thickness, L. Open circles are the experimental data and solid line is a linear fit. The dash line is the extrapolation of the linear fit to L = 0.

The remainder of this paper is based on data obtained from samples with L=150-200 μm. In Figures 4.4a and 4.4b we show typical impedance data at 90 ^oC obtained from P3HT-PEO(9-2) and P3HT-PEO(5-4) with LiTFSI at r_0 = 0.085, respectively. The data contain three semicircles and thus the method described above can be used to determine electronic and ionic conductivities of the samples. However, the relative magnitudes of the semicircles vary widely due to differences in R_i and R_e. The curves in Figure 4.4 are fits using the equivalent circuit shown in Figure 4.2a, inset which enable determination of R_i and R_e. R_e is much greater than R_i for all three sample, implying that $R_1 \approx R_i$ [see Equation (4.4)].

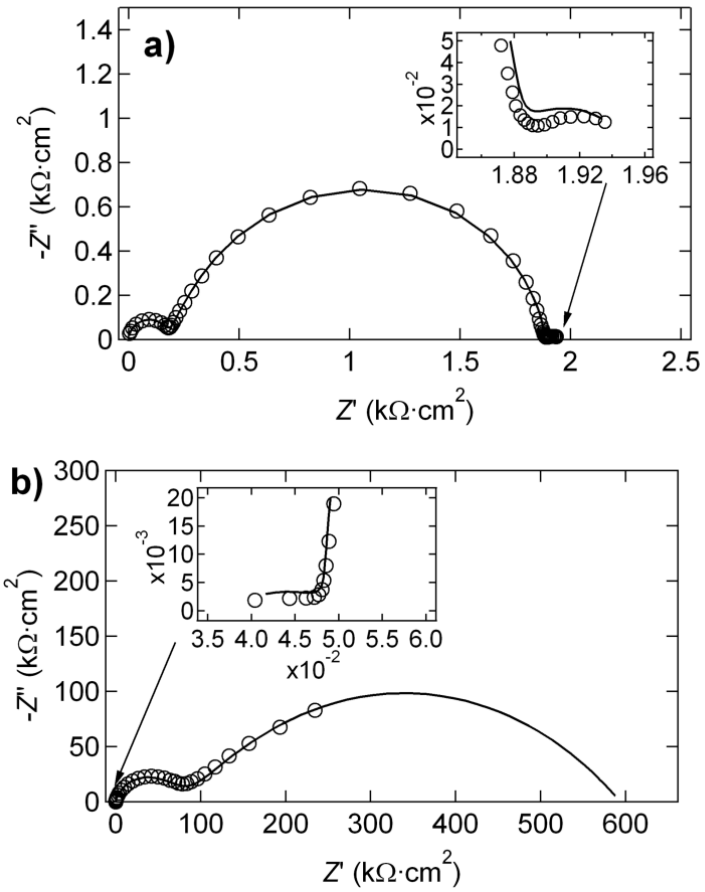

Figure 4.4. **(a)** Nyquist impedance plot (*-Z''* *vs. Z'*) at 90 °C for P3HT-PEO(9-2) at r_0 = 0.085 with frequency range of 1 MHz to 5 mHz. Fit parameters: Q_{bulk} = 1.01 x 10^{-9} F·s^{a-1}, a_{bulk} = 1, Q_{int} = 6.46 x 10^{-6} F·s^{a-1}, a_{int} = 0.572, Q_{grb} = 2.07 x 10^{-7} F·s^{a-1}, a_{gr} = 0.925, and $R_{i,fit}$ = 0.195 kΩ·cm^2, $R_{e,fit}$ = 1.95 kΩ·cm^2, $R_{gr,fit}$ = 47.3 kΩ·cm^2. **(b)** Nyquist impedance plot (*-Z''* *vs. Z'*) at 90 °C for P3HT-PEO(5-4) at r_0 = 0.085 with frequency range of 1 MHz to 1 mHz. Fit parameters: Q_{bulk} = 9.34 x 10^{-8} F·s^{a-1}, a_{bulk} = 0.912, Q_{int} = 2.02 x 10-^{5} F·s^{a-1}, a_{int} = 0.470, Q_{grb} = 5.0 x 10-^{7} F·s^{a-1}, a_{grb} = 0.422, and $R_{i,fit}$ = 0.053 kΩ·cm^2, $R_{e,fit}$ = 594 kΩ·cm^2, $R_{gr,fit}$ = 100 kΩ·cm^2. The open circles represent experimental data while the solid curve represents the equivalent circuit fit.

Electronic and ionic conductivities of P3HT-PEO(9-2) and P3HT-PEO(6-2) at r_0 = 0.085 at selected temperatures were determined by the methods given above and the results are shown in Figure 4.5. Both samples show an increase in σ_e and σ_i as temperature is increased from 40 °C to 90 °C. The temperature dependence on ionic conductivity is fitted to the Vogel-Tamman-Fulcher equation:

$$\sigma_i = A_i \exp\left(\frac{E_i}{R(T - T_0)}\right), \tag{4.6}$$

where σ_i is the ionic conductivity, A_i is a pre-exponential factor proportional to the number of ionic charge carriers, E_i is the pseudo-activation energy for ion motion, R is the gas constant, T is the temperature, and T_0 is a reference temperature which is typically 25 K below the glass transition temperature of PEO.[147] We left T_0 as a fit parameter because the glass

transition temperature of PEO changes with added salt. The temperature dependence on electronic conductivity was fit to the Arrhenius equation:

$$\sigma_e = A_e \exp\left(\frac{E_e}{RT}\right), \tag{4.7}$$

where σ_e is the electronic conductivity, A_e is a pre-exponential factor, E_e is the activation energy for electronic charge transport. The application of the Arrhenius model assumes the conduction mechanism is through thermally activated hopping, which is common for undoped semiconducting polymers.[148] The resulting fit parameters using equations (4.6) and (4.7) are given in the caption of Figure 4.5.

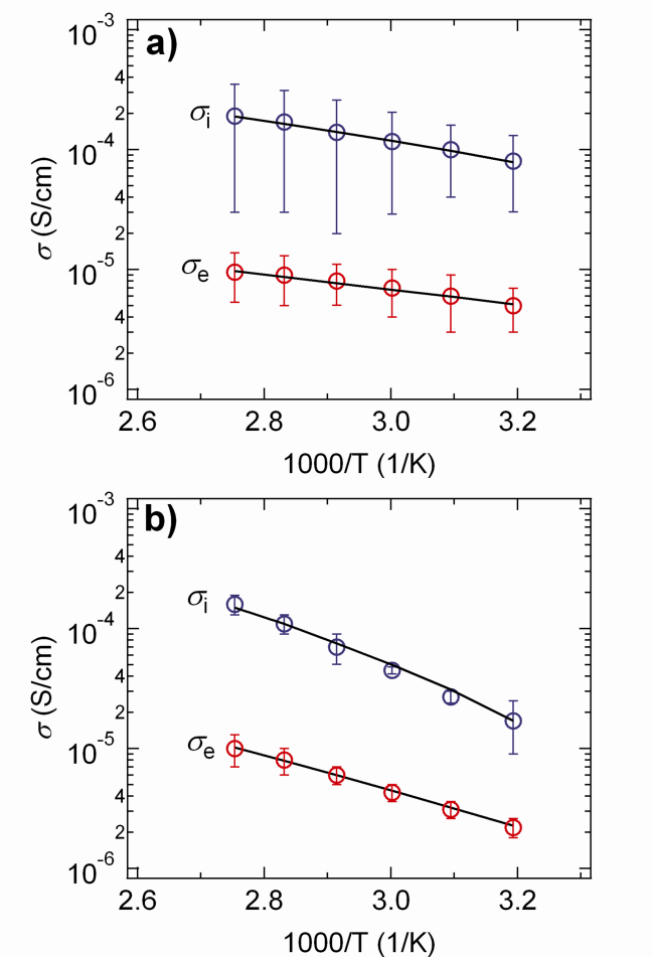

Figure 4.5. Temperature dependence of ionic and electronic conductivity for (a) P3HT-PEO(9-2) at r_0 = 0.085 and (b) P3HT-PEO(6-2) at r_0 = 0.085. Open symbols are experimental data and solid curves are fits using the VTF and Arrhenius equations for ionic and electronic conductivities, respectively. The VTF fit parameters are A_i = 1.63 x 10^{-3} S/cm, E_i = 0.032 eV, and T_0 = 190K for P3HT-PEO(9-2) and A_i = 1.00 x 10^{-2} S/cm , E_i =0.066 eV, and T_0 = 200K for P3HT-PEO(6-2). The Arrhenius fit parameters are A_e = 5.14 x 10^{-4} S/cm and E_e = 0.125 eV, for P3HT-PEO(9-2), and A_e = 1.2 x 10^{-2} S/cm S/cm and E_e = 0.210 eV for P3HT-PEO(6-2).

To further analyze the electronic and ionic charge transport properties, we will focus on the data obtained at 90 °C. Figure 4.6 shows σ_e and σ_i of the all three P3HT-PEO samples with and without LiTFSI. The ionic conductivity, σ_i, of P3HT-PEO(5-4) at r_0 = 0.085 is (3.9±0.6) x 10^{-4} S/cm, which is the highest among three block copolymer samples. This is not surprising as this polymer has the highest PEO volume fraction. The ionic conductivities of P3HT-PEO(9-2) and P3HT-PEO(6-2) at r_0 = 0.085 are within experimental error, in spite of the difference in PEO volume fraction. The values of σ_i reported here are similar to the reported ionic conductivities of other PEO-containing block copolymers.[86] All of the previous data (*e.g.* ref. 85) on PEO-containing block copolymers are restricted to systems wherein the non-ionically conducting block was insulating. The values of σ_e of P3HT-PEO(9-2) and P3HT-PEO(6-2) at r_0 = 0.085 are (9±4) x 10^{-6} S/cm and (1.0±0.3) x 10^{-5} S/cm. A significantly lower value of (3.6±0.9) x 10^{-8} S/cm was obtained from P3HT-PEO(5-4) at r_0 = 0.085. The neat P3HT-PEO samples (r_0 = 0) samples exhibited data that were similar to those obtained from P3HT-PEO/LiTFSI mixtures, but with two semicircles as shown in Figure 4.7 for P3HT-PEO(6-2). The analysis described above holds for these samples and the low frequency Z' intercept gives R_e. The dc-test showed that σ_e of neat P3HT-PEO(6-2) was (4.4±0.3) x 10^{-7} S/cm at 90 °C, which is in good agreement with σ_e of (5±2) x 10^{-7} S/cm from ac impedance spectroscopy. The effect of added salt on the electronic conductivities of the P3HT-PEO copolymers is shown in Figure 4.6. σ_e of P3HT-PEO(5-4) does not change appreciably when r_0 is increased from 0 to 0.085. One might anticipate this result if all of the added LiTFSI were preferentially located in the PEO microphase. In contrast, σ_e values of P3HT-PEO(9-2) and P3HT-PEO(6-2) increase by factors of 28.1 and 23.0 when r_0 is increased from 0 to 0.085, indicating that the electronic conductivity of the P3HT microphases is affected by LiTFSI.

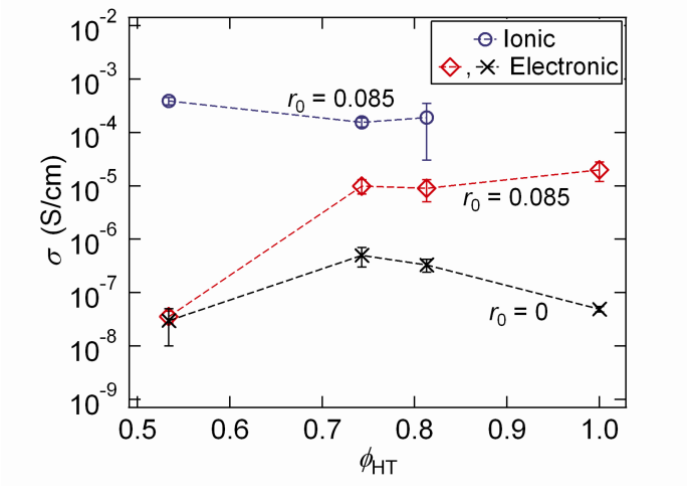

Figure 4.6. Electronic conductivity of P3HT homopolymer and P3HT-PEO block copolymers as a function of the P3HT volume fraction, ϕ_{HT}, at 90 °C. Measurements were made with (r_0 = 0.085) and without (r_0 = 0) added salt. The ϕ_{HT} values for the three block copolymers are given in Table 1. The ϕ_{HT} = 1 data set corresponds to homopolymer P3HT(5), and the salt concentration of 0.085 is actually r_{HT}. The ionic conductivities of the P3HT-PEO block copolymers were only measured with added salt (r_0 = 0.085). The dashed lines are guides for the eye.

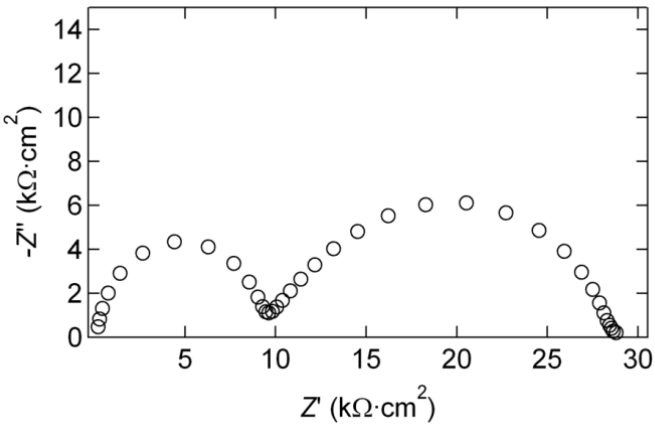

Figure 4.7. Nyquist impedance plot (-*Z*'' *vs. Z*') at 90 °C for P3HT-PEO(6-2) at $r_0 = 0$. The *Z*' intercept of the rightmost semicircle gives the electronic resistance.

The above observation motivated us to prepare several P3HT(5)/LiTFSI mixtures in the concentration range $0 \leq r_{HT} \leq 0.15$, where r_{HT} is the molar ratio of LiTFSI to 3-hexylthiophene monomer (refer to method section for details). The mixtures appeared homogeneous and with a clear red color when viewed by the naked eye (which could indicate the absence of chemical doping). This was further confirmed through solution (THF) and solid-state UV-VIS measurements as shown in Figure 4.8a-b. Figure 4.9a shows the Nyquist plot of the P3HT(5)/LiTFSI mixture at $r_{HT} = 0.085$. It contains two semicircles with no capacitive tail and thus the touchdown of the second semicircle gives the electronic resistance R_e, which was confirmed by dc measurements. In Figure 4.9b, we show the electronic conductivity of P3HT(5)/LiTFSI mixtures, σ_{HT}, as a function of r_{HT} at 90 °C. σ_{HT} increases rapidly with increasing r_{HT} in the $r_{HT} \leq 0.04$ regime. The right hand-axis in Figure 4.9b plots $\sigma_{HT,N}$ as a function of r_{HT}, where $\sigma_{HT,N}$ is the normalized electronic conductivity of P3HT(5)/LiTFSI, defined as the ratio of σ_{HT} at the r_{HT} of interest to σ_{HT} at r_{HT}=0. The increase in electronic conductivity cannot be attributed to increase in crystallinity as there is no clear trend with salt concentration (Figure 4.8c). It should be noted that the salt has no effect on the melting and crystallization temperature of P3HT as shown in Figure 4.8c.

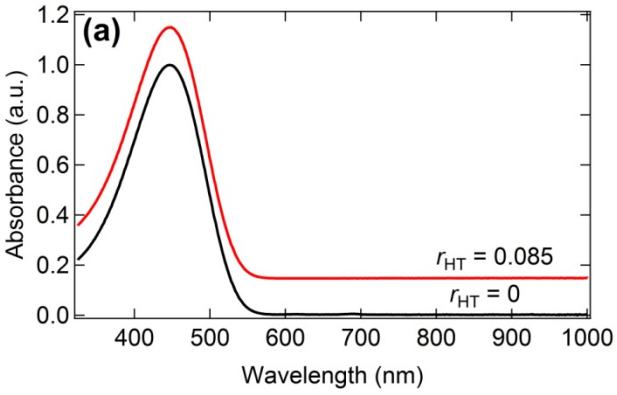

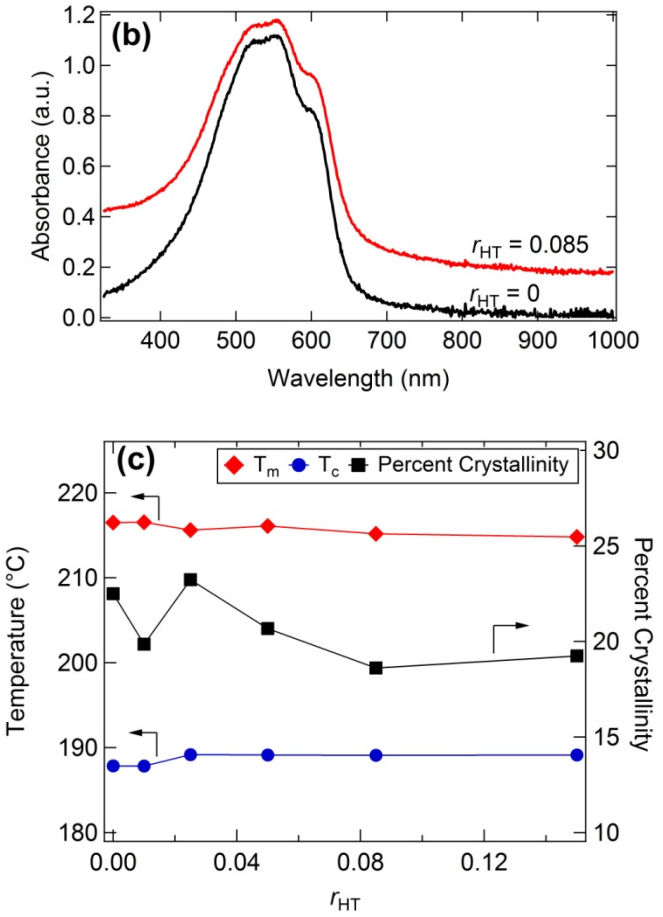

Figure 4.8. **(a)** Solution UV-VIS (THF) of P3HT(5) at r_{HT} = 0 and r_{HT} = 0.085. The maximum absorption is at λ = 447 nm for both cases. **(b)** Solid-state UV-VIS (THF) of P3HT(5) at r_{HT} = 0 and r_{HT} = 0.085. The maximum absorption peaks/shoulders are at λ = 525, 558, 608 for both cases. This indicates that LiTFSI is not doping P3HT or any change in conjugation length due to structural changes. **(c)** DSC data (T_m, T_c, and percent crystallinity) of P3HT with LiTFSI.

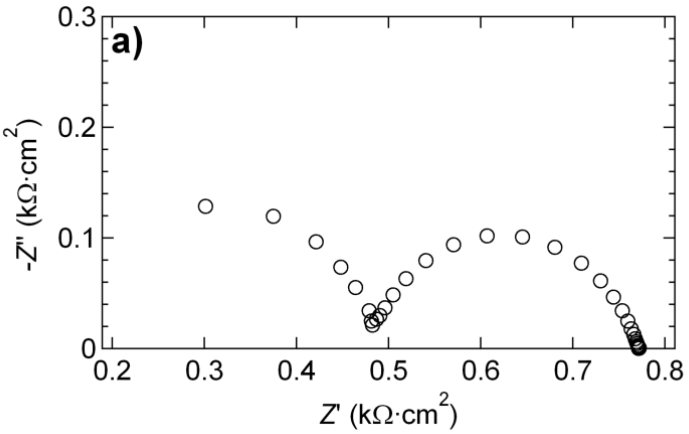

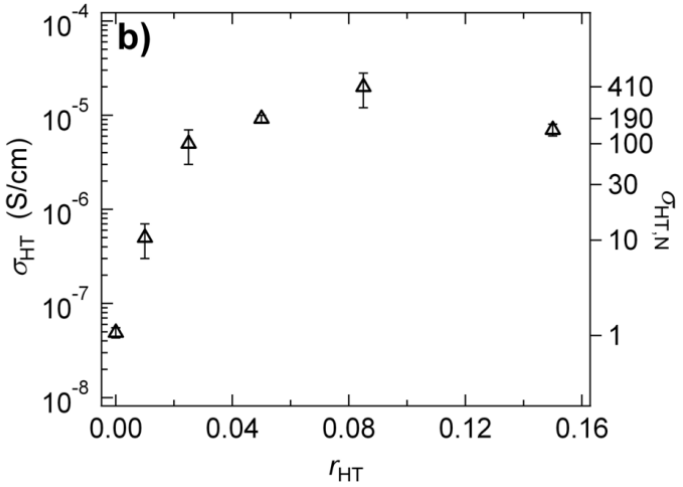

Figure 4.9. **(a)** Nyquist impedance plot (-*Z*'' *vs. Z*') at 90 °C for an P3HT(5)/LiTFSI mixture with salt concentration r_{HT} = 0.085. The *Z*' intercept of the rightmost semicircle gives the electronic resistance. **(b)** Electronic conductivity, σ_{HT}, at 90 °C for P3HT(5)/LiTFSI salt mixtures at various salt concentrations. Right-hand axis corresponds to the normalized P3HT electronic conductivity, $\sigma_{HT,N}$ (relative to σ_{HT} at r_{HT} = 0), as defined by Equation 4.8. This data is used to determine the partitioning of salt in the P3HT microphase as described in the text.

Returning to the electronic conductivity data in Figure 4.6, we make the simplifying assumption that the increase in electronic conductivity of the P3HT-PEO/LiTFSI mixtures relative to neat P3HT-PEO is due to mixing of some of the added LiTFSI with the P3HT. We define *k* for each of the block copolymers as:

$$k = \frac{\sigma_e(r_0 = 0.085)}{\sigma_e(r_0 = 0)}. \tag{4.8}$$

The values of *k* for P3HT-PEO(9-2), P3HT-PEO(6-2), and P3HT-PEO(5-4) are 28.1, 23.0, and 1.14, respectively. The concentration of LiTFSI in the P3HT microphase is obtained by determining the value of r_{HT} in Figure 4.9b where $\sigma_{HT,N} = k$. The LiTFSI concentrations in the P3HT microphase thus obtained are tabulated in Table 4.2. Also given in Table 4.2 are the inferred LiTFSI concentrations in the PEO microphase obtained by mass balance:

$$\frac{w_{EO}}{M_{0,EO}} r_0 = \frac{[1 - w_{EO}]}{M_{0,HT}} r_{HT} + \frac{w_{EO}}{M_{0,EO}} r_{EO}, \tag{4.9}$$

where r_{EO} is the salt concentration in the PEO microphase, w_{EO} is the PEO microphase weight fraction, $M_{0,EO}$ is the PEO repeat unit molecular weight, and $M_{0,HT}$ is the P3HT repeat unit molecular weight. It is evident from Table 4.2 that about 20% of the added salt partitions into the P3HT microphases in samples P3HT-PEO(9-2) and P3HT-PEO(6-2). This suggests that LiTFSI has an affinity towards the P3HT microphases with the nanofibrillar morphology.

Table 4.2. Estimated values LiTFSI salt concentrations in P3HT, r_{HT}, and in PEO, r_{EO} for P3HT-PEO salt mixtures at $r_0 = 0.085$ and 90 °C.

Polymer Name	r_{HT}	r_{EO}
P3HT-PEO(9-2)	**0.017±0.003**	0.065±0.003
P3HT-PEO(6-2)	**0.016±0.002**	0.072±0.001
P3HT-PEO(5-4)	**0.0003±0.0004**	0.0849±0.0001

We define a normalized ionic conductivity,

$$\sigma_{i,N} = \frac{\sigma_i}{\phi_{EO}\sigma_{EO}(r_{EO})}, \tag{4.10}$$

where ϕ_{EO} is the EO volume fraction, $\sigma_{EO}(r_{EO})$ is the ionic conductivity of pure PEO homopolymer at a salt concentration of r_{EO} at the temperature of interest. If equation 4.1 were valid and the intrinsic conductivity of the PEO microdomains in the P3HT-PEO/LiTFSI mixtures were identical to σ_{EO} then $\sigma_{i,N} = f_i$, the morphology factor for ionic conduction. The values of σ_{EO} used in the normalization were obtained at r_{EO} values provided in Table 4.2 using previously reported conductivity measurements on mixtures of PEO homopolymer and LiTFSI.[53, 149] The ionic conductivity of LiTFSI and PEO homopolymer mixtures is independent of polymer molecular weight over the range of this study ($M_{n,PEO}$ of 2 to 4.2 kg/mol).[55] This justifies our use of a molecular-weight-independent value of σ_{EO} in equation 4.10. The values of $\sigma_{i,N}$ thus obtained at 90 °C are listed in Table 4.3. For well-connected lamellae, the expected value of f_i is 0.67. The reported values of $\sigma_{i,N}$ in Table 4.3 are less than this, an observation that is consistent with measurements of ionic conductivity of PS-PEO block copolymers in the low molecular weight limit.[122]

Table 4.3. Normalized ionic conductivity, $\sigma_{i,N}$ and electronic conductivity, $\sigma_{e,N}$ for P3HT-PEO/LiTFSI salt mixtures at $r_0 = 0.085$ and 90 °C.

Polymer Name	$\underline{\sigma}_{i,N}$	$\underline{\sigma}_{e,N}$
P3HT-PEO(9-2)	0.6±0.5	8±2
P3HT-PEO(6-2)	0.33±0.06	12±5
P3HT-PEO(5-4)	0.48±0.06	1.2±0.9

The electronic conductivity of P3HT-PEO block copolymers can be analyzed by a scheme similar to that described in the preceding paragraph. The normalized electronic conductivity of a block copolymer, $\sigma_{e,N}$ is defined as

$$\sigma_{e,N} = \frac{\sigma_e(r_0 = 0.085)}{\phi_{HT}\sigma_{HT}(r_{HT})} = \frac{\sigma_e(r_0 = 0)}{\phi_{HT}\sigma_{HT}(r_{HT} = 0)}, \quad (4.11)$$

where ϕ_{HT} is the P3HT volume fraction, σ_e is the electronic conductivity of the block copolymer, and $\sigma_{HT}(r_{HT})$ is that of P3HT(5) homopolymer at salt concentration r_{HT} for each block copolymer given in Table 2. The second equality arises due to our approach for obtaining r_{HT}. As was the case with normalizing ionic conductivity, we assume that σ_{HT} is independent of P3HT molecular weight over the range of this study ($M_{n,P3HT}$ of 5 to 9 kg/mol). To our knowledge, the effect of molecular weight on conductivity, the product of charge carrier mobility and concentration, for bulk P3HT samples have not been reported. Previous work shows that changing $M_{n,P3HT}$ from 3 to 30 kg/mol results in a factor of 25 increase in mobility in a diode configuration,[150] and a factor of 10,000 increase in mobility in a transistor configuration.[47] It is important to note that the reported mobilities are obtained from measurements on thin films (20-200 nm), and that the measured properties depend on substrate effects and processing conditions. Further work is thus required to determine the limitations of the proposed normalization procedure for electronic conductivity in block copolymers.

The values of $\sigma_{e,N}$ obtained from equation 4.11 are listed in Table 4.3. The values of $\sigma_{e,N}$ of P3HT-PEO(9-2) and P3HT-PEO(6-2) are significantly greater than unity. It is clear that in this case, $\sigma_{e,N}$ is not equal to the morphology factor which, by definition is less than unity. The $\sigma_{e,N}$ values listed in Table 4.3 should be interpreted as lower bounds for the increase in intrinsic electronic conductivity of P3HT microphase due to nanostructuring. Thus the intrinsic electronic conductivity of P3HT domains in P3HT-PEO(6-2) is at least a factor of 12 larger than that of P3HT(5) homopolymer. This factor is 8 for P3HT-PEO(9-2) and not significantly different from unity for P3HT-PEO(5-4) (Table 4.3). Note that the largest increase is obtained in the P3HT-PEO(6-2) sample wherein the molecular weight of the P3HT block is closely matched to the P3HT homopolymer. The higher conductivity of the asymmetric block copolymers is unexpected due to the presence of the electronically insulating PEO microphase. Studies on poly(3-alkylthiophenes) (P3AT) and electronically insulating polymer composites have shown a similar increase in electronic conductivity at high P3AT weight fractions.[151-153] The results of these studies suggest that properties of the material surrounding the crystalline P3AT regions affect the electronic charge transport.[152]

It is important to note that the data in Tables 4.2 and 4.3 are based on the simplest possible interpretation of the available data. The factor by which conductivity of pure P3HT increases with added salt might be different from that obtained in P3HT-containing block copolymers. Note that the dependence of σ_e on ϕ_{HT} is non-monotonic and presented on a logarithmic scale in Figure 4.6. This cannot be anticipated from equation 4.1 which predicts a monotonic (linear) increase of σ_e with increasing ϕ_{HT}.

4.4 Conclusions

We have explored the relationship between morphology and transport of both electronic and ionic charge in block copolymer/salt mixtures. A key difference between the present samples and those used in previous studies on charge transport in block copolymers[30, 85, 86, 154, 155] is both ionic and electronic charges are transported simultaneously in the present system. A combination of ac impedance spectroscopy and dc measurements enables the determination of electronic and ionic conductivity in our samples. We discovered that the addition of LiTFSI to P3HT homopolymer results in approximately 400-fold increase in electronic conductivity at high salt concentrations. By combining this result with measurements of electronic conductivity of P3HT-PEO copolymers with and without salt we estimated the extent to which LiTFSI partitions between the P3HT and PEO microphases. The ionic conductivities of P3HT-PEO/LiTFSI mixtures are lower than those of PEO/LiTFSI mixtures. This is expected due to the presence of the non-ionically-conducting P3HT microphases in the P3HT-PEO/LiTFSI mixtures (see equation 4.1). Neat P3HT-PEO copolymers only transport electronic charge. The electronic conductivities of the neat asymmetric P3HT-PEO copolymers are significantly higher than those of the P3HT homopolymer. This is unexpected because one expects the presence of the non-electronically-conducting PEO microphases in P3HT-PEO to result in a decrease in electronic conductivity (see equation 4.1). We hope to identify the reason for this observation in future work.

Chapter 5 - Electronic Charge Transport Properties of Electrochemically Oxidized Block Copolymers – Lithium Battery Application

ABSTRACT

Block copolymers that can simultaneously conduct electronic and ionic charges on the nanometers length scale can serve as innovate conductive binder material for solid-state battery electrodes. The purpose of this work is study the electronic charge transport of poly(3-hexylthiophene)-*b*-poly(ethylene oxide) (P3HT-PEO) copolymers electrochemically oxidized with lithium bis(trifluoromethanesulfonyl) imide (LiTFSI) salt. We use a solid-state three-terminal electrochemical cell that enables simultaneous conductivity measurements and control over electrochemical doping of P3HT. At low oxidation levels (ratio of moles of electrons removed to moles of 3-hexylthiophene moieties in the electrode), the electronic conductivity increases from 10^{-8} S/cm to 10^{-4} S/cm. At high oxidation levels, $\sigma_{e,ox}$ approaches 10^{-2} S/cm. When P3HT-PEO is used as a conductive binder in a positive electrode with $LiFePO_4$ active material, P3HT is electroactive within the voltage window of a charge/discharge cycle. The electronic conductivity of the P3HT-PEO binder is in the 10^{-4} to 10^{-2} S/cm range over most of the potential window of the charge/discharge cycle. This allows for efficient electronic conduction and observed charge/discharge capacities approach the theoretical limit of $LiFePO_4$. However, at the end of the discharge cycle, the electronic conductivity decreases sharply to 10^{-7} S/cm, which means the "conductive" binder is now electronically insulating. The ability of our conductive binder to switch between electronically conducting and insulating states in the positive electrode provides an unprecedented route for automatic overdischarge protection in batteries.

5.1 Introduction

Materials with nanostructured conducting domains are essential for a wide range of applications related to alternative energy.[156] Organic solar cells require nanoscale electron and hole-conducting domains to promote charge separation and extraction.[6] Active materials in battery and fuel cell electrodes such as $LiFePO_4$, graphite, and platinum, are either electronic or ionic insulators.[81, 103, 104, 156] Nanoscale electron- and ion-conducting domains are necessary for enabling redox reactions in these materials.[81, 103, 104] For example, a traditional porous lithium battery electrode consists of a redox-active material, carbon black for electronic conduction, and non-conductive binder that holds the particles in place. The pores are backfilled filled with organic electrolyte for ionic conduction. In some cases such

as $LiFePO_4$, electronic and ionic conductivities are so low that the active materials must be in nanoparticle form, and addressing such particles requires the transport of both kinds of charges to occur on nanometer length scales. Materials such as block copolymers can self-assemble and form co-continuous nanoscale domains such as alternating lamellae, cylinders, or cubic gyroid phase.[59] Ionic conduction can, in principle, occur in one of the domains and electronic conduction in the other. In this study, which builds on the work in refs. 30 and 33, poly(3-hexylthiophene)-*block*-poly(ethylene oxide) (P3HT-PEO) copolymers are used to conducts both electronic and ionic charges. P3HT-PEO block copolymer molecules self-assemble on the nanometer length scale to yield P3HT-domains that conduct electronic charges and PEO-domains that conduct ionic charges. One can thus construct an electrode that only consists of the redox-active material and P3HT-PEO block copolymer.

P3HT is essentially an electronic insulator in its pristine state; it is formally a semiconductor with bulk electronic conductivity in the range of of 10^{-5} - 10^{-8} S/cm.[31-35, 38, 40] It is likely broad range of the conductivity is due to the presence of small concentrations of contaminants. The electronic conductivity of conjugated polymers is increased by chemical doping, i.e. the addition of chemical species such as ferric chloride, or by electrochemical doping, i.e. the introduction of ionic species such as PF_6^- under applied electrochemical potentials.[1, 11-13, 15, 41] Seminal work of Chiang et al. showed that chemical doping increases the electronic conductivity of poly(acetylene) from 10^{-9} S/cm to 10^2 S/cm after doping.[1] In the case of chemical doping, introduction of an oxidizing agent such as I_2 results in a spontaneous oxidation of the conjugated polymer. In the case of electrochemical doping, an applied potential drives the oxidation of the conjugated polymer. A formal positive charge (hole) created on the polymer backbone is compensated by diffusion of a dopant counterion into the polymer from the surrounding electrolyte. Electrochemical doping provides a unique avenue for designing the next generation of electrodes because it enables the possibility of turning redox reactions on and off reversibly through the control of applied potentials. This is in stark contrast to the traditional carbon additives used to conduct electrons in current battery and fuel cell electrodes which have a fixed electronic conductivity.

The purpose of this study is to characterize the electronic transport in electrochemically doped P3HT-PEO block copolymers. We use a novel three-terminal cell that enables simultaneous conductivity measurements and control over electrochemical doping of P3HT. The results of our experiments provide further insight on the charge transport properties of P3HT-PEO block copolymers when used to conduct electronic and ionic charges in a lithium battery electrode. In particular, we demonstrate the semiconducting properties of P3HT enable automatic overdischarge protection of the lithium battery.

The combination of conjugated polymers and electrolytes has been used in organic electrochemical transistors[157-160] and batteries (as the primary active material for electrodes[8, 9, 161, 162] and for overcharge protection[42, 163, 164]). The traditional electrochemical oxidation of conjugated polymers consists of polymer films submerged or swollen with a liquid electrolyte.[41, 42] In the case of solid-state organic electrochemical transistors, the conjugated polymer and polymer electrolyte are assembled as a bilayer. The conjugated polymer and polymer electrolyte are not chemically bonded across the interface between them. Our polymer is a unique electrochemical system in that the electrolyte is a solid polymer that is covalently bonded to the electronically conducting polymer. Block copolymer thermodynamics ensures microphase separation into co-continuous electronically conducting

P3HT and ionically conducting PEO domains on the nanometer length scale. The characteristic periodic length scale for P3HT-PEO block copolymers used in this study is around 20 nm.[123] As a result, the dopant counterions only have to diffuse a few nanometers to compensate for the charged nature of the electrochemically oxidized P3HT chains. This can, in principle, enable rapid and efficient counterion diffusion during redox reactions.

5.2 Methods

5.2.1 *Two-terminal conductivity and two-terminal electrochemical cell preparation*

Samples for conductivity measurements were prepared by hot pressing freeze-dried P3HT-PEO block copolymer with LiTFSI into a 125 μm thick Garolite G-10 spacer with an inner-hole diameter of 3.88 mm. To assemble a two-terminal conductivity cell, nickel foil current collectors were pressed on both sides of the spacer at 90 °C. Nickel tabs were placed on both nickel foils. The sample was then sealed in aluminum laminated pouch material (Showa Denko) using a vacuum sealer (Packing Aids Corp). To assemble the two-terminal electrochemical cell (Figure 5.1), we first measured the mass of the spacer before and after the addition of the polymer. A nickel foil current collector was pressed on one side of the spacer while a piece of polymer electrolyte membrane approximately 3/16" in diameter (PS-PEO block copolymer with LiTFSI at $r_0 = 0.085$) was gently pressed on the other side of the spacer. A disk with 3/16" diameter was punched from 150 μm thick lithium foil (FMC) and was gently pressed on the other side of the polymer electrolyte membrane. Nickel tabs were placed on the lithium and on the nickel foil. The sample was then sealed in aluminum laminated pouch material using a vacuum sealer. Samples were prepared and sealed in an argon-filled glovebox to ensure that the samples are air- and water-free.

5.2.2 *Three-terminal conductivity and three-terminal electrochemical cell preparation*

First, the P3HT-PEO/LiTFSI mixture was pressed into two separate spacers at 90 ^{o}C. The mass of the spacer was recorded before and after the addition of the polymer. The thickness, L, of each polymer filled spacer was measured (150-200 μm). Due to overfilling the spacer hole, the actual thickness is slightly larger than the spacer thickness, but is not an issue for taking measurements as the polymer is a hard solid at 90 ^{o}C. Next, a piece of electroformed nickel mesh (Industrial Netting) was gently pressed between two spacers at 90 °C. This step needs to be done very carefully to ensure the mesh is not damaged and that the two polymer layers come into good contact to ensure negligible resistance at the interface of the two layers. For the three-terminal conductivity cell (Figure 5.4a), nickel foil was gently pressed on both sides of the spacer. Nickel tabs were added to both nickel foil electrodes and the nickel mesh electrodes. The sample was then sealed in aluminum laminated pouch material using a vacuum sealer. In the case of the three-terminal electrochemical cell (Figure 5.3), a nickel foil electrode was gently pressed on one side of the spacer while piece of polymer electrolyte membrane was gently pressed on the other side of the spacer. A disk

with 3/16" diameter was punched from 150 μm thick lithium foil and was gently pressed on the other side of the polymer electrolyte membrane. Nickel tabs were placed on the lithium, the nickel foil electrode, and the nickel mesh electrode. The sample was then sealed in aluminum laminated pouch material using a vacuum sealer. Samples were prepared and sealed in an argon-filled glovebox to ensure that the samples are air- and water-free.

5.2.3 *Galvanostatic Experiments for Electrochemical Oxidation*

Galvanostatic oxidation experiments were performed using a Bio-Logic VMP3 instrument and the Bio-Logic EC-Lab data acquisition software. A current density (i) of 0.17 mA/cm^2 is applied to the electrochemical cell for a specific amount of time (t). The oxidation level is denoted as r_{ox}, which is the ratio between the moles of electrons (e^-) removed to the moles of the 3-hexylthiophene moieties. The mole of e^- removed is quantified using the following equation: moles $e^- = iAF/t$, where A is the area of the sample (0.118 cm^2) and F is Faraday's constant. The moles of e^- removed equals the moles of TFSI$^-$ counterions needed to stabilize the holes generated. After reaching the desired r_{ox} value, the cell is allowed to rest until the voltage begins to stabilize as shown in Figure 2a. This value is taken as the equilibrium voltage (E_{ox}) corresponding to the desired r_{ox} value.

5.2.4 *Conductivity measurements using impedance spectroscopy*

The impedance spectroscopy measurements were made using a Bio-Logics VMP3 instrument and Bio-Logic EC-Lab data acquisition software. The applied ac voltages was 50 mV with frequencies ranging from 1MHz to 1 mHz. Resistances were calculated from the complex impedance data ($Z^* = Z' - iZ''$) where Z' and Z'' are the real and imaginary impedances, respectively, using Nyquist plots ($-Z''$ *vs.* Z'). The conductivity, σ, is given by

$$\sigma = \frac{L}{R}, \tag{5.1}$$

where L is the polymer thickness and R is the resistance ($\Omega \cdot cm^2$), obtained from intersections of the Nyquist plots on the Z' axis. All conductivity measurements were averaged over a minimum of three samples and all reported error bars were calculated from one standard deviation. Physical arguments were used to arrive at a particular equivalent circuit. In all cases, we report the parsimonious result, *i.e.* the simplest equivalent circuit with the fewest elements that can describe the data. The Randomize + Simplex algorithm built into the EC-Lab software package was used to fit the impedance data.

5.2.5 *Polymer Electrolyte Film Preparation*

PS-PEO block copolymers and lithium bis(trifluoromethanesulfonyl)imide, LiTFSI mixtures were used as the solid electrolyte. The SEO was synthesized via sequential high-

vacuum anionic polymerization, using *sec*-butyllithium as the initiator and P4 *tert*-butylphosphazene base as the promoter for the polymerization of ethylene oxide. The synthetic procedure used in this study is described in literature.[85, 165, 166] The number-averaged molecular weight and the polydispersity index (PDI) of the PS block were obtained using gel permeation chromatography measurements using a Waters 2690 separations module and a Viscotek triple detector system calibrated with polystyrene standards. The PDI of the polymer was found to be less than 1.05. The volume fraction of each block was determined using ^{1}H nuclear magnetic resonance (NMR) spectroscopy. The M_n of the PS block is 52.9 kg/mol and M_n of the PEO block is 67.6 g/mol. The volume fraction of PEO (ϕ_{EO}) is 0.54. The dry polymer was dissolved in N-methyl pyrrolidone with LiTFSI. The ratio of Li ions to ethylene oxide moieties, *r*, in our electrolytes was 0.085, the optimal value for this polymer.[86] The solution was cast with a doctor blade and dried under vacuum at 90°C. The resulting free-standing membrane was 20-40 μm thick.

5.2.6 *Battery Assembly*

Solid polymer electrolyte was pressed to the positive electrode that contained P3HT-PEO block copolymer and $LiFePO_4$ particles at 90°C. Lithium metal negative electrode was pressed to the other side of the solid polymer electrolyte at room temperature. These were then analyzed in either Swagelok or pouch cells. Stainless steel Swagelok cells were used to contain samples and provide electrical contact for electrochemical measurements. These cells had fixed bottom electrodes, while the top electrodes had spring-loaded plungers to maintain pressure on the polymer samples. Instrumentation electrodes were connected to the Swagelok cells via glovebox feedthroughs. The Swagelok cells were held in a custom-built heating box equipped with a temperature controller (Omega) that was set so that the cell temperature was 90°C. For pouch cells, a nickel (negative electrode) or aluminum (positive electrode) tab was used as the current collector. The membrane electrode assembly was sealed in aluminum laminated pouch material (Showa Denko) using a vacuum sealer (Packaging Aids Corp), to make them air free. For Swagelok cells, all steps including cycling, were performed in an argon-filled MBraun glovebox, while pouch cells were cycled in a convection oven after vacuum sealing.

5.2.7 *Battery Cycling Procedure*

Battery cycling was performed using either a 16-channel potentiostat/galvanostat (Bio-Logic, VMP3) when using Swagelok cells, or an 8-channel Solartron 1480 potentiostat/cell test system attached to a Tenney TPS environmental test chamber when using pouch cells. The cells were annealed at 90°C for 24 hours prior to analysis. Constant current (0.02 mA/cm^2) was used to charge to 3.8V, and constant voltage was applied until the current decreased to 10% of the original value. The cells enter a rest period of 1 hour, which was then followed by a constant current discharge step to 2.5V. Another 1-hour rest period followed, then the whole process was repeated 9 times to get 10 cycles for each sample cell.

5.3 Results and Discussion

The characteristics of the P3HT-PEO block copolymers used in this study are summarized in Table 1. We examined mixtures of lithium bis-(trifluoromethanesulfonyl) imide salt (LiTFSI) and P3HT-PEO block copolymers listed in Table 5.1. The LiTFSI salt concentration, $r_{0,}$ is equal to 0.085 in all cases, where r_0 is the molar ratio of lithium ion to ethylene oxide moieties. All reported conductivity values were obtained at 90 °C, and reported potentials are relative to a Li/Li^+ reference electrode.

Table 5.1. Characteristics of polymers used in chapter 5.

Polymer Name	$M_{n,P3HT}$ (kg/mol)	$M_{n,PEO}$ (kg/mol)	ϕ_{HT} (P3HT block)	r_{HT}[123]	r_{EO}[123]	Morphology[123]
P3HT-PEO(9-2)	9.0	2.0	0.81	0.017	0.065	Nanofibrillar
P3HT-PEO(6-2)	6.0	2.0	0.74	0.016	0.072	Nanofibrillar
P3HT-PEO(5-4)	5.0	4.2	0.53	0.0003	0.0849	Lamellar

In Chapter 4, we reported on the relationship between morphology and simultaneous electronic and ionic charge transport in P3HT-PEO/LiTFSI mixtures.[123] The same block copolymers were used in Chapter 4 and the current chapter. At 90 °C, the electronic conductivity of P3HT-PEO/LiTFSI mixtures, in the absence of applied potentials, ranged from 10^{-8} to 10^{-5} S/cm. The decoupled ionic conductivity was about 10^{-4} S/cm in all cases, a value that is reasonable for practical lithium battery applications. In addition, we showed a surprising increase in the electronic conductivity by simple chemical mixing of LiTFSI in the P3HT domains. This observation of increased conductivity was surprising as LiTFSI does not have any of the characteristics of traditional chemical dopants, i.e. it did not spontaneously oxidize P3HT. It was shown that the LiTFSI salt partitions between P3HT and PEO microphases. In Table 5.1, we present r_{EO} and r_{HT}, the ratios of the moles of salt to the moles of ethylene oxide and 3-hexylthiophene moieties, respectively, as reported in Chapter 4. It is important to note that the conductivities reported in Chapter 4 correspond to neutral P3HT. In reality, the electronic conductivity can be further increased by electrochemically chemically doping P3HT with LiTFSI.

A variety of electrochemical cells were used in this study. We begin describing results obtained from a two-terminal electrochemical cell shown schematically in Figure 5.1. The negative electrode is lithium metal, which serves as the counter and reference electrode. The positive electrode is the P3HT-PEO/LiTFSI. P3HT (blue) is the redox-active domain and the LiTFSI is primarily dissolved into the PEO domain (red) serves as the electrolyte in the positive electrode. Separating the two electrodes is a block copolymer electrolyte (polystyrene-*block*-polyethylene oxide, PS-PEO) layer with LiTFSI at $r_0 = 0.085$. This layer serves to transport lithium ions between the electrodes. The electrochemical cell configuration (Figure 5.1) is similar to our previously reported work on batteries with a lithium metal anode and lithium iron phosphate ($LiFePO_4$) cathode.[167] The difference being that the positive electrode does not contain $LiFePO_4$ redox-active particles. Removing the

$LiFePO_4$ from the cathode enables the study of the electrochemical properties of P3HT-PEO block copolymers. The two half reactions that occur in the electrochemical cell during the oxidation reaction are shown in Figure 5.1. One of the reactions is the oxidization of P3HT to $P3HT^+$, and the second reaction is the reduction of Li^+ to neutral *Li*. To oxidize P3HT, a positive current is applied to the cell, i.e. an electron is removed from a 3-hexylthiophene moiety to generate a hole charge carrier (p-doping). This causes a TFSI anion to diffuse from the PEO domain into the P3HT domain. In other words, the P3HT has been electrochemically doped with a $TFSI^-$ counterion. At the negative electrode, the electron produced at the P3HT electrode travels through the external circuit to react with a Li^+ ion to form *Li* metal. The Li^+ ion left behind by the transfer of $TFSI^-$ anion into the $P3HT^+$ diffuses into the polymer electrolyte separator to compensate for the consumed Li^+ at the negative electrode. It is assumed that P3HT moieties are oxidized randomly as electrons are removed from the positive electrode, and it has been established that positive charges are separated by about six 3-hexylthiophene moieties.[45] The reactions in Figure 5.1 incorporate these assumptions.

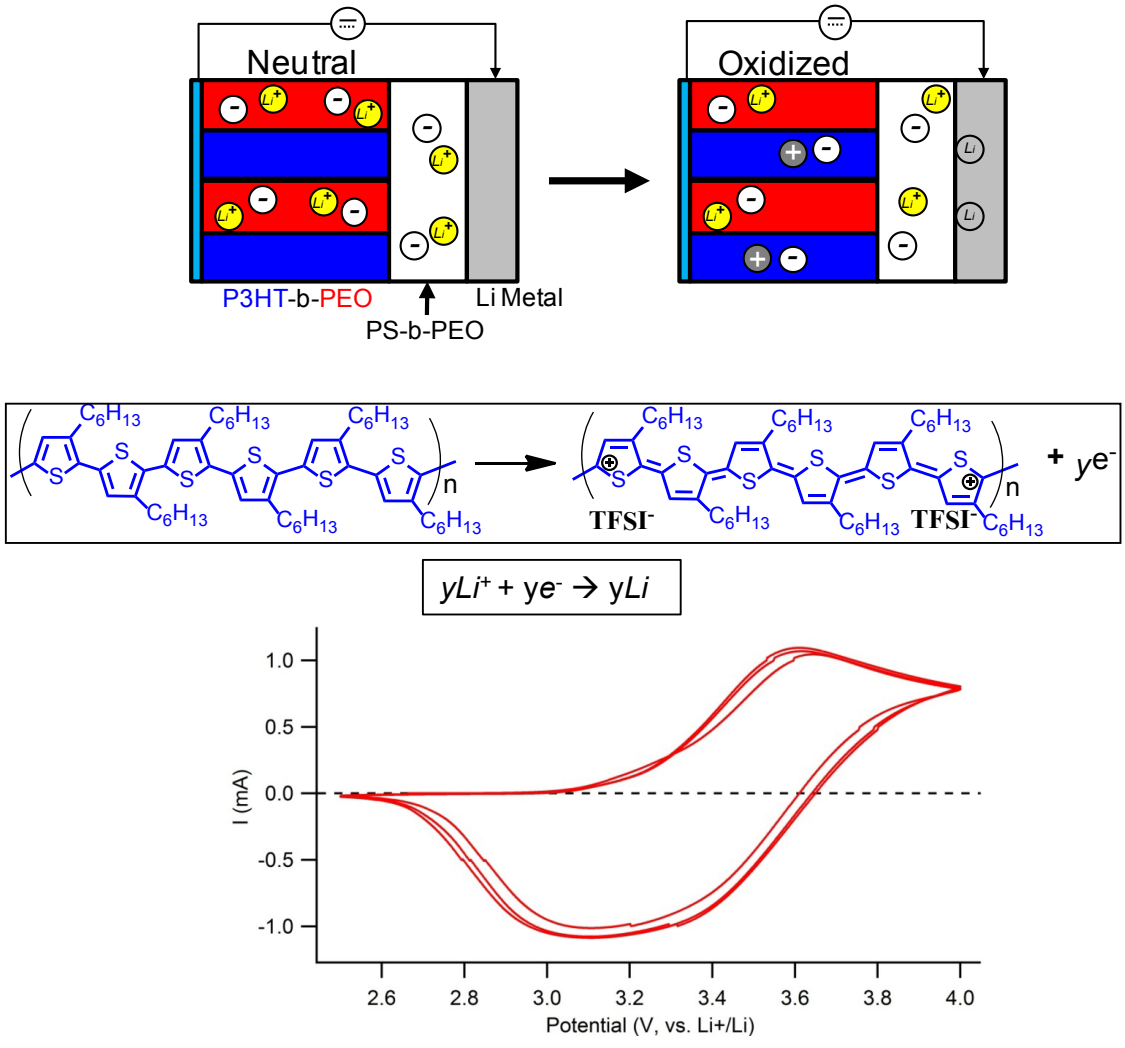

Figure 5.1. Schematic of a two-terminal electrochemical cell. The positive electrode is a nanostructured P3HT-PEO block copolymer with LiTFSI at $r_0 = 0.085$. We show only four lamellar horizontal domains for simplicity. In reality, the block copolymer nanostructure would be composed of randomly orientated grains. The negative electrode is pure lithium metal, which also serves as the reference electrode. Electrons are transported between the positive and negative electrodes by an external circuit. Lithium ions are transported through the PS-PEO block copolymer electrolyte. During the oxidation reaction, an electron is removed from P3HT to generate a hole charge carrier on the polymer backbone. As a result, a $TFSI^-$ counterion diffuses into the P3HT domain from the PEO domain. At the negative electrode, the electron produced at the P3HT-PEO electrode travels through the external circuit to react with a Li^+ ion to form *Li* metal. The Li^+ ion left behind by the transfer of $TFSI^-$ anion into the $P3HT^+$ diffuses into the polymer electrolyte separator to compensate for the consumed Li^+ at the negative electrode. A representative cyclic voltammogram is shown at the bottom. The onset of oxidation is around 3.1V (scanned from 2.5-4.0 V vs. Li/Li^+, scan rate of 20 mV/s). The CV indicates the reversible oxidation of P3HT with LiTFSI.

A cyclic voltammetery experiment on the electrochemical cell depicted in Figure 5.1 indicates an onset oxidation of P3HT is at 3.1 V and an oxidation peak 3.6 V. The initial open circuit voltage (OCV), measured in all of our cells the type in Figure 5.1 is 2.95±0.05. This corresponds to the neutral state of P3HT. The oxidation levels of P3HT were controlled galvanostatically. A current density (i) of 0.17 mA/cm^2 was applied to the electrochemical cell for a specific amount of time (t). In Figure 5.2 we show a plot of resulting cell potential (E_{we}) vs. t of a particular experiment on P3HT-PEO(6-2) where $t = 35$ min. The oxidation level is denoted as r_{ox}, which is the ratio of the moles of electrons (e^-) removed in the galvanostatic experiment to the moles of the 3-hexylthiophene moieties in the positive electrode. The moles of e^- removed are given by, moles $e^- = iAF/t$, where A is the area of the sample (0.118 cm^2) and F is Faraday's constant. We assume that the moles of e^- removed equal the moles of $TFSI^-$ counterions in the oxidized P3HT microphases (r_{ox} equals y/n where y and n are defined in Figure 5.1). After reaching the desired r_{ox} value, the cell is allowed to rest until the E_{we} "stabilizes" as shown in Figure 5.2a. In principle, the rest step allows for the dissipation of the electrode overpotentials and salt concentration gradients in the PS-PEO electrolyte and the P3HT-PEO electrode. It also allows for relaxation of inhomogeneous oxidation fronts that may have developed in the positive electrode. As can be seen Figure 5.2a, even after a rest step of 25 minutes a steady decrease in E_{we} of 0.001 V/min is observed. This may be result of slow diffusion ions across the electrode-electrolyte interface or uncontrolled side reactions. The value of E_{we} is taken as the oxidation potential (E_{ox}), and the corresponding extent of oxidation (r_{ox}) is set by the galvanostatic step. Figure 5.2b shows the results ac impedance spectroscopy measurements taken at $t = 0$ before oxidation and after the rest step at $r_{ox} = 0.01$. It is evident the cell impedance decreases after a small change in r_{ox} from 0 to 0.01. This is a clear sign that the P3HT chains are being oxidized. Even though we see clear evidence of decreasing cell resistance in Figure 5.2b, the challenge lies in extracting the electronic resistance of the P3HT domains in the positive electrode. The cell pictured in Figure 5.1 cannot be used address this challenge as it contains several resistive components including the PS-PEO separator, the P3HT-PEO block copolymer, with concomitant interfacial and charge transfer resistances at each electrode.

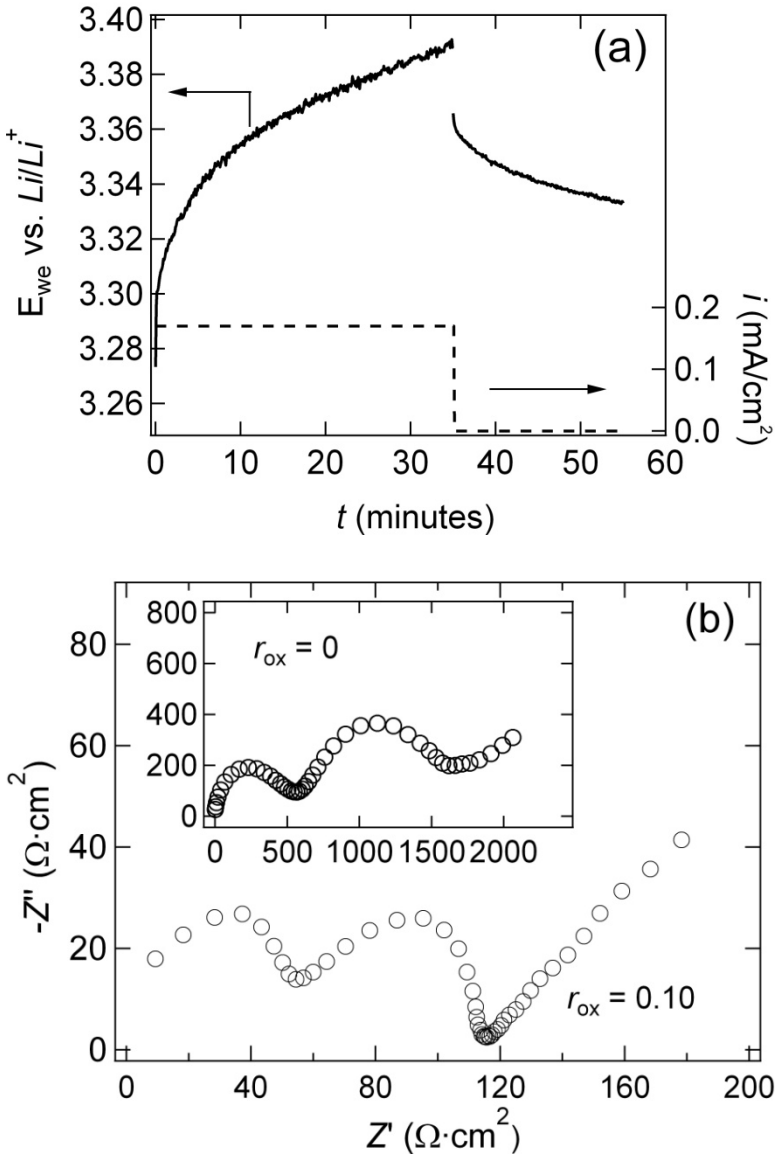

Figure 5.2. (**a**) A characteristic cell voltage (E_{we}) *versus* time (t) profile (solid curve) and current density (i) *versus* t (dashed lines) for the oxidation of P3HT-PEO(6-2) block copolymer with LiTFSI at r_0 = 0.085 using the two-terminal electrochemical cell. A current density of 0.17 mA/cm^2 is applied to the electrochemical cell until the desired oxidation level (r_{ox}) is reached. The cell is allowed to rest (i = 0 mA/cm^2) after which the value of E_{we} is taken as the oxidation potential (E_{ox}). **(b)** Nyquist impedance plot (-Z'' vs. Z') from 1 MHz to 100 mHz of a two-terminal electrochemical cell at 90 °C for r_{ox} = 0 (inset) and r_{ox} =0.10. The positive electrode is P3HT-PEO(6-2) at r_0 = 0.085.

In order to probe the electronic conductivity of the oxidized P3HT-PEO block copolymer directly, we modified the two-terminal cell (Figure 5.1) to include a nickel mesh in the P3HT-PEO positive electrode as shown in Figure 5.3. Following the procedure described above, a constant current is applied between the negative lithium metal electrode and the nickel foil of the positive electrode. After reaching the desired r_{ox} value and allowing

the cell to rest, ac impedance spectroscopy measurements are performed between the nickel foil and the nickel mesh both located in the P3HT-PEO electrode. This measurement quantifies the charge transport in the oxidized P3HT-PEO block copolymer. The E_{ox} value was recorded after the rest step when stable impedance data were obtained (usually less than 30 minutes after the galvanostatic step).

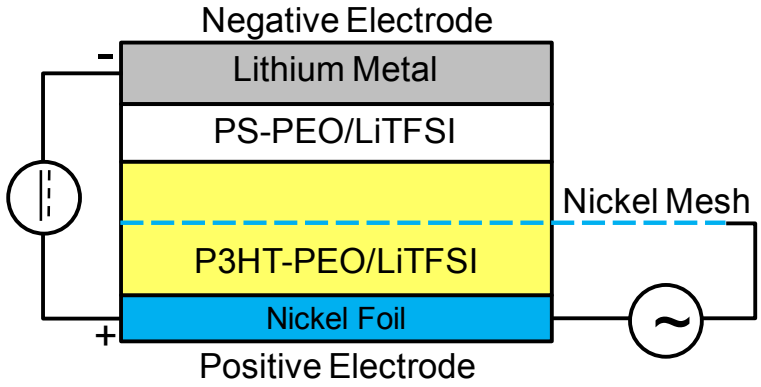

Figure 5.3. Schematic of a three-terminal electrochemical cell that enables simultaneous conductivity measurements and control over electrochemical doping of P3HT. The nickel mesh (third terminal) is placed at the middle of the polymer layer of the positive electrode. The negative electrode is pure lithium metal, which also serves as the reference electrode. By applying a current between the positive and negative electrode, we can control the r_{ox} value of the P3HT-PEO block copolymer. After reaching the desired r_{ox} value, an ac impedance measurement is performed between nickel foil of the positive electrode and the nickel mesh. This measurement allows us to directly quantifying the conductivity of the oxidized P3HT-PEO block copolymer.

In standard impedance measurements, one uses identical parallel plate electrodes to apply potentials and measure the resulting current. If edge effects are neglected, and the field lines are parallel to each other and perpendicular to the electrodes, the conductivity is calculated using Equation 5.1 in the experimental methods section. In contrast, one of the electrodes used in the three-terminal cell is a mesh with 90% open area. In order to quantify the effect of using this mesh as an electrode, experiments were performed on a modified three-terminal cell as shown in Figure 5.4a. The cell in Figure 5.4a is symmetric with a P3HT-PEO/LiTFSI mixture sandwiched between two nickel foils and with a nickel mesh in the middle. Impedance spectra were obtained in two independent experiments. In one case, the spectra were obtained using the two nickel foils as electrodes (foil-foil). In the other case, the spectra were obtained with one of the foils and a nickel mesh as the other electrode (mesh-foil). In Figure 5.4b we show data obtained from a P3HT-PEO(6-2)/LiTFSI mixture. The qualitative features seen in the foil-foil impedance data were similar to those seen in the mesh-foil impedance data. In both cases, the spectra were analyzed by methods described in Chapter 4 to give the electronic (σ_e) and ionic (σ_i) conductivities, using the same total polymer cross-sectional polymer area (0.118 cm^2). The validity of σ_e and σ_i thus obtained may be questioned due to the large void fraction of nickel mesh. In Figure 5.4c, we show the values of σ_e and σ_i of the three P3HT-PEO/LiTFSI samples (Table 5.1). The values of σ_e and σ_i obtained in the foil-foil experiments reported in Figure 5.4c are within experimental

error of those reported in Chapter 4. This is reasonable as one does not expect the presence of the nickel mesh in the sample to have a measurable effect on ion transport in P3HT-PEO. The values of σ_i obtained from the foil-foil and mesh-foil configuration are within experimental error. The σ_e of P3HT-PEO(5-4) and P3HT-PEO(6-2) are also within experimental error. Only σ_e of P3HT-PEO(9-2) from the mesh-foil experiment is significantly different from the foil-foil experiment. With exception of σ_e of P3HT-PEO(5-4), which is near the lower limit of the instrumental resolution, values of $\sigma_{e\ and}$ σ_e obtained from mesh-foil are lower than the foil-foil experiments. One may thus consider σ_e obtained from mesh-foil experiments to be lower limits of the actual electronic conductivity. It is evident from Figure 5.4c, that one cannot account for the mesh electrode using a multiplicative correction factor that applies to all samples. For consistency, we report conductivity values with the mesh-polymer-foil configuration without any corrections.

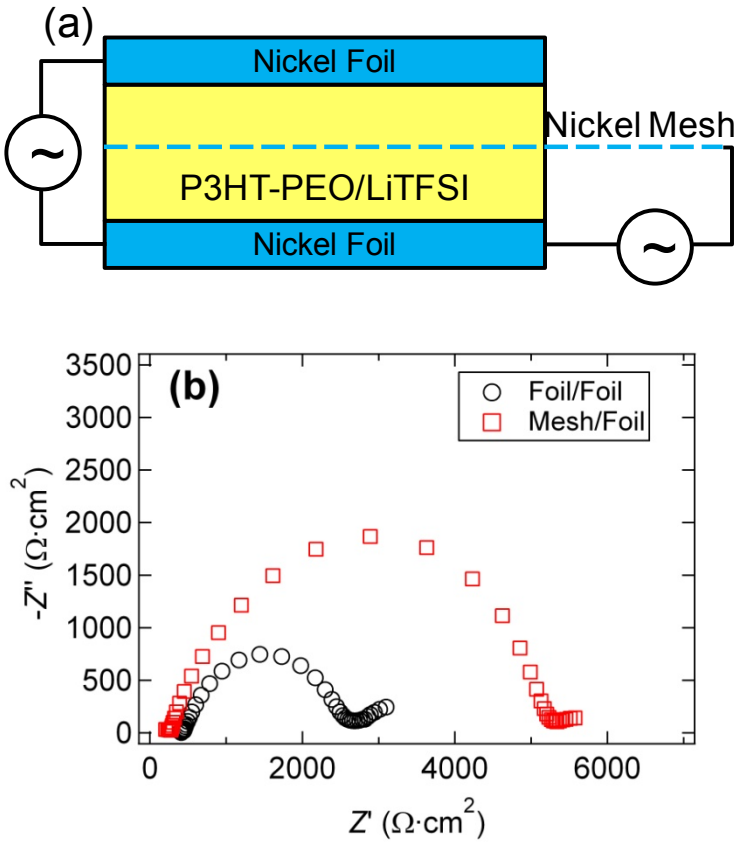

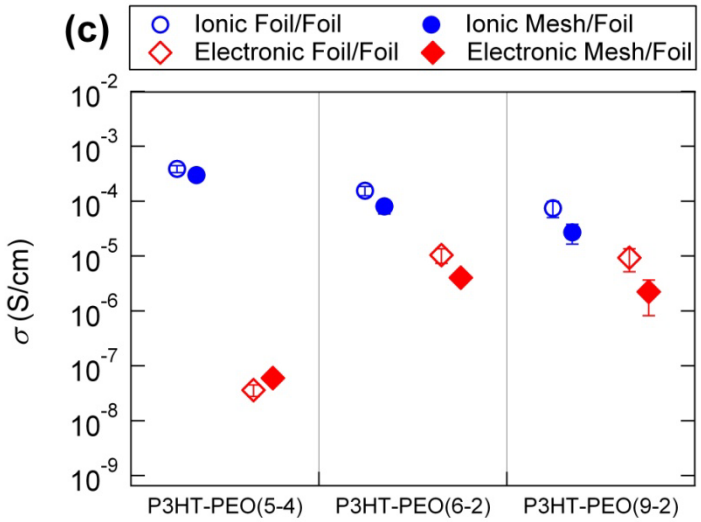

Figure 5.4. **(a)** Schematic of a three-terminal conductivity cell used to quantify the effects of a nickel mesh electrode. **(b)** Representative Nyquist impedance plots (-*Z*'' vs. *Z*') for P3HT-PEO(6-2) at r_0 = 0.085 for a frequency range from 1 MHz to 10 mHz. Measurements are taken between the two nickel foil electrodes and between nickel foil and nickel mesh electrodes. **(c)** Electronic and ionic conductivity at 90 °C of the P3HT-PEO block copolymers at r_0 = 0.085 when measured between foil/foil electrodes and between foil/mesh electrodes.

In Figure 5.5 we show Nyquist impedance plots of P3HT-PEO(6-2) obtained using the three-terminal electrochemical cell at r_{ox} values 0, 0.01, and 0.10. At r_{ox} = 0, the Nyquist plot contains three semicircles. A small increase in r_{ox} to 0.01 results in a Nyquist plot with two semicircles. At r_{ox} 0.10, the Nyquist plot only contains one semicircle. The methodology to obtain the electronic and ionic conductivities of P3HT-PEO/LiTFSI mixtures from Nyquist plots is discussed in length in Chapter 4. Regardless the number of Nyquist semicircles, the electronic resistance, R_e, is given by the intersection of lowest frequency semicircle with the real axis. The curves through the data in Figure 5.5 are fits using the equivalents circuits in the insets of each figure. The method used to obtain the fit is described in Chapter 4. The electronic conductivities of the oxidized polymers ($\sigma_{e,ox}$) were calculated from R_e values thus obtained using Equation 5.1 described in the experimental methods section.

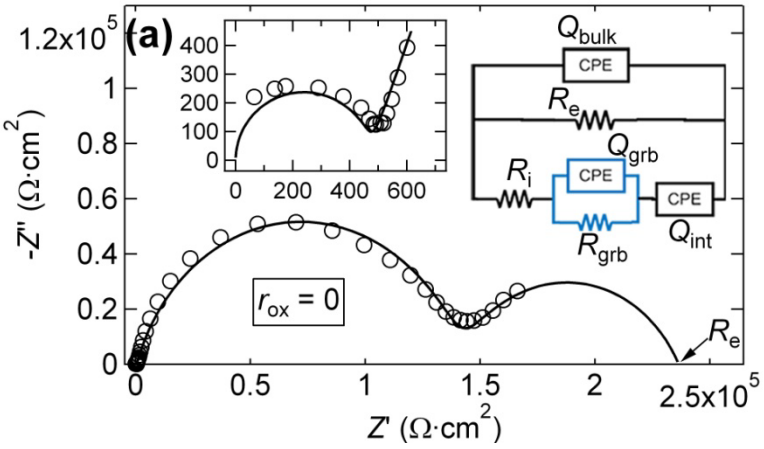

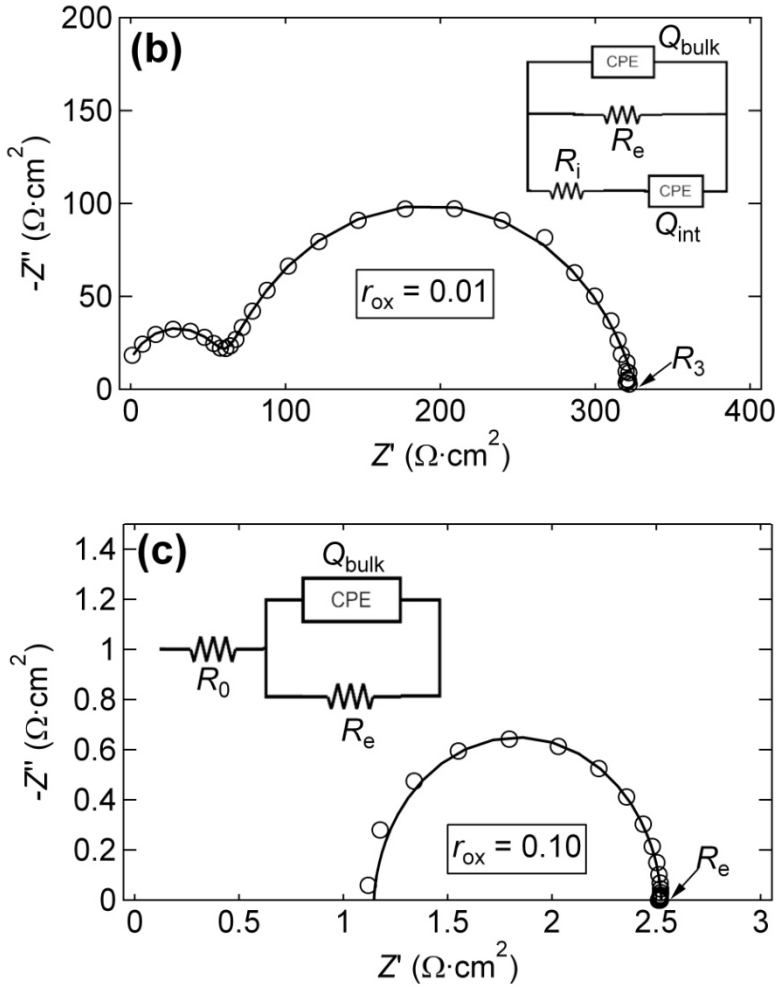

Figure 5.5. (a) Characteristic Nyquist impedance plot (-*Z*'' *vs. Z*') at 90 ^{o}C for P3HT-PEO(6-2) at r_{ox} = 0.01 with frequency range of 1 MHz to 1 mHz. Fit parameters: Q_{bulk} = 2.1 x 10^{-10} F·s^{a-1}, a_{bulk} = 1.0, Q_{int} = 1.60 x 10^{-7} F·s^{a-1}, a_{int} = 0.81, and $R_{i,fit}$ = 473 Ω·cm^2, $R_{grb,fit}$ = 2.4 x 10^5 Ω·cm^2, $R_{e,fit}$ = 2.4 x 10^5 Ω·cm^2. (b) Characteristic Nyquist impedance plot (-*Z*'' *vs. Z*') at 90 ^{o}C for P3HT-PEO(6-2) at r_{ox} = 0.01 with frequency range of 1 MHz to 100 Hz. Fit parameters: Q_{bulk} = 1.51 x 10^{-9} F·s^{a-1}, a_{bulk} = 0.97, Q_{int} = 1.60 x 10^{-7} F·s^{a-1}, a_{int} = 0.81, and $R_{i,fit}$ = 130 Ω·cm^2, $R_{e,fit}$ = 310 Ω·cm^2. (c) Characteristic Nyquist impedance plot (-*Z*'' *vs. Z*') at 90 ^{o}C for P3HT-PEO(6-2) at r_{ox} = 0. 10 with frequency range of 1 MHz to 55 Hz. Fit parameters: Q_{bulk} = 1.7 x 10^{-7} F·s^{a-1}, a_{bulk} = 0.96, and $R_{0,fit}$ = 1.14 Ω·cm^2, $R_{e,fit}$ = 1.40 Ω·cm^2. These measurements are taken between the nickel foil and nickel mesh of the three-terminal electrochemical cell. The open circles represent experimental data while the solid curve corresponds to the fit using the equivalent circuit shown in the inset.

In Figure 5.6, we present $\sigma_{e,ox}$ of electrochemically oxidized P3HT-PEO block copolymers at r_{ox} = 0, 0.01, and 0.10. At r_{ox} = 0, $\sigma_{e,ox}$ is between 10^{-7} and 10^{-8} S/cm for all three polymers. Also shown in Figure 5.6 is the electronic conductivity (σ_e) of unoxidized P3HT-PEO obtained using a two-terminal conductivity cell with nickel foil electrodes. Note that both experiments probe unoxidized P3HT-PEO block copolymers at r_0 = 0.085. In spite of this, it is evident in Figure 5.6 that $\sigma_{e,ox}$ at r_{ox} = 0 is about three orders of magnitude lower than σ_e for both P3HT-PEO(9-2) and P3HT-PEO(6-2). It was shown in Chapter 4, that the high values of σ_e in P3HT-PEO(9-2) and P3HT-PEO(6-2) is due to partitioning of salt into

the P3HT microphase. In contrast, the salt is located exclusively in the PEO microphase in the case of P3HT-PEO(5-4). It thus appears that the chemical potential of LiTFSI in PEO is a function of the PEO block molecular weight. We propose that the higher chemical potential of LiTFSI for P3HT-PEO block copolymers with PEO molecular weight of 2 kg/mol drives the LiTFSI into the P3HT rich microphase. In the two-terminal conductivity cell, the LiTFSI chemical potential can only be decreased by partitioning into the P3HT microphase. In the three-terminal electrochemical cell, however, the LiTFSI chemical potential can be decreased by partitioning into the PS-PEO electrolyte layer where the PEO molecular weight is 67.6 kg/mol. We thus conclude that the electronic conductivities of all three P3HT-PEO block copolymer measured in the three-terminal electrochemical cell and that of P3HT-PEO(5-4) measured in the cell with two-terminal conductivity cell correspond to a pure P3HT microphase with no added LiTFSI. All of the results obtained from unoxidized P3HT-PEO block copolymers is consistent with the notion that LiTFSI chemical potential increases with decreasing PEO block molecular weight. The interfacial area per unit volume between ionically conducting and non-ionically conducting microdomains (either P3HT or PS) increases with decreasing PEO block molecular weight. This is one potential reason for the dependence of LiTFSI chemical potential on PEO block molecular weight. Lastly, it is evident in Figure 5.6 that the electronic conductivities of electrochemically oxidized of P3HT-PEO block copolymers are weak functions of P3HT volume fraction (ϕ_{HT}) where increasing r_{ox} from 0 to 0.01 results a 1000 fold in $\sigma_{e,ox}$. Further increase in r_{ox} from 0.01 to 0.10 results in 100 fold increase in $\sigma_{e,ox}$.

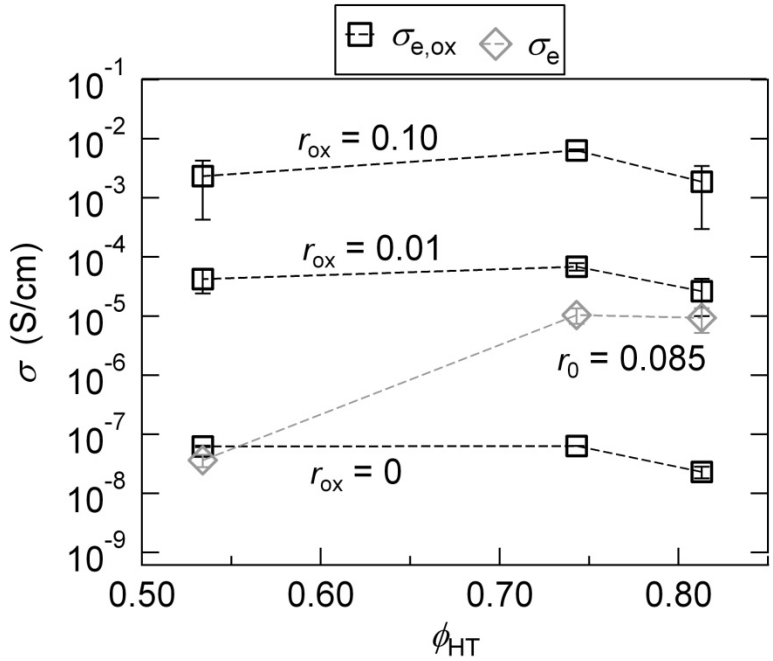

Figure 5.6. Electronic conductivity of the oxidized P3HT-PEO block copolymers ($\sigma_{e,ox}$) at 90 °C as a function the P3HT volume fraction, (ϕ_{HT}) for r_{ox} values of 0, 0.01, and 0.10. The ϕ_{HT} values for the three block copolymer are given in Table 5.1. The diamond markers correspond to the electronic conductivity of the P3HT-PEO block copolymers when only considering the chemical mixing of LiTFSI at r_0 = 0.085 and determined using a two-terminal conductivity cell. The dashed lines are guides for the eye.

Figure 5.7 shows conductivity data obtained in the three-terminal cells as the P3HT-PEO block copolymers are cycled between oxidized and reduced states. A cycle consisted of oxidation in two steps, from r_{ox} = 0 to r_{ox} = 0.01 and from r_{ox} = 0.01 to r_{ox} = 0.10, using the galvanostatic oxidation protocol described above. Each step took about one hour to execute. In the reduction step, the electrons were added to the P3HT-containing electrode until the voltage cutoff of 2.5 V was reached and the cell was allowed rest until a stable value of conductivity was obtained. Full reduction of the P3HT chains back to the neutral state took several such steps and typically required three days. In the oxidation step, the TFSI anion diffuses through the PEO microphase into the P3HT microphase. In the reduction step, the TFSI anion diffuses through the P3HT microphase into the PEO microphase. Our experiments suggest that the diffusion of TFSI anion through P3HT is much slower than through PEO. It is evident in Figure 5.7 that the dependence of $\sigma_{e,ox}$ of P3HT-PEO(9-2) and P3HT-PEO(6-2) on r_{ox} is independent of cycle number. In the case of P3HT-PEO(5-4), $\sigma_{e,ox}$ increases with each cycle at both r_{ox} values of 0.01 and 0.10. The largest increase occurs between cycle 2 and 3. The data obtained in cycles 4 and 5 are almost within experimental error but shows signs of stabilizing after subsequent cycling. Even though $\sigma_{e,ox}$ at r_{ox} = 0.01 and 0.10 generally increases with cycle number, the baseline conductivity obtained at r_{ox} = 0 is within experimental error in all cases.

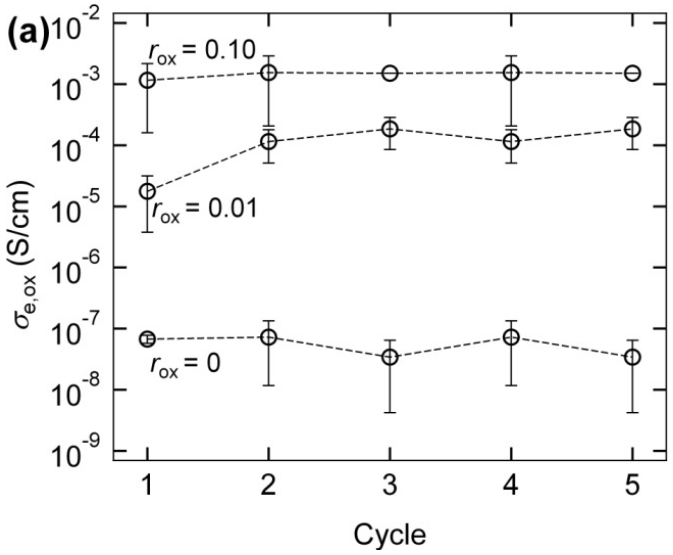

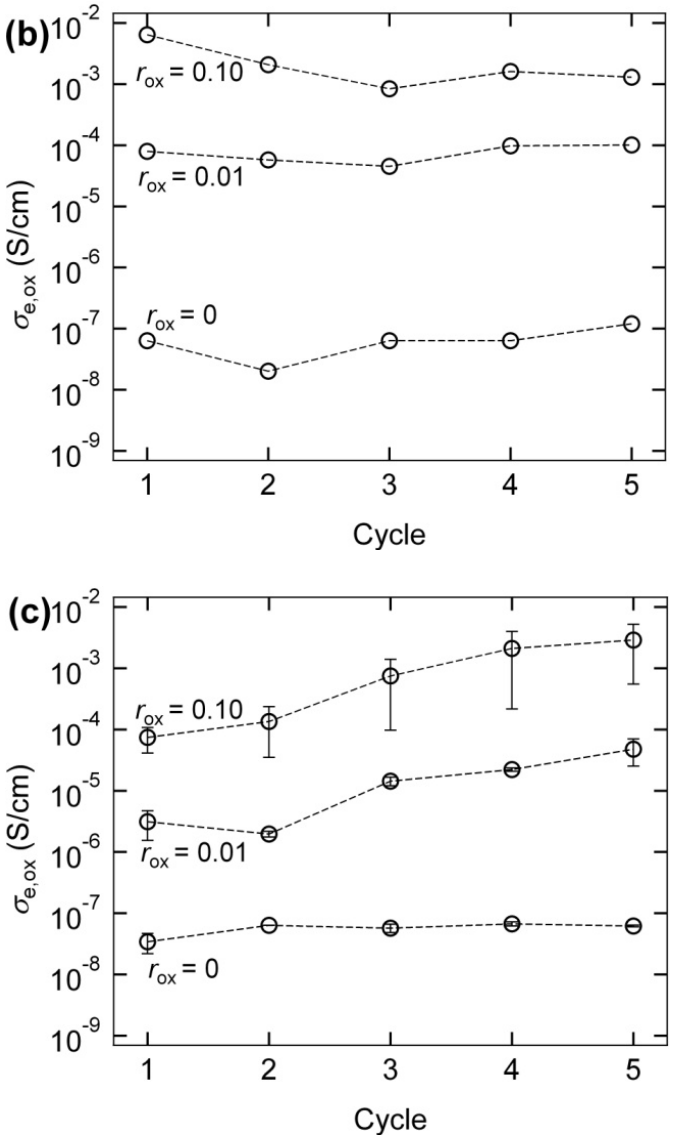

Figure 5.7. Electronic conductivity of the oxidized (a) P3HT-PEO(9-2), (b) P3HT-PEO(6-2), and (c) P3HT-PEO(5-4) block copolymers at 90 °C for r_{ox} values of 0. 0.01, and 0.10 for five oxidation/reduction cycles. A cycle consisted of oxidation from r_{ox} = 0 to r_{ox} = 0.10 and then reduction back to neutral state of r_{ox} = 0, which corresponds to the start of the next cycle.

Small angle X-ray scattering (SAXS) experiments were performed on the oxidized samples at r_{ox} = 0.10 after the fifth cycle. Figure 5.8a shows the SAXS intensity, *I*, *versus* magnitude of the scattering vector, *q*, of P3HT-PEO(5-4) at r_{ox} = 0 and 0.10. The SAXS profile of P3HT-PEO(5-4) at r_{ox} = 0 shows a primary peak at $q = q^* = 0.31$ nm^{-1} and a higher order peak at $2q^*$, indicating the presence of a lamellar structure with a domain spacing, d = 20.3 nm ($d = 2\pi/q^*$). At r_{ox} = 0.10, the SAXS profile of P3HT-PEO(5-4) shows only a primary peak at $q^* = 0.28$ nm^{-1} corresponding to a domain of d = 22.4 nm. It is clear from the scattering profile that oxidation of P3HT results in the reduction of long range order as indicated by the loss of the second order peak. The transformation of P3HT-PEO(5-4) to a poorly ordered morphology may be one of the reasons why $\sigma_{e,ox}$ increases with cycle number. It has been shown in PS-PEO block copolymer electrolytes that decreasing long

range order increases ionic conductivity in bulk samples.[168] The SAXS profile of P3HT-PEO(9-2) at r_{ox} = 0 shows a broad peak at q^* = 0.31 nm^{-1} corresponding d = 20.3 nm (Figure 5.8b). Subtle shoulders are seen at higher values of q. These are signatures of the nanofibrillar morphology typically seen with P3HT-containing block copolymers. At r_{ox} = 0.10, the SAXS profile of P3HT-PEO(9-2) also shows the nanofibrillar morphology with a broad peak at q^* = 0.29 nm^{-1} corresponding to d = 22 nm. Unlike P3HT-PEO(5-4), no significant change in morphology is seen upon oxidation of P3HT-PEO(9-2). This may be the reason for the lack of dependence of $\sigma_{e,ox}$ on cycle number. In both Figures 5.8a and 5.8b, we see that d increases with oxidation [d increases 10% in P3HT-PEO(5-4) and 6% for P3HT-PEO(9-2)]. The transformation of the P3HT backbone from the benzenoid structure to the quinoid structure results in an increase the persistence length of the polymer.[169] We propose the observed increase in d upon oxidation is due to this effect.

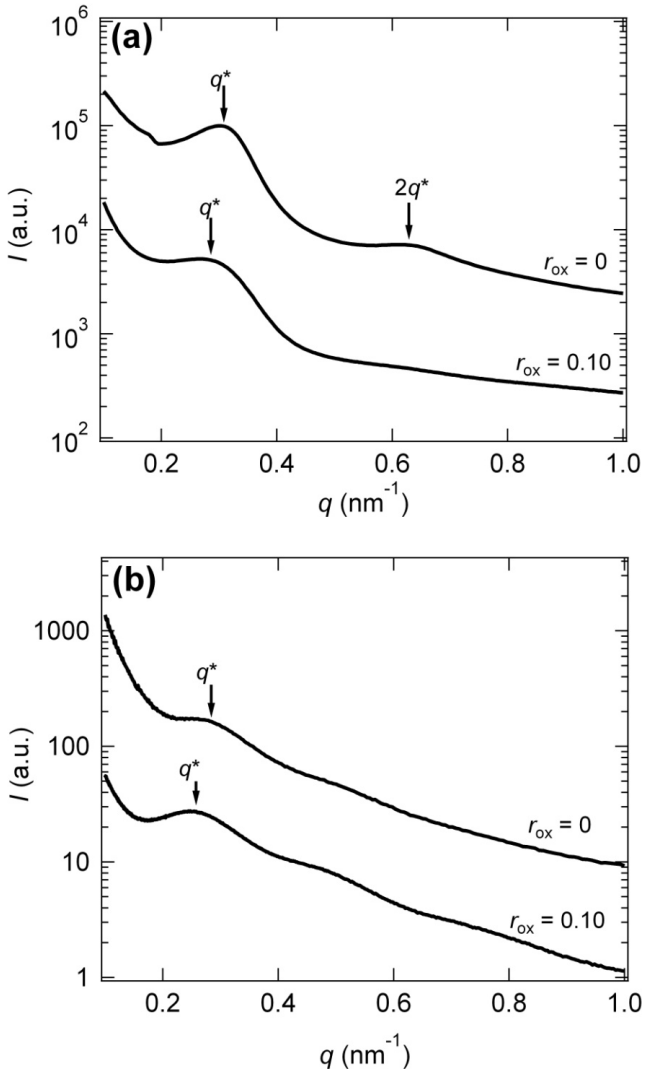

Figure 5.8. (a) SAXS profile of P3HT-PEO(5-4) at 90 °C for r_{ox} = 0 and 0.01 indicating the presence of microphase separation. A lamellar morphology is seen at r_{ox} = 0, while the there is a decrease in long-range order after oxidation to r_{ox} = 0.10. (b) SAXS profile of P3HT-PEO(9-2) at 90 °C for r_{ox} = 0 and 0.01 indicates a microphase separated structure.

The important parameters that described the effects of electrochemical oxidation on electronic conductivity of P3HT-PEO block copolymers are $\sigma_{e,ox}$, r_{ox}, and E_{ox}. The relationships between these parameters are shown in Figure 5.9. Figure 5.9a shows $\sigma_{e,ox}$ as function of r_{ox} for the three P3HT-PEO block copolymers. The dependence of $\sigma_{e,ox}$ on r_{ox} is similar for all three block copolymers. The data appear to fall into two regimes. The first regime encompasses low oxidation levels and it is found that $\sigma_{e,ox}$ increase by approximately three orders of magnitude when r_{ox} increases from 0 to 0.005. In the second regime, further increase of r_{ox} from 0.005 to about 0.10 results in a more modest increase in $\sigma_{e,ox}$ with some evidence of saturation at $\sigma_{e,ox}$ of 10^{-2} S/cm at high r_{ox} values. The trends seen in Figure 5.9a are consistent with previously reported behavior of chemically oxidized conjugated polymers.[1] The highest r_{ox} values attainable, 0.10, 0.125, and 0.150 for P3HT-PEO(9-2), P3HT-PEO(6-2), and P3HT-PEO(5-4), respectively, increase with decreasing molecular weight of the P3HT block. Chen et al. report r_{ox} values as high as 0.30 for poly(3-butylthiophene) immersed in $LiPF_6$-containing liquid electrolyte and corresponding bulk electronic conductivities as high as 0.1 S/cm. However, Ciprelli et al. found considerably lower values of r_{ox} when poly(3-octylthiophene) was chemically doped with a salt containing the TFSI anion.[170] In Figure 5.9b, we show the relationship between r_{ox} and E_{ox}, which has a power law relationship (the solid curves are power law fits to the data points). Even though each block copolymer has a different highest attainable r_{ox}, the corresponding highest attainable E_{ox} is about 3.6 V in all cases. In Figure 5.9c, we show the relationship between E_{ox} and $\sigma_{e,ox}$. It is clear that $\log(\sigma_{e,ox})$ increases linearly with E_{ox} in the potential range of the measurements.

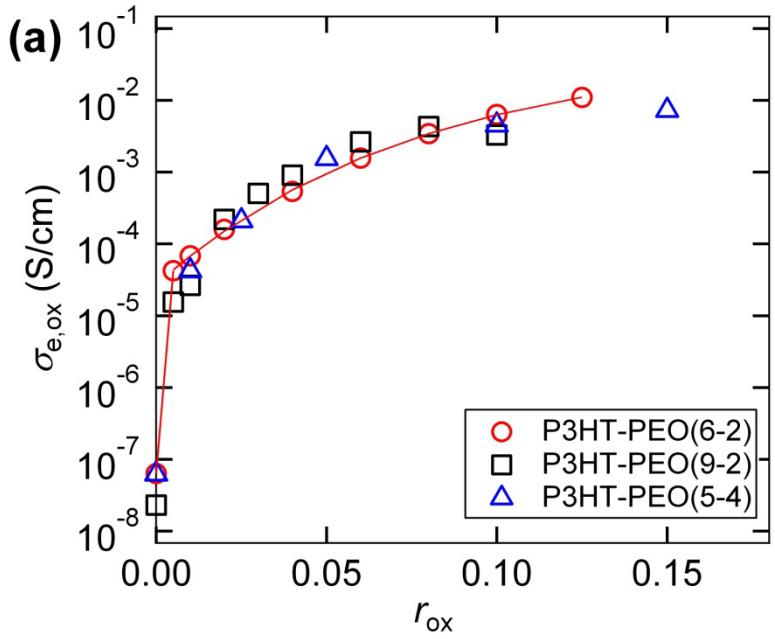

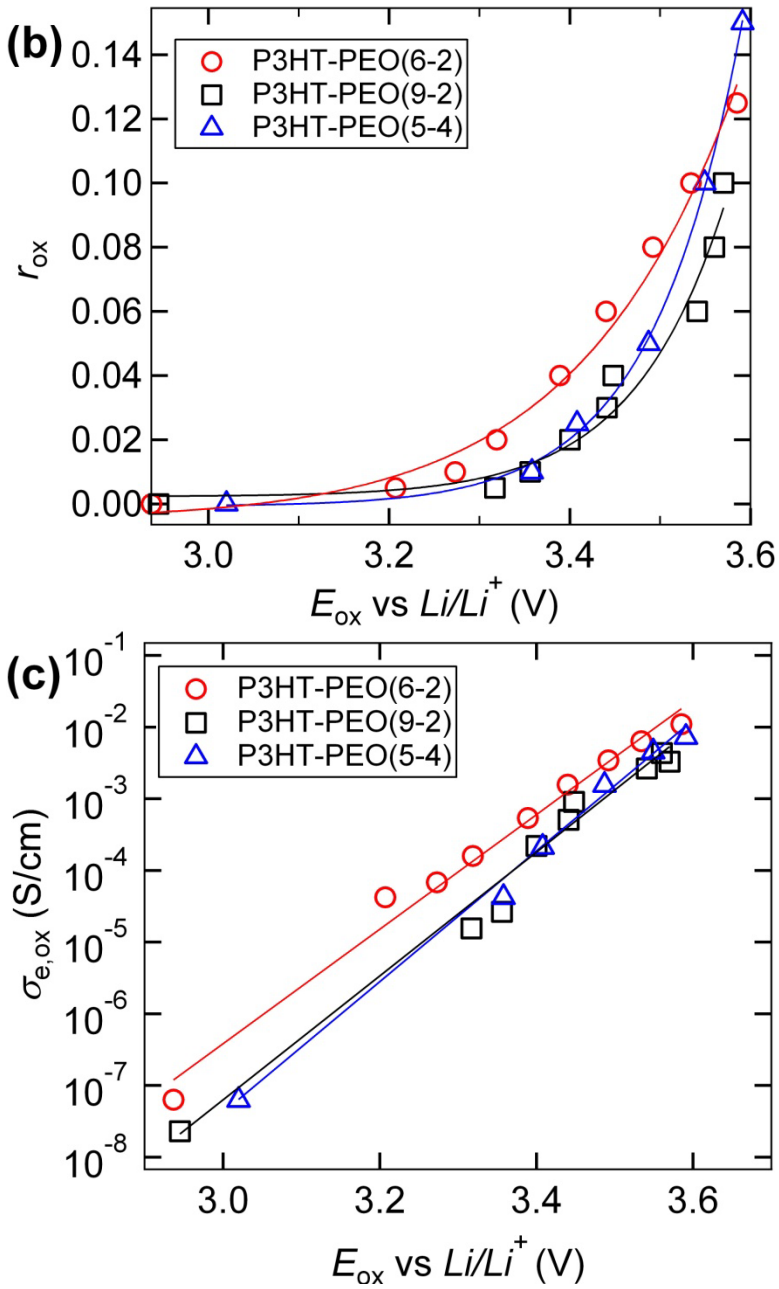

Figure 5.9. (a) Electronic conductivity ($\sigma_{e,ox}$) of the oxidized P3HT-PEO block copolymers as function of oxidation level (r_{ox}). The solid line correspond to a line fit between r = 0 and 0.005. The solid curve corresponds to a fit using $\log(\sigma_{e,ox}) = a - b(10^{c*rox/d})$ from r_{ox} = 0.005 to 0.125, where a = -1.32, b = 3.24, c = 1120, and d = 86.2. Fit is only given for P3HT-PEO(6-2) for clarity. (b) The relationship between r_{ox} and E_{ox} for the P3HT-PEO block copolymers. Open circles are the experimental data and the solids curves are power law fits. Fit parameters using the equation $r_{ox} = a + b(E_{ox})^c$: a = -4.97 x10^{-3}, b = 8.08 x 10^{-13}, and c = 20.6 for P3HT-PEO(6-2), a = 2.28 x 10^{-3}, b = 3.25 x 10^{-21}, and c = 35.2 for P3HT-PEO(9-2), and a = -7.54 x 10^{-4}, b = 1.31 x 10^{-21}, and c = 36.1 for P3HT-PEO(5-4). (c) Electronic conductivity of the oxidized P3HT-PEO block copolymers as function of cell potential (E_{ox} *vs* Li/Li^+). Open circles are the experimental data and the solids lines are linear (log-scale) fits. Fit parameters using the equation $\log(\sigma_{e,ox}) = a + b(E_{ox})$: a = -30.4 and b = 7.99 for P3HT-PEO(6-2), a = -33.1 and b = 8.63 for P3HT-PEO(9-2), and a = -34.7 and b = 9.11 for P3HT-PEO(5-4). All conductivity data are at 90 °C.

Figure 5.10 shows the hole mobility (μ_{ox}) of electrochemically oxidized P3HT-PEO block copolymer as a function of r_{ox}. The mobilities were calculated from the relation $\mu_{ox} = \sigma_{e,ox}/ne$, where n is the charge carrier density, and e is the elementary charge. The value of n is calculated from r_{ox}; $n = r_{ox}N_{av}\rho_{P3HT}/M_0$, where N_{av} is Avogrado's number, ρ_{P3HT} is the density of P3HT, and M_0 is molar mass of 3-hexylthiophene repeat unit. Note that both $\sigma_{e,ox}$ and n are function of electrochemical potential of the polymer (Figure 5.9). The μ_{ox} vs r_{ox} data in Figure 5.10 appear to fall two regimes. For r_{ox} values less than 0.02, μ_{ox} is a weak function of r_{ox}. Above $r_{ox} = 0.02$, μ_{ox} increases linearly, nearly one order of magnitude, as r_{ox} is increased to about 0.10. In this regime, hole mobility is independent of block copolymer composition or the chain length of P3HT block. The data in Figure 5.10 are qualitatively similar to those obtained from electrochemically doped P3HT homopolymer in presence of a liquid electrolyte.[43, 171, 172] Arkhipov et al. explained the observed trend in mobility assuming a transport model that account for coulombic interactions between the holes and counterions. An important parameter in the model is the reciprocal localization radius (γ) which was varied to obtain agreement between theory and experiment. At low r_{ox} values, the holes generated are trapped by the attractive Coulomb potentials of the TFSI anion (Coulomb traps). As a result, the mobility of holes is suppressed. The several orders of magnitude increase in $\sigma_{e,ox}$ (Figure 5.9a) at low r_{ox} is entirely from the increase in charge carrier density. As r_{ox} increases, the distance between the holes (and TFSI anions) decreases, which results in the overlap of the Coulomb trap potential energy wells. This reduces the activation barrier for hole transport and enhances mobility. Remarkably, the data in Figure 5.10 are in quantitative agreement Arkhipov et al. with $\gamma = 3$ nm^{-1},i.e. μ_{ox} increases from 10^{-5} to 10^{-4} cm^{2}V^{-1}s^{-1} as r_{ox} is increased by a factor of 10 (Figure 4 in ref. 172). The only difference between our data and the model is that in the model the linear regime starts at $r_{ox} \approx 0.1$ while in our experiments this regime at $r_{ox} \approx 0.01$.

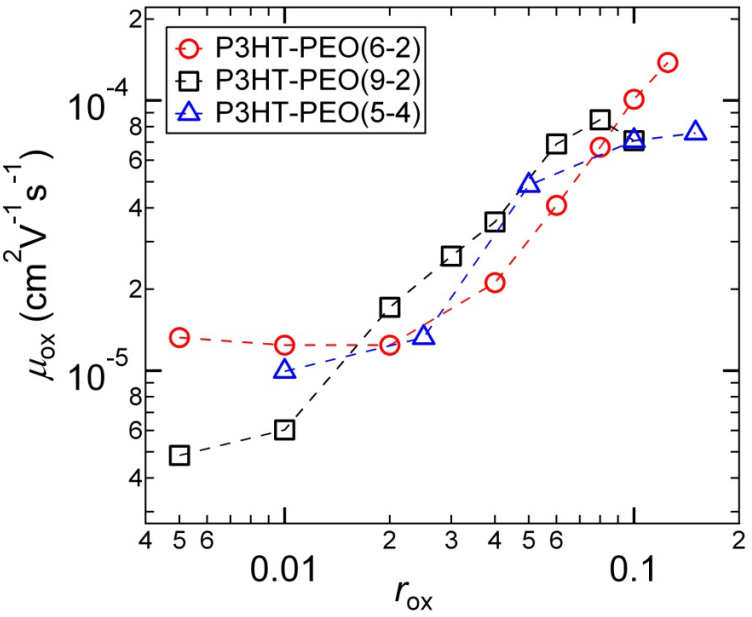

Figure 5.10. Hole mobility (μ_{ox}) of electrochemically oxidized P3HT-PEO block copolymers as function of oxidation level (r_{ox}). The mobilities were calculated from the relation $\mu_{ox} = \sigma_{e,ox}/ne$, where n (related to r_{ox}) is the charge carrier density (cm^{-3}), and e is the elementary charge. The dashed lines are guides for the eye.

Figure 5.11a shows the schematic of a battery with a lithium metal negative electrode and a $LiFePO_4$ positive electrode. The $LiFePO_4$ particles are dispersed in a P3HT-PEO(6-2)/LiTFSI mixture. Separating the two electrodes is a PS-PEO block copolymer electrolyte layer with LiTFSI at $r_0 = 0.085$. Figure 5.11b shows an SEM image of the film obtained from the $LiFePO_4$/P3HT-PEO(6-2)/LiTFSI mixture. $LiFePO_4$ particles appear as bright spots and the polymer/salt mixture appears as a dark matrix. This film is remarkably simple when compared to a traditional lithium ion positive electrode, which contains pores for ionic conduction, conductive carbon additives for electronic conduction, and an inert polymer binder to hold the structure in place, in addition to the active material. In our system, the active material is dispersed in a single polymer that functions simultaneously as the conductor of lithium ions and electronic charge, as well as the binder material in the electrode. The average specific capacities of ten batteries obtained during the first ten cycles are shown in Figure 5.11c. The batteries show a specific capacity that approaches the theoretical value of $LiFePO_4$ (170 mAh/g) with relatively little capacity fade. This provides further evidence that the P3HT-PEO block copolymer delivers both ions and electronic charge to the active centers, thus allowing the batteries to cycle efficiently. It is important to note that P3HT is also redox-active and can contribute to the capacity of the battery where the theoretical specific capacity for P3HT is 161 mAh/g. However, as we will show later, P3HT only contributes a very small fraction to the overall capacity of the battery.

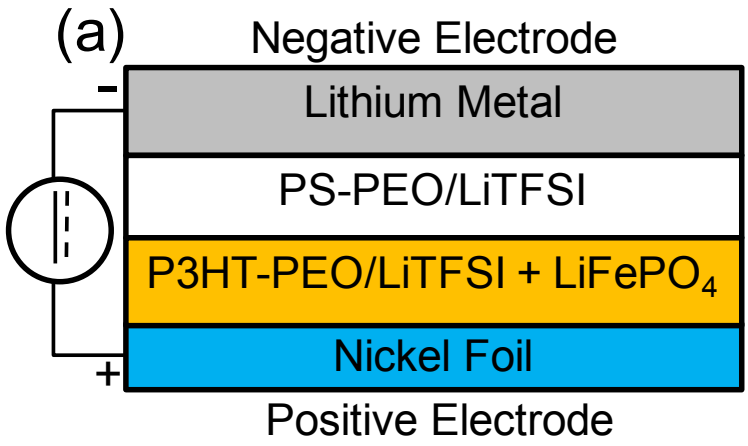

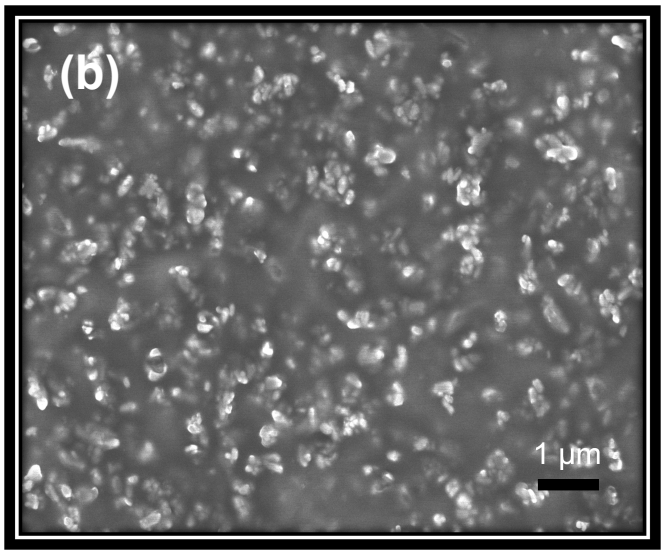

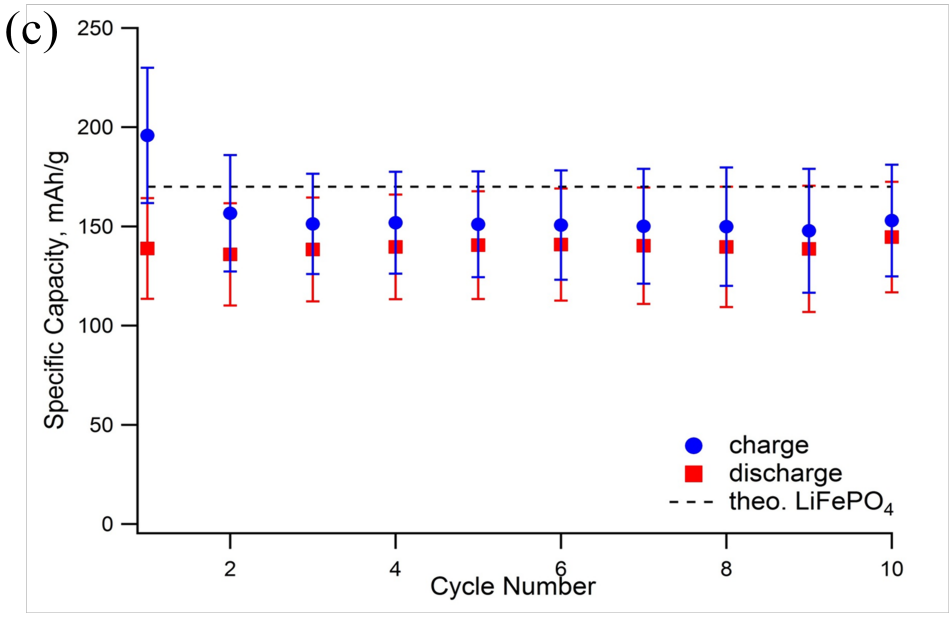

Figure 5.11. **(a)** Schematic of a battery cell with a positive electrode comprising of $LiFePO_4$, LiTFSI, and P3HT-PEO binder. The negative electrode is pure lithium metal, which also serves as the reference electrode. In between the positive and negative electrode is a PS-PEO/LiTFSI electrolyte layer. **(b)** SEM image of the positive electrode composed of P3HT-PEO(6-2)/LiTFSI and $LiFePO_4$. **(c)** Average specific capacity (mAh/g) for 10 cells as a function of cycle number of $LiFePO_4$. The dashed line corresponds to the theoretical specific capacity of $LiFePO_4$ (170 mAh/g).

We focus on a single charge/discharge cycle to elucidate the changes in the electronic conductivity and oxidation level of P3HT during a battery cycle as shown in Figure 5.12a. The voltage of the battery (E_{we} vs. Li/Li^+) is initially at its equilibrium OCV of 3.41 V. The battery is then charged at a constant i of 0.02 mA/cm^2 until E_{we} reaches 3.8 V. E_{we} is held at 3.8 V until i decreased to 10% of the original value, which completes the charging step. After a rest step of 60 minutes, the battery is discharged at a constant i of -0.02 mA/cm^2 until E_{we} reaches 2.5 V. After another rest step, E_{we} increases until it returns to the equilibrium OCV value of 3.41 V. This completes the charge/discharge cycle. Note that the E_{we} values found in the battery (Figure 5.12a) overlap with the range of E_{ox} values given in Figure 5.9c. Interestingly, the voltage window where P3HT is electrochemically active is within the voltage range of the battery charge/discharge cycle. The reversible redox reactions occurring in the battery are

$$xLiFePO_4 \underset{\text{discharge}}{\overset{\text{charge}}{\rightleftharpoons}} xFePO_4 + xe^- + xLi^+ \tag{5.2}$$

$$y P3HT \underset{\text{discharge}}{\overset{\text{charge}}{\rightleftharpoons}} y P3HT^+ + ye^- \tag{5.3}$$

$$(x+y)Li^+ + (x+y)e^- \underset{\text{discharge}}{\overset{\text{charge}}{\rightleftharpoons}} (x+y)Li \tag{5.4}$$

The forward reaction corresponds to the charging step while the reverse reaction corresponds to discharging step. Reactions 5.2 and 5.3 occur in the positive electrode while reaction 5.4 occurs in the negative electrode. In Figure 5.12b, we show the time dependence of r_{ox} during the charge/discharge cycle. This curve was calculated from the power law fit through P3HT-PEO(6-2) data in Figure 5.9b. During the charging step, r_{ox} was assumed to follow the power law until the maximum r_{ox} value was reached. During this time, we assumed that both $LiFePO_4$ and P3HT are oxidized. In the remainder of the charging the step, we assume that all of the oxidation occurs in the $LiFePO_4$ particles. We assume the r_{ox} remains constant during the rest step and that follows the power law in the subsequent discharging and rest steps. At a maximum r_{ox} of 0.125, P3HT is only contributes about 7% to the total capacity of the battery.

In Figure 5.12c, we show the time dependence of $\sigma_{e,ox}$ during the charge/discharge cycle obtained using the fit through the P3HT-PEO(6-2) data shown in Figure 5.9c. It is evident that the conductivity of our binder is relatively high, in the 10^{-3} to 10^{-2} S/cm range during charging. This value is significantly higher than the ionic conductivity of the P3HT-PEO(6-2)/LiTFSI mixture (10^{-4} S/cm) reported in Chapter 4. This is important for enabling the redox reactions 1 to 3 because they involve equal moles of lithium ions and electronic charges. It is, perhaps, not surprising that high electronic conductivity is obtained during charging because the P3HT chains are being oxidized during this step. During most of the discharge step, electronic conductivity is above 10^{-4} S/cm. This may seem surprising because P3HT is being reduced during this step. Electronic conductivity during the discharge step is enabled entirely due to the potential of 3.3 V imposed on the positive

electrode by the $FePO_4$ particles. As the discharge step approaches completion and E_{we} decreases to 2.5 V (Figure 5.12b), $\sigma_{e,ox}$ plummets to below 10^{-7} S/cm. In other words, our "conductive" binder is essentially an electronic insulator towards the end of the discharge cycle. This provides a unique route for overdischarge protection as the battery has been essentially "shutoff" to further discharge. After the discharge cycle, the battery returns back to equilibrium OCV value of 3.41 V where $\sigma_{e,ox} = 1 \times 10^{-3}$ S/cm indicating the binder returns to the electronically conducting state.

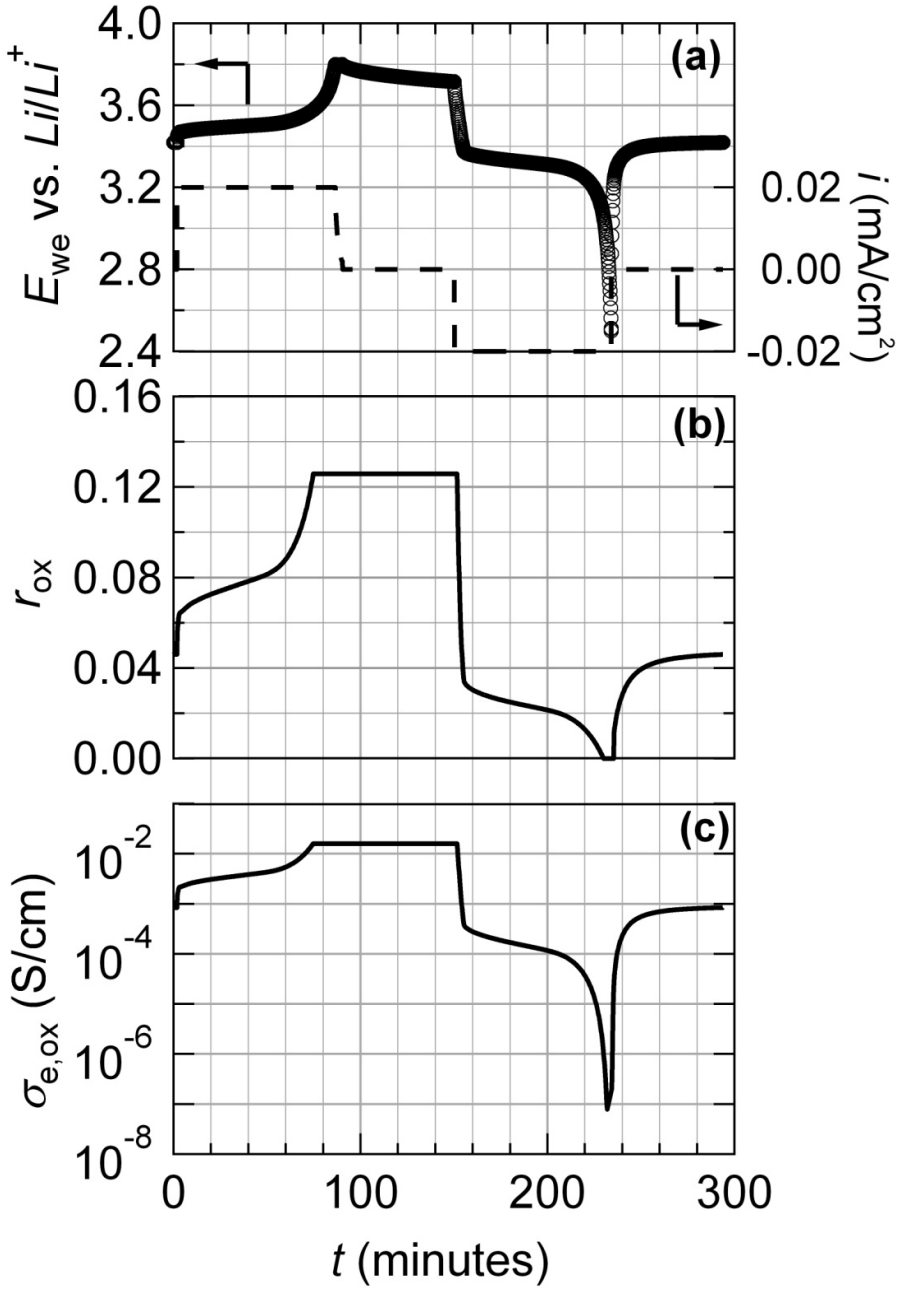

Figure 5.12. (a) Cell potential (E_{we} *vs* Li/Li^+) vs. time (t) curve corresponding to a characteristic charge/discharge profile for a battery cell composed of a lithium anode, solid polymer electrolyte, and a

$LiFePO_4$ positive electrode with P3HT-PEO(6-2) conductive binder. (b) Predicted oxidization level (r_{ox}) for the charge/discharge profile using the relationship between E_{ox} and r_{ox} given Figure 5.9b. (c) Predicted oxidized electronic conductivity ($\sigma_{e,ox}$) for the charge/discharge profile using the relationship between E_{ox} and $\sigma_{e,ox}$ given Figure 5.9c.

It is important to have overdischarge and overcharge protection in a battery in order to improve the safety and cycle life of the battery. In a conventional battery, overdischarge and overcharge protection is accomplished using external circuitry. Unfortunately, the use of external circuitry adds significant weight, adds to the cost, and complicates battery pack design. Therefore, it is advantageous to incorporate the overdischarge or overcharge protection capabilities within the chemistry of the battery cell, thus simplifying the battery pack design and reducing the cost. In some experimental battery cells, redox shuttles are used to enable overcharge and overdischarge protection within a battery cell.[173] In an interesting experiment, Chen *et al*. lined the pores of a conventional battery separator with P3BT. Under the conditions where the cells were fully charged, the P3BT lining became electronically conducting and the additional electrons were directly shuttled from the negative to the positive electrode.[163, 164] The charging process is thus interrupted. Alternatively, incorporating a semiconducting binder in one of the electrodes (as we do in this study) provides a radically new approach for enabling and overdischarge and overcharge protection. In principle, a semiconducting binder in the positive electrode could provide overdischarge protection, as shown in this study, while a semiconducting binder in the negative electrode could provide overcharge protection.

5.4 Conclusions

We have characterized the electronic charge transport properties of electrochemically doped P3HT-PEO block copolymers used as conductive binder material for a lithium battery positive electrode. We use a novel three-terminal electrochemical cell that enables simultaneous conductivity measurements and control over electrochemical doping of P3HT. The electronic conductivity ($\sigma_{e,ox}$) of the P3HT-PEO block copolymers are measured as a function of oxidation level, r_{ox}, and oxidation voltage, E_{ox}. At low r_{ox} values below 0.01, $\sigma_{e,ox}$ increases from 10^{-8} S/cm to nearly 10^{-4} S/cm. At r_{ox} values near the highest attainable oxidation levels, $\sigma_{e,ox}$ approaches 10^{-2} S/cm. We further extend our analysis to a charge/discharge cycle of a lithium battery that contains a positive electrode with $LiFePO_4$ active material and P3HT-PEO(6-2) conductive binder. Importantly, P3HT is electroactive in the potential window of a charge/discharge cycle, which means we have two redox reactions occurring in the positive electrode involving P3HT and $LiFePO_4$ (reactions 5.2 and 5.3). We assume that the $LiFePO_4$ redox reaction controls the cell potential of the battery, which in turn dictates the $\sigma_{e,ox}$ of the P3HT-PEO block copolymer. At OCV of the battery, the binder is at an electronically conducting state ($\sigma_{e,ox} = 10^{-3}$ S/cm), and $\sigma_{e,ox}$ increases to 10^{-2} S/cm during the charging step. This range is significantly higher than the ionic conductivity of the P3HT-PEO block copolymer binder (10^{-4} S/cm). This is important for enabling the redox reactions as they involve equal moles of lithium ions and electronic charges (reactions 5.2 and 5.3). $\sigma_{e,ox}$ is above 10^{-4} S/cm for majority of the discharge cycle allowing for

successful extraction of discharge capacity from the battery. However, at the tail end of the discharge cycle, $\sigma_{e,ox}$ decreases sharply to 10^{-7} S/cm; in this state the P3HT-PEO block copolymer binder is essentially an electronic insulator. This observation shows that the use of semiconducting polymer like P3HT as a conductive binder in a positive electrode provides an unprecedented route for overdischarge protection in batteries.

Chapter 6 - Summary

The goal of this project was to synthesize and characterize the structural and charge transport properties of poly(3-alkylthiophene)-*b*-poly(ethylene oxide) P3AT-*b*-PEO copolymers. These block copolymers are used as conductive binder material for a lithium battery electrode where it provides charge transport pathways for both electronic charges (P3HT) and Li^+ ions (PEO) on the nanometer length scale. This electrode design is remarkably simple when compared to a traditional lithium ion positive electrode, which contains pores for ionic conduction, conductive carbon additives for electronic conduction, and an inert polymer binder to hold the structure in place, in addition to the active material (*e.g.* $LiFePO_4$).

Poly(3-hexylthiophene)-*b*-poly(ethylene oxide) (P3HT-PEO) and poly(3-ethylhexylthiophene)-b-poly(ethylene oxide) (P3EHT-PEO) copolymers were synthesized using a combination of Grignard metathesis (GRIM) polymerization and 1,3-dipolar cycloaddition "click" reaction. To obtain basic characteristics, the synthesized polymer were characterized using gel permeation chromatography (GPC), ^{1}H-NMR spectroscopy, matrix assisted laser desorption ionization – time of flight (MALDT-TOF), differential scanning calorimetery (DSC), and UV-VIS spectroscopy.

The morphology of P3HT-*b*-PEO copolymers, where the P3HT block is the major component, is dominated by nanofibrils. In contrast, the nearly symmetric P3HT-*b*-PEO copolymers self-assemble into a lamellar phase. In addition, we show that P3EHT-*b*-PEO chains self-assemble to produce traditional nanoscale morphologies such as lamellae and gyroid in the melt-state. The segregation strength between the two blocks is controlled through the addition of lithium bis(trifluromethanesulfonyl) imide (LiTFSI). Our approach enables estimation of the "effective" Flory-Huggins interaction parameter, χ_{eff}, using the random phase approximation (RPA). The χ_{eff} trends with salt concentration suggest that the TFSI anion preferentially segregates into the P3EHT phase while Li^+ remains in the PEO phase. For the salt-free sample, the gyroid morphology, obtained in the melt-state, is transformed into lamellae when the P3EHT block is crystallized. This is due to the "breaking out" of the crystalline phase. At high salt concentrations, P3EHT-*b*-PEO has a lamellar morphology in both melt and crystalline states (confined crystallization).

We presented the first reported attempt to study the relationship between morphology and electronic/ionic charge transport of P3HT-*b*-PEO/LiTFSI mixtures. Using ac impedance spectroscopy, we show that P3HT-*b*-PEO/LiTFSI mixtures can conduct electronic and ionic charges simultaneously. At 90 °C, the electronic conductivity of P3HT-*b*-PEO/LiTFSI mixtures ranged from 10^{-8} to 10^{-5} S/cm depending on the volume fraction of P3HT. The decoupled ionic conductivity is around $\sim 10^{-4}$ S/cm. It was shown that LiTFSI partitions between P3HT and PEO microphases. In particular, LiTFSI only partitions between the microphases when the PEO block molecular weight is 2 kg/mol while we observe no partitioning when the PEO block molecular weight of 4.2 kg/mol. It thus appears that the chemical potential of LiTFSI in PEO is a function of the PEO block molecular weight. We propose that the higher chemical potential of LiTFSI for P3HT-*b*-PEO copolymers with PEO molecular weight of 2 kg/mol drives the LiTFSI into the P3HT rich microphase.

The electronic conductivity can be further increased by electrochemically chemically doping the P3HT chains with LiTFSI. Electrochemical doping provides a unique avenue for

designing the next generation of electrodes because it enables the possibility of turning redox reactions on and off reversibly through the control of applied potentials. This is in stark contrast to the traditional carbon additives used to conduct electrons in current battery and fuel cell electrodes which have a fixed electronic conductivity. Therefore, we quantified the electronic conductivity P3HT-*b*-PEO copolymers electrochemically oxidized with LiTFSI. We use a novel solid-state three-terminal electrochemical cell that enables simultaneous conductivity measurements and control over electrochemical doping of P3HT. At low oxidation levels, the electronic conductivity increases from 10^{-8} S/cm to 10^{-4} S/cm. At high oxidation levels, the electronic conductivity approaches 10^{-2} S/cm. These values match or exceed the ionic conductivity, which is important for enabling redox reactions in a battery as they involve equal moles of lithium ions and electronic charges.

A lithium metal battery was assembled where the positive electrode consisted of P3HT-*b*-PEO conductive binder and $LiFePO_4$ active material. We were able to cycle batteries and obtain capacities approaching the theoretical limit of $LiFePO_4$. Importantly, P3HT is electroactive within the voltage window of a charge/discharge cycle. The electronic conductivity of the P3HT-*b*-PEO copolymer binder is in the 10^{-4} to 10^{-2} S/cm range over most of the potential window of the charge/discharge cycle. This allows for efficient electronic conduction needed for the successful cycling of the batteries. However, at the end of the discharge cycle, the electronic conductivity decreases sharply to 10^{-7} S/cm, which means the "conductive" binder is now electronically insulating. The ability of our conductive binder to switch between electronically conducting and insulating states in the positive electrode provides an unprecedented route for automatic overdischarge protection in batteries.

The results of my PhD research clearly show that choosing the correct conjugated polymer and inorganic active material combination is very important in successful battery cycling. Our results suggest that the inorganic active material dominates the cell voltage. Therefore, the conjugated polymer must be electrochemically active in the voltage window of the inorganic active material in order to have sufficient electronic conductivity. Meaning, electronic conductivity needs to match or exceed the ionic conductivity. This is particularly important during the discharge cycle. The above analysis provides a new framework for substantial future work on characterizing electronic and ionic conduction of block copolymers and its application to battery electrodes.

Chapter 7 - References

1. Chiang, C. K.; Gau, S. C.; Fincher, C. R.; Park, Y. W.; Macdiarmid, A. G.; Heeger, A. J. Polyacetylene, (Ch)X - N-Type and P-Type Doping and Compensation. *Appl Phys Lett* **1978**, *33*, 18-20.

2. Yan, H.; Chen, Z. H.; Zheng, Y.; Newman, C.; Quinn, J. R.; Dotz, F.; Kastler, M.; Facchetti, A. A High-Mobility Electron-Transporting Polymer for Printed Transistors. *Nature* **2009**, *457*, 679-U1.

3. Sirringhaus, H. Device Physics of Solution-Processed Organic Field-Effect Transistors. *Adv Mater* **2005**, *17*, 2411-2425.

4. Sun, Y. M.; Liu, Y. Q.; Zhu, D. B. Advances in Organic Field-Effect Transistors. *J Mater Chem* **2005**, *15*, 53-65.

5. Bao, Z. N. Designing Organic Materials for Thin Film Transistors. *Abstr Pap Am Chem S* **2004**, *228*, U215-U216.

6. Yu, G.; Gao, J.; Hummelen, J. C.; Wudl, F.; Heeger, A. J. Polymer Photovoltaic Cells - Enhanced Efficiencies Via a Network of Internal Donor-Acceptor Heterojunctions. *Science* **1995**, *270*, 1789-1791.

7. Yang, X.; Loos, J.; Veenstra, S.; Verhees, W.; Wienk, M.; Kroon, J.; Michels, M.; Janssen, R. Nanoscale Morphology of High-Performance Polymer Solar Cells. *Nano Lett.* **2005**, *5*, 579-583.

8. Novak, P.; Muller, K.; Santhanam, K. S. V.; Haas, O. Electrochemically Active Polymers for Rechargeable Batteries. *Chem. Rev.* **1997**, *97*, 207-281.

9. Mike, J. F.; Lutkenhaus, J. L. Recent Advances in Conjugated Polymer Energy Storage. *Journal of Polymer Science Part B: Polymer Physics* **2013**, n/a-n/a.

10. Morgado, J.; Cacialli, F.; Friend, R. H.; Chuah, B. S.; Rost, H.; Holmes, A. B. Light-Emitting Devices Based on a Poly(P-Phenylenevinylene) Statistical Copolymer with Oligo(Ethylene Oxide) Side Groups. *Macromolecules* **2001**, *34*, 3094-3099.

11. Heeger, A. J. Semiconducting and Metallic Polymers: The Fourth Generation of Polymeric Materials (Nobel Lecture). *Angew. Chem. Int. Ed.* **2001**, *40*, 2591-2611.

12. MacDiarmid, A. G. "Synthetic Metals": A Novel Role for Organic Polymers (Nobel Lecture). *Angew Chem Int Edit* **2001**, *40*, 2581-2590.

13. Shirakawa, H. The Discovery of Polyacetylene Film: The Dawning of an Era of Conducting Polymers (Nobel Lecture). *Angew. Chem. Int. Ed.* **2001**, *40*, 2575-2580.

14. Roncali, J. Conjugated Poly(Thiophenes) - Synthesis, Functionalization, and Applications. *Chem Rev* **1992**, *92*, 711-738.

15. Skotheim, T. A.; Reynolds, J. R. *Handbook of Conducting Polymers. Conjugated Polymers : Theory, Synthesis, Properties, and Characterization*. 3rd ed.; CRC Press: Boca Raton, 2007.

16. Ballauff, M. Stiff-Chain Polymers - Structure, Phase-Behavior, and Properties. *Angewandte Chemie-International Edition in English* **1989**, *28*, 253-267.

17. McCullough, R. D. The Chemistry of Conducting Polythiophenes. *Adv. Mater.* **1998**, *10*, 93-116.

18. Mao, H. Y.; Xu, B.; Holdcroft, S. Synthesis and Structure Property Relationships of Regioirregular Poly(3-Hexylthiophenes). *Macromolecules* **1993**, *26*, 1163-1169.

19. McCullough, R. D.; Tristramnagle, S.; Williams, S. P.; Lowe, R. D.; Jayaraman, M. Self-Orienting Head-to-Tail Poly(3-Alkylthiophenes) - New Insights on Structure-Property Relationships in Conducting Polymers. *J. Am. Chem. Soc.* **1993**, *115*, 4910-4911.

20. Elsenbaumer, R. L.; Jen, K. Y.; Oboodi, R. Processible and Environmentally Stable Conducting Polymers. *Synthetic Met* **1986**, *15*, 169-174.

21. Sato, M.; Tanaka, S.; Kaeriyama, K. Soluble Conducting Polythiophenes. *J Chem Soc Chem Comm* **1986**, 873-874.

22. McCullough, R. D.; Lowe, R. D. Enhanced Electrical-Conductivity in Regioselectively Synthesized Poly(3-Alkylthiophenes). *Journal of the Chemical Society-Chemical Communications* **1992**, 70-72.

23. Chen, T. A.; Rieke, R. D. The 1st Regioregular Head-to-Tail Poly(3-Hexylthiophene-2,5-Diyl) and a Regiorandom Isopolymer - Ni Vs Pd Catalysis of 2(5)-Bromo-5(2)-(Bromozincio)-3-Hexylthiophene Polymerization. *J Am Chem Soc* **1992**, *114*, 10087-10088.

24. Loewe, R. S.; Khersonsky, S. M.; McCullough, R. D. A Simple Method to Prepare Head-to-Tail Coupled, Regioregular Poly(3-Alkylthiophenes) Using Grignard Metathesis. *Adv. Mater.* **1999**, *11*, 250-+.

25. Jeffries-El, M.; Sauve, G.; McCullough, R. D. *In-Situ* End-Group Functionalization of Regioregular Poly(3-Alkylthiophene) Using the Grignard Metathesis Polymerization Method. *Adv. Mater.* **2004**, *16*, 1017-1019.

26. Osaka, I.; McCullough, R. D. Advances in Molecular Design and Synthesis of Regioregular Polythiophenes. *Acc. Chem. Res.* **2008**, *41*, 1202-1214.

27. McCullough, R.; Tristramnagle, S.; Williams, S.; Lowe, R.; Jayaraman, N. Self-Orienting Head-to-Tail Poly(3-Alkylthiophenese) - New Insights on Structure-Property Relationships in Conducting Polymers. *J. Am. Chem. Soc.* **1993**, *115*, 4910-4911.

28. Zhang, R.; Li, B.; Iovu, M. C.; Jeffries-El, M.; Sauve, G.; Cooper, J.; Jia, S. J.; Tristram-Nagle, S.; Smilgies, D. M.; Lambeth, D. N.*, et al.* Nanostructure Dependence of Field-Effect Mobility in Regioregular Poly(3-Hexylthiophene) Thin Film Field Effect Transistors. *J. Am. Chem. Soc.* **2006**, *128*, 3480-3481.

29. Tao, Y.; McCulloch, B.; Kim, S.; Segalman, R. A. The Relationship between Morphology and Performance of Donor-Acceptor Rod-Coil Block Copolymer Solar Cells. *Soft Matter* **2009**, *5*, 4219-4230.

30. Liu, J. S.; Sheina, E.; Kowalewski, T.; McCullough, R. D. Tuning the Electrical Conductivity and Self-Assembly of Regioregular Polythiophene by Block Copolymerization: Nanowire Morphologies in New Di- and Triblock Copolymers. *Angew. Chem. Int. Ed.* **2002**, *41*, 329-332.

31. Bondarev, D.; Zednik, J.; Sloufova, I.; Sharf, A.; Prochazka, M.; Pfleger, J.; Vohlidal, J. Synthesis and Properties of Cationic Polyelectrolyte with Regioregular Polyalkylthiophene Backbone and Ionic-Liquid Like Side Groups. *J. Polym. Sci., Part A: Polym. Chem.* **2010**, *48*, 3073-3081.

32. Chen, T. A.; Wu, X. M.; Rieke, R. D. Regiocontrolled Synthesis of Poly(3-Alkylthiophenes) Mediated by Rieke Zinc - Their Characterization and Solid-State Properties. *J. Am. Chem. Soc.* **1995**, *117*, 233-244.

33. Kuila, B. K.; Malik, S.; Batabyal, S. K.; Nandi, A. K. *In-Situ* Synthesis of Soluble Poly(3-Hexylthiophene)/Multiwalled Carbon Nanotube Composite: Morphology, Structure, and Conductivity. *Macromolecules* **2007**, *40*, 278-287.

34. Liu, C.; Oshima, K.; Shimomura, M.; Miyauchi, S. Anisotropic Conductivity-Temperature Characteristic of Solution-Cast Poly(3-Hexylthiophene) Films. *Synth. Met.* **2006**, *156*, 1362-1367.

35. Obrzut, J.; Page, K. A. Electrical Conductivity and Relaxation in Poly(3-Hexylthiophene). *Phys. Rev. B* **2009**, *80*.

36. Pal, S.; Roy, S.; Nandi, A. K. Temperature Variation of Dc Conductivity of Poly(3-Alkyl Thiophenes) and Their Cocrystals. *J. Phys. Chem. B* **2005**, *109*, 18332-18341.

37. Sze, S. M. *Semiconductor Devices, Physics and Technology*. 2nd ed.; Wiley: New York, 2002; p viii, 564 p.

38. Yim, K. H.; Whiting, G. L.; Murphy, C. E.; Halls, J. J. M.; Burroughes, J. H.; Friend, R. H.; Kim, J. S. Controlling Electrical Properties of Conjugated Polymers Via a Solution-Based P-Type Doping. *Adv Mater* **2008**, *20*, 3319-+.

39. Qiao, X. Y.; Wang, X. H.; Mo, Z. S. The Fecl3-Doped Poly(3-Alkyithiophenes) in Solid State. *Synth. Met.* **2001**, *122*, 449-454.

40. Xuan, Y.; Liu, X.; Desbief, S.; Leclere, P.; Fahlman, M.; Lazzaroni, R.; Berggren, M.; Cornil, J.; Emin, D.; Crispin, X. Thermoelectric Properties of Conducting Polymers: The Case of Poly(3-Hexylthiophene). *Phys Rev B* **2010**, *82*.

41. Chung, T. C.; Kaufman, J. H.; Heeger, A. J.; Wudl, F. Charge Storage in Doped Poly(Thiophene) - Opitcal and Electrochemical Studies. *Phys. Rev. B* **1984**, *30*, 702-710.

42. Chen, G. Y.; Thomas-Alyea, K. E.; Newman, J.; Richardson, T. J. Characterization of an Electroactive Polymer for Overcharge Protection in Secondary Lithium Batteries. *Electrochim. Acta* **2005**, *50*, 4666-4673.

43. Jiang, X.; Harima, Y.; Yamashita, K.; Tada, Y.; Ohshita, J.; Kunai, A. Doping-Induced Change of Carrier Mobilities in Poly(3-Hexylthiophene) Films with Different Stacking Structures. *Chem. Phys. Lett.* **2002**, *364*, 616-620.

44. Bredas, J. L.; Street, G. B. Polarons, Bipolarons, and Solitons in Conducting Polymers. *Acc. Chem. Res.* **1985**, *18*, 309-315.

45. Stafstrom, S.; Bredas, J. L. Evolution of the Electronic-Structure of Polyacetylene and Polythiophene as a Function of Doping Level and Lattice Conformation. *Phys Rev B* **1988**, *38*, 4180-4191.

46. Facchetti, A.; Yoon, M. H.; Marks, T. J. Gate Dielectrics for Organic Field-Effect Transistors: New Opportunities for Organic Electronics. *Adv Mater* **2005**, *17*, 1705-1725.

47. Kline, R. J.; McGehee, M. D. Morphology and Charge Transport in Conjugated Polymer. *Polym Rev* **2006**, *46*, 27-45.

48. Sirringhaus, H.; Brown, P. J.; Friend, R. H.; Nielsen, M. M.; Bechgaard, K.; Langeveld-Voss, B. M. W.; Spiering, A. J. H.; Janssen, R. A. J.; Meijer, E. W.; Herwig, P.*, et al.* Two-Dimensional Charge Transport in Self-Organized, High-Mobility Conjugated Polymers. *Nature* **1999**, *401*, 685-688.

49. Kline, R. J.; McGehee, M. D.; Kadnikova, E. N.; Liu, J. S.; Frechet, J. M. J.; Toney, M. F. Dependence of Regioregular Poly(3-Hexylthiophene) Film Morphology and Field-Effect Mobility on Molecular Weight. *Macromolecules* **2005**, *38*, 3312-3319.

50. Bao, Z.; Dodabalapur, A.; Lovinger, A. J. Soluble and Processable Regioregular Poly(3-Hexylthiophene) for Thin Film Field-Effect Transistor Applications with High Mobility. *Appl Phys Lett* **1996**, *69*, 4108-4110.

51. Ballantyne, A. M.; Chen, L.; Dane, J.; Hammant, T.; Braun, F. M.; Heeney, M.; Duffy, W.; McCulloch, I.; Bradley, D. D. C.; Nelson, J. The Effect of Poly(3-Hexylthiophene) Molecular Weight on Charge Transport and the Performance of Polymer : Fullerene Solar Cells. *Adv Funct Mater* **2008**, *18*, 2373-2380.

52. Fenton, D. E.; Parker, J. M.; Wright, P. V. Complexes of Alkali-Metal Ions with Poly(Ethylene Oxide). *Polymer* **1973**, *14*, 589-589.

53. Lascaud, S.; Perrier, M.; Vallee, A.; Besner, S.; Prudhomme, J.; Armand, M. Phase-Diagrams and Conductivity Behavior of Poly(Ethylene Oxide) Molten-Salt Rubbery Electrolytes. *Macromolecules* **1994**, *27*, 7469-7477.

54. Berthier, C.; Gorecki, W.; Minier, M.; Armand, M. B.; Chabagno, J. M.; Rigaud, P. Microscopic Investigation of Ionic-Conductivity in Alkali-Metal Salts Poly(Ethylene Oxide) Adducts. *Solid State Ionics* **1983**, *11*, 91-95.

55. Teran, A. A.; Tang, M. H.; Mullin, S. A.; Balsara, N. P. Effect of Molecular Weight on Conductivity of Polymer Electrolytes. *Solid State Ionics* **2011**, *203*, 18-21.

56. Borodin, O.; Smith, G. D. Mechanism of Ion Transport in Amorphous Poly(Ethylene Oxide)/Litfsi from Molecular Dynamics Simulations. *Macromolecules* **2006**, *39*, 1620-1629.

57. Stoeva, Z.; Martin-Litas, I.; Staunton, E.; Andreev, Y. G.; Bruce, P. G. Ionic Conductivity in the Crystalline Polymer Electrolytes Peo6 : Lixf6, X = P, as, Sb. *J Am Chem Soc* **2003**, *125*, 4619-4626.

58. Hallinan Jr., D. T.; Balsara, N. P. Polymer Electrolytes. *Annual Review of Materials Research* **2013**, *43*.

59. Matsen, M. W.; Bates, F. S. Unifying Weak- and Strong-Segregation Block Copolymer Theories. *Macromolecules* **1996**, *29*, 1091-1098.

60. Matsen, M. W. Effect of Architecture on the Phase Behavior of Ab-Type Block Copolymer Melts. *Macromolecules* **2012**, *45*, 2161-2165.

61. Leibler, L. Theory of Microphase Separation in Block Co-Polymers. *Macromolecules* **1980**, *13*, 1602-1617.

62. Matsen, M. W.; Bates, F. S. Conformationally Asymmetric Block Copolymers. *J Polym Sci Pol Phys* **1997**, *35*, 945-952.

63. Beardsley, T. M.; Matsen, M. W. Monte Carlo Phase Diagram for a Polydisperse Diblock Copolymer Melt. *Macromolecules* **2011**, *44*, 6209-6219.

64. Fredrickson, G. H.; Helfand, E. Fluctuation Effects in the Theory of Microphase Separation in Block Copolymers. *J Chem Phys* **1987**, *87*, 697-705.

65. Holyst, R.; Schick, M. Correlations in a Rigid - Flexible Diblock Copolymer System. *J Chem Phys* **1992**, *96*, 730-740.

66. Hammouda, B. Scattering from Mixtures of Flexible and Stiff Polymers. *J Chem Phys* **1993**, *98*, 3439-3444.

67. Olsen, B. D.; Segalman, R. A. Self-Assembly of Rod-Coil Block Copolymers. *Materials Science & Engineering R-Reports* **2008**, *62*, 37-66.

68. Singh, C.; Goulian, M.; Liu, A. J.; Fredrickson, G. H. Phase-Behavior of Semiflexible Diblock Copolymers. *Macromolecules* **1994**, *27*, 2974-2986.

69. Pryamitsyn, V.; Ganesan, V. Self-Assembly of Rod-Coil Block Copolymers. *J. Chem. Phys.* **2004**, *120*, 5824-5838.

70. Olsen, B. D.; Shah, M.; Ganesan, V.; Segalman, R. A. Universalization of the Phase Diagram for a Model Rod-Coil Diblock Copolymer. *Macromolecules* **2008**, *41*, 6809-6817.

71. McCulloch, B.; Ho, V.; Hoarfrost, M.; Stanley, C.; Do, C.; Heller, W. T.; Segalman, R. A. Polymer Chain Shape of Poly(3-Alkylthiophenes) in Solution Using Small-Angle Neutron Scattering. *Macromolecules* **2013**, *46*, 1899-1907.

72. Rangarajan, P.; Register, R. A.; Fetters, L. J.; Bras, W.; Naylor, S.; Ryan, A. J. Crystallization of a Weakly Segregated Polyolefin Diblock Copolymer. *Macromolecules* **1995**, *28*, 4932-4938.

73. Ryan, A. J.; Hamley, I. W.; Bras, W.; Bates, F. S. Structure Development in Semicrystalline Diblock Copolymers Crystallizing from the Ordered Melt. *Macromolecules* **1995**, *28*, 3860-3868.

74. Quiram, D. J.; Register, R. A.; Marchand, G. R. Crystallization of Asymmetric Diblock Copolymers from Microphase-Separated Melts. *Macromolecules* **1997**, *30*, 4551-4558.

75. Hamley, I. W. Crystallization in Block Copolymers. *Adv Polym Sci* **1999**, *148*, 113-137.

76. Loo, Y. L.; Register, R.; Ryan, A. Crystallization Kinetics of a Strongly Segregated Sphere-Forming Diblock Copolymer. *Abstr Pap Am Chem S* **1999**, *218*, U672-U672.

77. Loo, Y. L.; Register, R. A.; Ryan, A. J. Polymer Crystallization in 25-Nm Spheres. *Phys Rev Lett* **2000**, *84*, 4120-4123.

78. Zhu, L.; Cheng, S. Z. D.; Calhoun, B. H.; Ge, Q.; Quirk, R. P.; Thomas, E. L.; Hsiao, B. S.; Yeh, F.; Lotz, B. Phase Structures and Morphologies Determined by Self-Organization, Vitrification, and Crystallization: Confined Crystallization in an Ordered Lamellar Phase of Peo-B-Ps Diblock Copolymer. *Polymer* **2001**, *42*, 5829-5839.

79. Loo, Y. L.; Register, R. A.; Ryan, A. J. Modes of Crystallization in Block Copolymer Microdomains: Breakout, Templated, and Confined. *Macromolecules* **2002**, *35*, 2365-2374.

80. Xu, J. T.; Fairclough, J. P. A.; Mai, S. M.; Chaibundit, C.; Mingvanish, M.; Booth, C.; Ryan, A. J. Crystallization Behavior of Oxyethylene/Oxybutylene Diblock and Triblock Copolymers. *Polymer* **2003**, *44*, 6843-6850.

81. Delacourt, C.; Laffont, L.; Bouchet, R.; Wurm, C.; Leriche, J. B.; Morcrette, M.; Tarascon, J. M.; Masquelier, C. Toward Understanding of Electrical Limitations (Electronic, Ionic) in Limpo4 (M = Fe, Mn) Electrode Materials. *J Electrochem Soc* **2005**, *152*, A913-A921.

82. Bazito, F. F. C.; Torresi, R. M. Cathodes for Lithium Ion Batteries: The Benefits of Using Nanostructured Materials. *J. Braz. Chem. Soc.* **2006**, *17*, 627-642.

83. Wang, C. S.; Hong, J. Ionic/Electronic Conducting Characteristics of Lifepo4 Cathode Materials - the Determining Factors for High Rate Performance. *Electrochemical and Solid State Letters* **2007**, *10*, A65-A69.

84. Atebamba, J. M.; Moskon, J.; Pejovnik, S.; Gaberscek, M. On the Interpretation of Measured Impedance Spectra of Insertion Cathodes for Lithium-Ion Batteries. *J Electrochem Soc* **2010**, *157*, A1218-A1228.

85. Singh, M.; Odusanya, O.; Wilmes, G. M.; Eitouni, H. B.; Gomez, E. D.; Patel, A. J.; Chen, V. L.; Park, M. J.; Fragouli, P.; Iatrou, H.*, et al.* Effect of Molecular Weight on the Mechanical and Electrical Properties of Block Copolymer Electrolytes. *Macromolecules* **2007**, *40*, 4578-4585.

86. Panday, A.; Mullin, S.; Gomez, E. D.; Wanakule, N.; Chen, V. L.; Hexemer, A.; Pople, J.; Balsara, N. P. Effect of Molecular Weight and Salt Concentration on Conductivity of Block Copolymer Electrolytes. *Macromolecules* **2009**, *42*, 4632-4637.

87. Stone, G. M.; Mullin, S. A.; Teran, A. A.; Hallinan, D. T.; Minor, A. M.; Hexemer, A.; Balsara, N. P. Resolution of the Modulus Versus Adhesion Dilemma in Solid Polymer Electrolytes for Rechargeable Lithium Metal Batteries. *J Electrochem Soc* **2012**, *159*, A222-A227.

88. Hallinan, D. T.; Mullin, S. A.; Stone, G. M.; Balsara, N. P. Lithium Metal Stability in Batteries with Block Copolymer Electrolytes. *J Electrochem Soc* **2013**, *160*, A464-A470.

89. Jeffries-El, M.; Sauve, G.; Iovu, M.; McCullough, R. D. *In Situ* End Group Modification of Regioregular Poly(3-Alkylthiophenes) Via Grignard Metathesis (Grim) Polymerization. *Abstracts of Papers of the American Chemical Society* **2004**, *227*, U418-U418.

90. Parrish, B.; Breitenkamp, R.; Emrick, T. Peg- and Peptide-Grafted Aliphatic Polyesters by Click Chemistry. *J. Am. Chem. Soc.* **2005**, *127*, 7404-7410.

91. Iovu, M. C.; Sheina, E. E.; Gil, R. R.; McCullough, R. D. Experimental Evidence for the Quasi-"Living" Nature of the Grignard Metathesis Method for the Synthesis of Regioregular Poly(3-Alkylthiophenes). *Macromolecules* **2005**, *38*, 8649-8656.

92. McCullough, R. D. Power of Maldi for Preparing Electrically Conductive Nanowires. *Abstracts of Papers of the American Chemical Society* **2003**, *225*, U672-U672.

93. Rader, H. J.; Schrepp, W. Maldi-Tof Mass Spectrometry in the Analysis of Synthetic Polymers. *Acta Polym* **1998**, *49*, 272-293.

94. Nielen, M. W. F. Maldi Time-of-Flight Mass Spectrometry of Synthetic Polymers. *Mass Spectrom Rev* **1999**, *18*, 309-344.

95. Liu, J. S.; Loewe, R. S.; McCullough, R. D. Employing Maldi-Ms on Poly(Alkylthiophenes): Analysis of Molecular Weights, Molecular Weight Distributions, End-Group Structures, and End-Group Modifications. *Macromolecules* **1999**, *32*, 5777-5785.

96. Pasch, H.; Schrepp, W. *Maldi-Tof Mass Spectrometry of Synthetic Polymers*. Springer: Berlin ; New York, 2003; p xviii, 298 p.

97. Montaudo, G.; Samperi, F.; Montaudo, M. S. Characterization of Synthetic Polymers by Maldi-Ms. *Prog Polym Sci* **2006**, *31*, 277-357.

98. Malik, S.; Nandi, A. K. Crystallization Mechanism of Regioregular Poly(3-Alkyl Thiophene)S. *J. Polym. Sci. Pt. B-Polym. Phys.* **2002**, *40*, 2073-2085.

99. Patil, A. O.; Heeger, A. J.; Wudl, F. Optical-Properties of Conducting Polymers. *Chem Rev* **1988**, *88*, 183-200.

100. Craley, C. R.; Zhang, R.; Kowalewski, T.; McCullough, R. D.; Stefan, M. C. Regioregular Poly(3-Hexylthiophene) in a Novel Conducting Amphiphilic Block Copolymer. *Macromol Rapid Comm* **2009**, *30*, 11-16.

101. Ho, V.; Boudouris, B. W.; Segalman, R. A. Tuning Polythiophene Crystallization through Systematic Side Chain Functionalization. *Macromolecules* **2010**, *43*, 7895-7899.

102. Segalman, R. A.; McCulloch, B.; Kirmayer, S.; Urban, J. J. Block Copolymers for Organic Optoelectronics. *Macromolecules* **2009**, *42*, 9205-9216.

103. Steele, B. C. H.; Heinzel, A. Materials for Fuel-Cell Technologies. *Nature* **2001**, *414*, 345-352.

104. Tarascon, J. M.; Armand, M. Issues and Challenges Facing Rechargeable Lithium Batteries. *Nature* **2001**, *414*, 359-367.

105. Darling, S. B. Block Copolymers for Photovoltaics. *Energy & Environmental Science* **2009**, *2*, 1266-1273.

106. Sauve, G.; McCullough, R. D. High Field-Effect Mobilities for Diblock Copolymers of Poly(3-Hexylthiophene) and Poly(Methyl Acrylate). *Adv. Mater.* **2007**, *19*, 1822-+.

107. Iovu, M. C.; Zhang, R.; Cooper, J. R.; Smilgies, D. M.; Javier, A. E.; Sheina, E. E.; Kowalewski, T.; McCullough, R. D. Conducting Block Copolymers of Regioregular Poly(3-Hexylthiophene) and Poly(Methacrylates): Electronic Materials with Variable Conductivities and Degrees of Interfibrillar Order. *Macromol. Rapid Comm.* **2007**, *28*, 1816-1824.

108. Cooper, J. R.; Zhang, R.; Iovu, M. C.; McCullough, R. D.; Kowalewski, T. Comparative Study of Poly(3-Alkylthiophene) Triblock Copolymers. *Abstracts of Papers of the American Chemical Society* **2005**, *230*, U4199-U4199.

109. Ho, V.; Boudouris, B. W.; McCulloch, B. L.; Shuttle, C. G.; Burkhardt, M.; Chabinyc, M. L.; Segalman, R. A. Poly(3-Alkylthiophene) Diblock Copolymers with Ordered Microstructures and Continuous Semiconducting Pathways. *J Am Chem Soc* **2011**, *133*, 9270-9273.

110. Moon, H. C.; Bae, D.; Kim, J. K. Self-Assembly of Poly(3-Dodecylthiophene)-Block-Poly(Methyl Methacrylate) Copolymers Driven by Competition between Microphase Separation and Crystallization. *Macromolecules* **2012**.

111. Loo, Y. L.; Register, R. A.; Ryan, A. J.; Dee, G. T. Polymer Crystallization Confined in One, Two, or Three Dimensions. *Macromolecules* **2001**, *34*, 8968-8977.

112. Mai, S. M.; Fairclough, J. P. A.; Viras, K.; Gorry, P. A.; Hamley, I. W.; Ryan, A. J.; Booth, C. Chain Folding in Semicrystalline Oxyethylene/Oxybutylene Diblock Copolymers. *Macromolecules* **1997**, *30*, 8392-8400.

113. Hamley, I. W.; Fairclough, J. P. A.; Bates, F. S.; Ryan, A. J. Crystallization Thermodynamics and Kinetics in Semicrystalline Diblock Copolymers. *Polymer* **1998**, *39*, 1429-1437.

114. Dimarzio, E. A.; Guttman, C. M.; Hoffman, J. D. Calculation of Lamellar Thickness in a Diblock Co-Polymer, One of Whose Components Is Crystalline. *Macromolecules* **1980**, *13*, 1194-1198.

115. Whitmore, M. D.; Noolandi, J. Theory of Crystallizable Block Copolymer Blends. *Macromolecules* **1988**, *21*, 1482-1496.

116. Chang, J.-F.; Sun, B.; Breiby, D. W.; Nielsen, M. M.; Sölling, T. I.; Giles, M.; McCulloch, I.; Sirringhaus, H. Enhanced Mobility of Poly(3-Hexylthiophene) Transistors by Spin-Coating from High-Boiling-Point Solvents. *Chemistry of Materials* **2004**, *16*, 4772-4776.

117. Sirringhaus, H. B. P. J. Two-Dimensional Charge Transport in Self-Organized, High-Mobility Conjugated Polymers. *Nature* **1999**, *401*, 685.

118. Kim, H.; Seo, M.; Park, M. H.; Cho, J. A Critical Size of Silicon Nano-Anodes for Lithium Rechargeable Batteries. *Angew Chem Int Edit* **2010**, *49*, 2146-2149.

119. Boudouris, B. W.; Ho, V.; Jimison, L. H.; Toney, M. F.; Salleo, A.; Segalman, R. A. Real-Time Observation of Poly(3-Alkylthiophene) Crystallization and Correlation with Transient Optoelectronic Properties. *Macromolecules* **2011**, *44*, 6653-6658.

120. Lin, C. C.; Jonnalagadda, S. V.; Kesani, P. K.; Dai, H. J.; Balsara, N. P. Effect of Molecular-Structure on the Thermodynamics of Block-Copolymer Melts. *Macromolecules* **1994**, *27*, 7769-7780.

121. Eitouni, H. B.; Balsara, N. P. Thermodynamics of Polymer Blends. In *Physical Properties of Polymers Handbook*; Mark, J. E., Ed.; Springer: New York, 2007; pp 339-356.

122. Wanakule, N. S.; Panday, A.; Mullin, S. A.; Gann, E.; Hexemer, A.; Balsara, N. P. Ionic Conductivity of Block Copolymer Electrolytes in the Vicinity of Order-Disorder and Order-Order Transitions. *Macromolecules* **2009**, *42*, 5642-5651.

123. Patel, S. N.; Javier, A. E.; Stone, G. M.; Mullin, S. A.; Balsara, N. P. Simultaneous Conduction of Electronic Charge and Lithium Ions in Block Copolymers. *Acs Nano* **2012**, *6*, 1589-1600.

124. Nojima, S.; Ono, M.; Ashida, T. Crystallization of Block Copolymers .2. Morphological-Study of Poly(Ethylene Glycol) Poly Epsilon-Caprolactone) Block Copolymers. *Polym J* **1992**, *24*, 1271-1280.

125. Wanakule, N. S.; Virgili, J. M.; Teran, A. A.; Wang, Z. G.; Balsara, N. P. Thermodynamic Properties of Block Copolymer Electrolytes Containing Imidazolium and Lithium Salts. *Macromolecules* **2010**, *43*, 8282-8289.

126. Xu, J. T.; Fairclough, J. P. A.; Mai, S. M.; Ryan, A. J.; Chaibundit, C. Isothermal Crystallization Kinetics and Melting Behavior of Poly(Oxyethylene)-B-Poly(Oxybutylene)/Poly(Oxybutylene) Blends. *Macromolecules* **2002**, *35*, 6937-6945.

127. Xu, J. T.; Turner, S. C.; Fairclough, J. P. A.; Mai, S. M.; Ryan, A. J.; Chaibundit, C.; Booth, C. Morphological Confinement on Crystallization in Blends of Poly(Oxyethylene-Block-Oxybutylene) and Poly(Oxybutylene). *Macromolecules* **2002**, *35*, 3614-3621.

128. Personal Correspondance with Victor Ho, Bryan Mcculloch and Rachel Segalman.

129. Nakamura, I.; Balsara, N. P.; Wang, Z. G. Thermodynamics of Ion-Containing Polymer Blends and Block Copolymers. *Phys Rev Lett* **2011**, *107*.

130. Nakamura, I.; Wang, Z. G. Salt-Doped Block Copolymers: Ion Distribution, Domain Spacing and Effective Chi Parameter. *Soft Matter* **2012**, *8*, 9356-9367.

131. Riess, I. Mixed Ionic-Electronic Conductors - Material Properties and Applications. *Solid State Ionics* **2003**, *157*, 1-17.

132. Teraoka, Y.; Zhang, H. M.; Okamoto, K.; Yamazoe, N. Mixed Ionic-Electronic Conductivity of La1-Xsrxco1-Yfeyo3-Delta Perovskite-Type Oxides. *Mater. Res. Bull.* **1988**, *23*, 51-58.

133. Adler, S. B. Limitations of Charge-Transfer Models for Mixed-Conducting Oxygen Electrodes. *Solid State Ionics* **2000**, *135*, 603-612.

134. Adler, S. B.; Lane, J. A.; Steele, B. C. H. Electrode Kinetics of Porous Mixed-Conducting Oxygen Electrodes. *J. Electrochem. Soc.* **1996**, *143*, 3554-3564.

135. Riess, I. Measurements of Electronic and Ionic Partial Conductivities in Mixed Conductors, without the Use of Blocking Electrodes. *Solid State Ionics* **1991**, *44*, 207-214.

136. Riess, I. Review of the Limitation of the Hebb-Wagner Polarization Method for Measuring Partial Conductivities in Mixed Ionic Electronic Conductors. *Solid State Ionics* **1996**, *91*, 221-232.

137. Huggins, R. A. Simple Method to Determine Electronic and Ionic Components of the Conductivity in Mixed Conductors - a Review. *Ionics* **2002**, *8*, 300-13.

138. Jamnik, J.; Maier, J. Treatment of the Impedance of Mixed Conductors - Equivalent Circuit Model and Explicit Approximate Solutions. *J. Electrochem. Soc.* **1999**, *146*, 4183-4188.

139. Costantini, N.; Wegner, G.; Mierzwa, M.; Pakula, T. Simultaneous Ionic and Electronic Conductivity in Polymeric Materials. *Macromol. Chem. Phys.* **2005**, *206*, 1345-1354.

140. Witker, D.; Curtis, M. D. Lithium Ion and Electronic Conductivity in 3-(Oligoethylene Oxide)Thiophene Comb-Like Polymers. *J. Power Sources* **2006**, *156*, 525-532.

141. Ren, X. M.; Pickup, P. G. Ionic and Electronic Conductivity of Poly(3-Methylpyrrole-4-Carboxylic Acid). *J. Electrochem. Soc.* **1992**, *139*, 2097-2105.

142. Ren, X. M.; Pickup, P. G. Coupling of Ion and Electron-Transport During Impedance Measurements on a Conducting Polymer with Similar Ionic and Electronic Conductivities. *J. Chem. Soc., Faraday Trans.* **1993**, *89*, 321-326.

143. Plocharski, J.; Wycislik, H. Mixed Conductivity in Poly(P-Phenylene) Doped with Iron Chloride. *Solid State Ionics* **2000**, *127*, 337-344.

144. Siroma, Z.; Hagiwara, J.; Yasuda, K.; Inaba, M.; Tasaka, A. Simultaneous Measurement of the Effective Ionic Conductivity and Effective Electronic Conductivity in a Porous Electrode Film Impregnated with Electrolyte. *J. Electroanal. Chem.* **2010**, *648*, 92-97.

145. Mullin, S. A.; Stone, G. M.; Panday, A.; Balsara, N. P. Salt Diffusion Coefficients in Block Copolymer Electrolytes. *J. Electrochem. Soc.* **2011**, *158*, A619-A627.

146. Guo, X.; Fleig, J.; Maier, J. Separation of Electronic and Ionic Contributions to the Gain Boundary Conductivity in Acceptor-Doped Srtio3. *J. Electrochem. Soc.* **2001**, *148*, J50-J53.

147. Bruce, P. G.; Gray, F. M.; Shi, J.; Vincent, C. A. Ionic Transport in Polymer Electrolytes. *Philos. Mag. A* **1991**, *64*, 1091-1099.

148. Likun, P.; Zhuo, S. Solvent and Temperature-Dependent Conductive Behavior of Poly(3-Hexylthiophene). *J. Phys. Chem. Solids* **2009**, *70*.

149. Conductivity for Peo Homopolyer/Litfsi Mixtures Were Taken from Published Data by Lascaud Et Al. (Ref. 53). The Peo Molecualar Weight Was Approximately 4 Kg/Mol. The Ionic Conductivity at 90 Oc Was Interpolated for Each Litfsi Salt Concentration in the Peo Microphase.

150. Goh, C.; Kline, R. J.; McGehee, M. D.; Kadnikova, E. N.; Frechet, J. M. J. Molecular-Weight-Dependent Mobilities in Regioregular Poly(3-Hexyl-Thiophene) Diodes. *Appl. Phys. Lett.* **2005**, *86*.

151. Lu, G.; Tang, H.; Qu, Y.; Li, L.; Yang, X. Enhanced Electrical Conductivity of Highly Crystalline Polythiophene/Insulating-Polymer Composite. *Macromolecules* **2007**, *40*, 6579-6584.

152. Lu, G.; Tang, H.; Huan, Y.; Li, S.; Li, L.; Wang, Y.; Yang, X. Enhanced Charge Transportation in Semiconducting Polymer/Insulating Polymer Composites: The Role of an Interpenetrating Bulk Interface. *Adv. Funct. Mater.* **2010**, *20*, 1714-1720.

153. Goffri, S.; Muller, C.; Stingelin-Stutzmann, N.; Breiby, D.; Radano, C.; Andreasen, J.; Thompson, R.; Janssen, R.; Nielsen, M.; Smith, P.*, et al.* Multicomponent Semiconducting Polymer Systems with Low Crystallization-Induced Percolation Threshold. *Nat. Mater.* **2006**, *5*, 950-956.

154. Dante, M.; Yang, C.; Walker, B.; Wudl, F.; Nguyen, T.-Q. Self-Assembly and Charge-Transport Properties of a Polythiophene-Fullerene Triblock Copolymer. *Adv. Mater.* **2010**, *22*, 1835-1839.

155. Kumar, A.; Baklar, M.; Scott, K.; Kreouzis, T.; Stingelin-Stutzmann, N. Efficient, Stable Bulk Charge Transport in Crystalline/Crystalline Semiconductor-Insulator Blends. *Adv. Mater.* **2009**, *21*, 4447-4451.

156. Arico, A. S.; Bruce, P.; Scrosati, B.; Tarascon, J. M.; Van Schalkwijk, W. Nanostructured Materials for Advanced Energy Conversion and Storage Devices. *Nat Mater* **2005**, *4*, 366-377.

157. Cho, J. H.; Lee, J.; Xia, Y.; Kim, B.; He, Y. Y.; Renn, M. J.; Lodge, T. P.; Frisbie, C. D. Printable Ion-Gel Gate Dielectrics for Low-Voltage Polymer Thin-Film Transistors on Plastic. *Nat Mater* **2008**, *7*, 900-906.

158. Panzer, M. J.; Frisbie, C. D. Exploiting Ionic Coupling in Electronic Devices: Electrolyte-Gated Organic Field-Effect Transistors. *Adv Mater* **2008**, *20*, 3177-3180.

159. Larsson, O.; Laiho, A.; Schmickler, W.; Berggren, M.; Crispin, X. Controlling the Dimensionality of Charge Transport in an Organic Electrochemical Transistor by Capacitive Coupling. *Adv Mater* **2011**, *23*, 4764-+.

160. Bubnova, O.; Berggren, M.; Crispin, X. Tuning the Thermoelectric Properties of Conducting Polymers in an Electrochemical Transistor. *J Am Chem Soc* **2012**, *134*, 16456-16459.

161. Macinnes, D.; Druy, M. A.; Nigrey, P. J.; Nairns, D. P.; Macdiarmid, A. G.; Heeger, A. J. (Ch)X Organic Batteries - Reversible N-Type and P-Type Electrochemical Dopiing of Polyacetylene. *Journal of the Chemical Society-Chemical Communications* **1981**, 317-319.

162. Kaufman, J. H.; Chung, T. C.; Heeger, A. J.; Wudl, F. Poly(Thiophene) - a Stable Polymer Cathode Material. *J. Electrochem. Soc.* **1984**, *131*, 2092-2093.

163. Chen, G. Y.; Richardson, T. J. Overcharge Protection for High Voltage Lithium Cells Using Two Electroactive Polymers. *Electrochemical and Solid State Letters* **2006**, *9*, A24-A26.

164. Guoying, C.; Richardson, T. J. Overcharge Protection for Rechargeable Lithium Batteries Using Electroactive Polymers. *Electrochem. Solid-State Lett.* **2004**, *7*, A23-A26.

165. Hadjichristidis, N.; Iatrou, H.; Pispas, S.; Pitsikalis, M. Anionic Polymerization: High Vacuum Techniques. *J Polym Sci Pol Chem* **2000**, *38*, 3211-3234.

166. Quirk, R. P.; Kim, J.; Kausch, C.; Chun, M. S. Butyllithium-Initiated Anionic Synthesis of Well-Defined Poly(Styrene-Block-Ethylene Oxide) Block Copolymers with Potassium Salt Additives. *Polym Int* **1996**, *39*, 3-10.

167. Javier, A. E.; Patel, S. N.; Hallinan, D. T.; Srinivasan, V.; Balsara, N. P. Simultaneous Electronic and Ionic Conduction in a Block Copolymer: Application in Lithium Battery Electrodes. *Angew. Chem. Int. Ed.* **2011**, *50*, 9848-9851.

168. Yuan, R.; Teran, A. A.; Gurevitch, I.; Mullin, S. A.; Wanakule, N. S.; Balsara, N. P. Ionic Conductivity of Low Molecular Weight Block Copolymer Electrolytes. *Macromolecules* **2013**, *46*, 914-921.

169. Bredas, J. L.; Themans, B.; Fripiat, J. G.; Andre, J. M.; Chance, R. R. Highly Conducting Polyparaphenylene, Polypyrrole, and Polythiophene Chains - an Abinitio Study of the Geometry and Electronic-Structure Modifications Upon Doping. *Phys Rev B* **1984**, *29*, 6761-6773.

170. Ciprelli, J. L.; Clarisse, C.; Delabouglise, D. Enhanced Stability of Conducting Poly(3-Octylthiophene) Thin Films Using Organic Nitrosyl Compounds. *Synthetic Met* **1995**, *74*, 217-222.

171. Shimotani, H.; Diguet, G.; Iwasa, Y. Direct Comparison of Field-Effect and Electrochemical Doping in Regioregular Poly(3-Hexylthiophene). *Appl Phys Lett* **2005**, *86*.

172. Arkhipov, V. I.; Emelianova, E. V.; Heremans, P.; Bassler, H. Analytic Model of Carrier Mobility in Doped Disordered Organic Semiconductors. *Phys Rev B* **2005**, *72*.

173. Richardson, T. J.; Ross, P. N. Overcharge Protection for Rechargeable Lithium Polymer Electrolyte Batteries. *J. Electrochem. Soc.* **1996**, *143*, 3992-3996.

Chapter 8 - Appendix

8.1 List of Symbols

A	area (cm^2)
d	domain spacing
E_{ox}	oxidation voltage *versus* Li/Li^+ (V)
E_{we}	electrochemical cell voltage *versus* Li/Li^+ (V)
I_{abs}	absolute scattering intensity (cm^{-1})
i	current density (mA/cm^2)
L	thickness (cm)
l_{EHT}	P3EHT statistical segment length (nm)
l_{PEO}	PEO statistical segment length (nm)
M_n	number-average molecular weight of a polymer
M_w	weight-average molecular weight of a polymer
N	degree of polymerization
q	scattering vector
Q_{bulk}	constant phase element for geometric capacitance
Q_{int}	constant phase element for interfacial capacitance
Q_{grb}	constant phase element for ionic grain boundary capacitance
r_0	total LiTFSI salt concentration
r_{EO}	LiTFSI salt concentration in PEO phase
r_{HT}	LiTFSI salt concentration in P3HT phase
R_0	lead resistance for impedance data
R_1	higher frequency semicircle real impedance intercept
R_2	middle frequency semicircle real impedance intercept
R_3	low frequency semicircle real impedance intercept
R_{dc}	dc resistance
R_{grb}	grain boundary resistance
R_i	ionic resistance
R_e	electronic resistance
r_{ox}	oxidation level
t	time
Z'	real impedance
Z''	imaginary impedance

GREEK

χ	Flory-Huggins interaction parameter
χ_{eff}	effective Flory-Huggins interaction parameter
ϕ_{HT}	P3HT volume fraction
ϕ_{EO}	PEO volume fraction
μ_{ox}	hole charge carrier mobility ($cm^2V^{-1}s^{-1}$)
ρ_{P3HT}	P3HT density (g/cm^3)
ρ_{P3EHT}	P3EHT density (g/cm^3)
ρ_{PEO}	PEO density (g/cm^3)

σ_e	neutral electronic conductivity (S/cm)
$\sigma_{e,N}$	normalized neutral electronic conductivity (S/cm)
$\sigma_{e,ox}$	oxidized electronic conductivity (S/cm)
σ_i	ionic conductivity (S/cm)
$\sigma_{i,N}$	normalized ionic conductivity (S/cm)

8.2 Absolute Molecular Weight Measurement via GPC

8.2.1 *Theory*

The light scattering detector in a GPC allows for the direct measurement of the absolute molecular weight of a polymer. Low angle light scattering (LALS) measurement provides the weight-average molecular weight of the polymer (M_w). The concentration of the polymer solution running through the GPC is measured by the refractive index (RI) detector. This detector is crucial in accurately measuring the refractive index increment of the polymer solution. By combining the results from the LALS and RI measurements, one can easily obtain M_w of any given polymer.

The fundamental light scattering equation for polymer solutions is given by the Zimm equation,

$$\frac{KC}{R_\theta} = \frac{1}{M_w P_\theta} + 2A_2 C, \tag{7.1}$$

where C is the sample concentration, A_2 is the second virial coefficient of the solution, R_θ is the excess Rayleigh scattering ratio of the solution above that of the pure solvent, measured at an angle θ with respect to the incident beam.

$$R_\theta = k\frac{I_\theta}{I_0} = k\frac{LALS_{area}}{I_0}, \tag{7.2}$$

where k is an instrument constant related to the scattered light collection efficient, I_θ is the excess intensity of the scattered light above that of the pure solvent, which is related to the low angle light scattering signal peak area ($LALS_{area}$). P_θ is the particle scattering factor, but can be ignored at the limit of low angles (equals unity when θ = zero and is 0.98 when θ = 7 °C). K in Equation 7.1 is a composite of optical and fundamental constants.

$$K = \frac{2p\left(\pi n_0 \frac{dn}{dc}\right)^2}{N_A \lambda_0^4}, \tag{7.3}$$

where n_0 is the refractive index of the solvent, dn/dc is the refractive index increment of the polymer solution, N_A is Avogrado's number, λ_0 is wavelength of the incident light, and p is an interger value of 1 for un-polarized light and 2 for vertically polarized light. N_A, λ_0, and p are instrument constant, which can be combined with detector constant k and I_0 given in the Equation 7.2. This forms a new constant k_{LALS}. Rearranging Equation 7.1 yields

$$\frac{1}{M_w C} = \frac{n_0^2 \left(\frac{dn}{dc}\right)^2}{(k_{LALS})(LALS_{area})} - 2A_2 . \tag{7.4}$$

A_2 can be generally ignored as it is typically much smaller than the other terms in the equation, which yields

$$\boxed{\frac{1}{M_w C} = \frac{n_0^2 \left(\frac{dn}{dc}\right)^2}{(k_{LALS})(LALS_{area})}}. \tag{7.5}$$

The next step is to find a relationship for dn/dc, which can be obtained from the RI detector. Knowing the RI detector peak area (RI_{area}), one obtains the following equation:

$$RI_{area} = \frac{k_{RI}}{n_0} C_{area} \left(\frac{dn}{dc}\right), \tag{7.6}$$

where k_{RI} is the RI detector calibration constant and C_{area} is the concentration area, which is the total mass of polymer injected,

$$C_{area} = CV_{inj} , \tag{7.7}$$

where V_{inj} is the injected volume. Combining equation 7.6 and 7.7 and solving for dn/dc yields the following equation:

$$\boxed{\frac{dn}{dc} = \frac{n_0 RI_{area}}{k_{RI} V_{inj} C}}. \tag{7.8}$$

Substituting equation 7.8 into equation 7.5 yields

$$\frac{C}{M_w} = \frac{\frac{n_0^3}{(k_{RI})^2 (V_{inj})^2} (RI_{area})^2}{(k_{LALS})(LALS_{area})} . \tag{7.9}$$

To further simplify the equation, n_0 and V_{inj} are combined with the detector calibration constants (k_{RI} and k_{LALS}) to obtain an overall calibration constant k_{cal}. Solving equation 7.9 for M_w yields

$$\boxed{M_w = k_{cal} \frac{LALS_{area}}{(RI_{area})^2} C}. \tag{7.10}$$

Equation 7.10 allows for the determination of M_w from the LALS and RI peaks areas of the GPC chromatograms.

8.2.2 *Example of M_w Calculations*

A polystyrene (PS) standard with C = 1.078 mg/mL (M_w = 80.7 kg/mol, PDI = 1.01) was run through the GPC (THF as the eluent). The area of the RI and LALS peaks were 21.199 and 20.022, respectively. All parameters are known for equation 7.10, thus allowing for the calculation of k_{cal}, which is equal to 1.6803 x 10^6. Now that we have a calibration constant, we can determine the molecular weight of any other polymer of choice. To confirm that the calibration works, I determined the M_w of a poly(isobutylene) (PIB) previously synthesized and characterized in the lab. The M_w of the PIB used should be 56,800 g/mol. A PIB solution with C = 1.19 mg/mL was run through the GPC. The area of the RI and LALS peaks were 14.289 and 5.7941, respectively. Using equation 7.10, the M_w is calculated to be 56,700 g/mol, which is in very good agreement with the expected M_w.

Alternatively, we can determine M_w by applying equation 7.5 and 7.8. We first calculate k_{LALS} and k_{RI} using the PS standard (knowing that the *dn/dc* of PS in THF is 0.185). Next, using equation 7.8, we can calculate the *dn/dc* of PIB in THF. Finally, we can calculate the M_w of PIB using equation 7.5 using the calculated value of *dn/dc*. With this method, you can determine the *dn/dc* of the polymer that you are trying to characterize. This is a good check to see if your molecular weight measurements are accurate.

8.2.3 *Preparing GPC Sample Solutions*

Amber Bottles

- Buy at least three amber bottles from the stockroom.
- Remove any sticker or label that may be on the bottle.
- Place the bottles in the base bath overnight or about a day.
- After removing from base bath, wash thoroughly with methanol and THF.
- Allow the bottle to dry at least overnight to make sure it is completely dry.

PS Solution Preparation

- Remove the bottle from the oven and let it cool to room temperature and tighten the cap onto the bottle.
- Wipe the outsides of the whole bottle with a kimwipe to remove any debris.
- Label the top of the cap with a marker (i.e. PS3-20).
- Place the capped bottle onto the balance, let the mass stabilize, and record the mass.
- Remove the bottle from the balance, but don't tare the balance.
- Add 50 mg of PS into the bottle. Make sure you are adding the polymer outside the balance.

- Weigh the bottle again to see how much polymer was added to the bottle.
- You may need to add or remove polymer multiple times to reach the correct mass of polymer.
- After getting about 50 mg of PS, measure out 50 mL of HPLC grade (Burdick and Jackson) Toluene into a graduated cylinder.
- It may be easier to add the last few drops with a pipette so you don't overshoot the volume measurements.
- Add the Toluene into the bottle and let it dissolve for about an hour before using the solution.
- Weigh the bottle, which will be needed to calculate the actual concentration of the polymer. The density of toluene is 0.948 g/mL.
- Record the concentration